5-17-2022 10:00 AM

A Molecular Dynamics Study Of Polymer Chains In Shear Flows and Nanocomposites

Venkat Bala, *The University of Western Ontario*

Supervisor: Denniston, Colin, *The University of Western Ontario*

A thesis submitted in partial fulfillment of the requirements for the Doctor of Philosophy degree in Applied Mathematics

Abstract

In this work we study single chain polymers in shear flows and nanocomposite polymer melts extensively through the use of large scale molecular dynamics simulations through LAMMPS [130]. In the single polymer chain shear flow study, we use the Lattice-Boltzmann method to simulate fluid dynamics and also include thermal noise as per the *fluctuation-dissipation* theorem in the system. When simulating the nanocomposite polymer melts, we simply use a Langevin thermostat to mimic a heat bath.

In the single polymer in shear flow study we investigated the margination of a single chain towards solid surfaces and how strongly the shear flow influences this effect. In particular we also tried to study the effect of the polymer's monomer size a on its overall tendency to marginate. To this end, we studied polymer chains of length $N = 16, 32$ in flows at multiple shear rates, $\dot{\gamma}$ and noted higher margination rates in the case of chains with larger radii monomers in comparison to smaller radii monomer chains. We quantified this behaviour and effect by considering various measures such as the distribution of the chain's maximum extent into the flow, the distribution of its centre of mass normal to the surface as well as its radius of gyration in directions parallel and normal to the surface i.e. R_x, R_y, R_z.

In the second work, we looked at the effects of introducing nanorods into polymeric melts. We primarily focused on understanding the dispersion, orientation and conformational patterns exhibited by the nanorods and chains respectively. At lower concentrations, rods phase separated into distinct nematic clusters, while at higher concentrations they remained more isotropic and disordered. We noted that this behaviour is being driven by the system finding a trade-off between the entropic forces trying to create the isolated clusters and the enthalpic effects that work to improve mixing of the rods. We also noted that the rigid rods induced significant local conformational changes in the flexible chains in close proximity which in turn made the whole melt more ordered.

Keywords: Molecular dynamics, LAMMPS, Polymer, Polymer melts, nanrods

Lay Abstract

Polymers are everywhere and their applications in our daily lives are numerous. Be it in the healthcare field or the food industry or within the human body itself, polymers play a very key role in our day to day lives as well as in our healthy living. Understanding how these large molecules behave under different situations, forces and environments is key in order for us to be able to develop novel tools and medications.

Polymers are everywhere within the human body. DNA, the most commonly known is basically a very long polymer that encodes vital information about the human genome. Another less known polymer in the human body is the vWF (von Williebrand Fibers) that plays an extremely crucial role in preventing blood loss. It is well known that these polymers are abnormally large in comparison to other proteins in humans, and from our work we confirmed that this large size plays a major role in it performing its task of preventing blood loss. At a very high level, in case of a cut or injury to a blood vessel, the polymer detects the injury rushes to the damaged site and much like duct tape, stretches out to essentially seal the injury. In this study we investigate this very property of large polymers through the use of computer simulations.

Rigid plastics start their life as polymer melts, which is basically a fluid phase of the same and are made up of thousands of individual polymers. Several studies have been done in order to boost the mechanical properties of these melts by infusing them with rigid rods such as fiber glass. These are especially useful in the manufacturing and automotive industry due to their promising physical properties such as light weight and able to sustain high stresses. The mixture of the melt with rigid rods has resulted in materials with enhanced mechanical properties that prove to be quite useful in several applications. In our work, we investigate the same via computer simulations and study how the rigid rods affect the properties of the polymer surrounding them and also comment on potential applications of such material in industry and research.

Co-Authorship Statement

Chapter 3 in this work is based on the work published in Soft Matter on Polymer margination in shear flows by myself and my co-author/PhD supervisor Dr. Colin Denniston. In this work, I carried out the majority of the work that involved creating and running the simulations on Compute Canada's infrastructure, developing programs and scripts to analyze the simulation data as well as generating the figures and the latex document for publication. My supervisor assisted me along the way by helping me analyze the simulations results, publication drafts and in providing general feedback.

Chapter 4 in this work is based on a joint work between myself, my supervisor and another PhD graduate student Navid Afrasiabian. This work, titled Dispersion and Orientation patterns in nanorod-infused polymer melts is awaiting submission for publication in a suitable scientific journal. I initiated this project and was primary in creating and running the necessary simulations as well as in developing all the programs and scripts necessary to process the simulation results and data. I also authored the initial draft of the paper and my colleague worked on the revisions. We both shared the work load equally in generating the publication figures and our supervisor provided us with all the necessary guidance and feedback in order to finish the project.

Acknowlegements

I dedicate this work to my wife (Lawanya Mayil), daughter (Isha) and my parents (Bala Muthuswamy & Vijayalakshami) and thank them for their persistent support and faith in me throughout my doctoral years. I also sincerely thank my supervisor for providing me with the much needed guidance and advice over the course of my doctoral studies

Contents

List of Figures

List of Tables

Chapter 1

Introduction

1.1 Literature Review

Polymers are everywhere and have found wide spread applications and use in all aspects of our lives. The word *polymer* simply means many parts and refers to molecules consisting of many elementary units conventionally termed as *monomers*. Monomers are the atomic and fundamental unit of a polymer and are connected together by covalent bonds. The process of generating the entire structure of a polymer is known as *polymerization* and it refers to the process by which the basic units i.e. monomers are covalently linked together. The number of monomers in a polymer is termed as its *degree of polymerization*, N and its *molar mass* M is equal to its degree of polymerization N times the molar mass of its monomers i.e.

$$M = NM_{monomer} \tag{1.1}$$

Humans have used polymers without realizing what they have been dealing with. A good example of this is the usage of naturally occurring rubber from the rubber plant. For centuries, humans have relied on such naturally occurring materials for their day to day needs without having a deep understanding of the true potential of these macromolecules. Historically, chemists have been synthesizing polymers/macromolecules since the mid nineteenth century but the field of polymer physics and chemistry became mainstream only in the early 20^{th} century and since then these macromolecules have been extensively studied, researched and used due to their novel physical, chemical, mechanical, and biological properties. The chemical nature of the monomers is one of the principal factors that determines the overall properties of any polymeric system. Another factor is the polymer's microstructure i.e. the typical organization of the monomers along its backbone and it cannot be changed without breaking the covalent bonds linking each component [136]. It is important to note that the degree of polymerization, N is a major factor that determines the overall properties of several polymeric systems. *Oligomers* are polymers with only a small degree of polymerization, typically of the order of $N \leq 20$. Linear polymers typically contain monomers of the order of 20 to 10 billion. As monomers are linked to the backbone of the chains, the physical properties such as the melting and boiling point the polymer system increases quite rapidly.

Another important feature that controls the properties of the system is its architecture. The different architectures manifests into vastly different properties for the

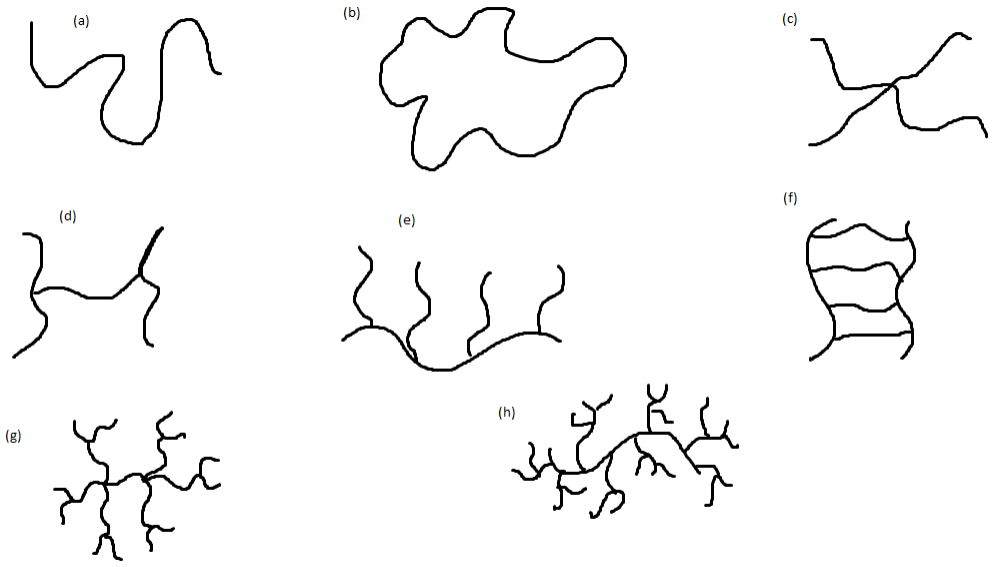

Figure 1.1: Different polymer architectures (a) linear, (b) ring, (c) star-branched, (d) H-branched (e) comb (f) ladder (g) dendrimer and (h) randomly branched

polymeric systems for instance the randomly branched architecture shown in figure (1.1 h) has particular industrial importance and is widely used in the manufacturing of bottles and packaging films. High degree of crosslinking between constituent polymers leads to formation of polymer networks that are useful in manufacturing of soft solids such as erasers and tires [136]. Polymers with only a single type of chemical monomer are commonly known as *homopolymers*, while chains with several different monomer types are referred to as *heteropolymers*. Heteropolymers have unique properties depending on their composition i.e. fraction of the different monomers used during polymerization as well as the sequence with which each one appears in the chain. Many biopolymers present in the human body are heteropolymers. For instance DNA is a heteropolymer consisting of four different types of monomers (nucleotides) while other proteins are made up of 20 different types of amino acids.

Polymers with two or more different types of monomers are known as *copolymers*. The different monomers can come in either an alternating, random, block or grafted sequence. Polymers with two blocks are termed as *diblock copolymers*. Similarly, when there are three blocks the chains are termed as *triblock copolymers* and chains with several alternating blocks are known as *multiblock copolymers*. These various patterns are illustrated in figure (1.2).

An important aspect that is quite unique to single polymer chains is that after polymerization the chains can adopt many different *conformations*. A chain's conformation is basically its spatial structure that is determined by the relative locations of its monomers

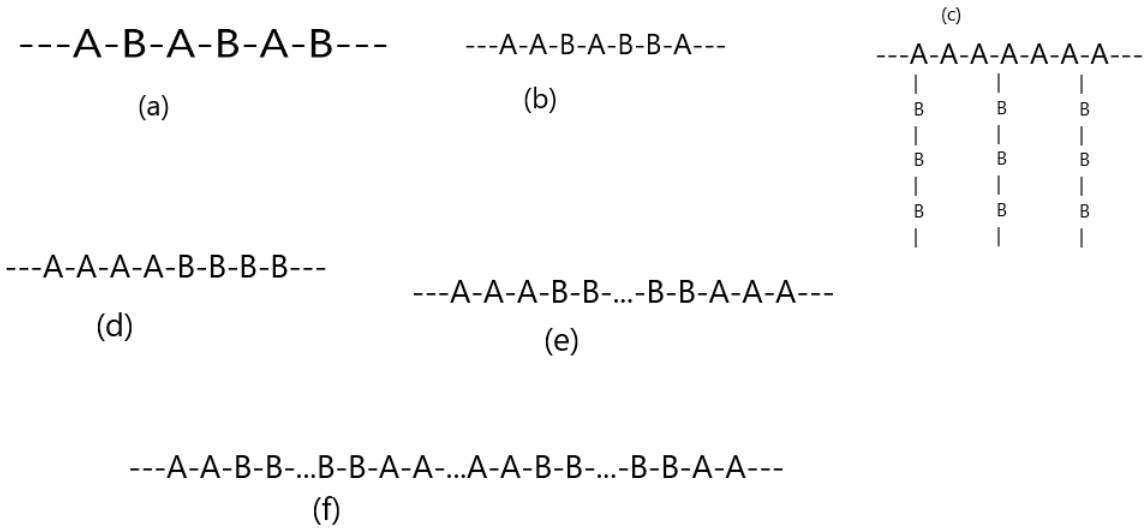

Figure 1.2: Different type of patterns in copolymer chains (a) alternating, (b) random, (c) graft, (d) diblock, (e) triblock and (f) Multiblock

in space and can be specified by giving the position vectors of all the monomers comprising the chain or equivalently by tracing a path formed by all the *bond* vectors along the chain's backbone. The conformations assumed by a single chain depend primarily on three factors, namely its flexibility, interactions between the monomers, as well as interactions of the monomers with the surrounding environment. The size and nature of the monomers also have a drastic impact on properties that the chains tend to exhibit as a whole. As we will see in subsequent sections, the size of monomers plays a crucial role for chains in fluid flows. Depending on the interactions of the monomers amongst themselves as well as with the surrounding, the chains can either be extremely flexible like a thread of silk or be stiff like a piano or guitar string. The monomer interactions can be either attractive or repulsive in nature and the relative strengths of these can vary with ambient temperature. As we can see, even for a single chain there are many degrees of freedom that one can in principle tune to achieve any desirable macroscopic property/effect. Due to such vast features polymers have proven to be extremely useful and are prevalent in numerous industrial and medical applications.

In modern times, the polymer industry has grown far beyond the industries relying on aluminum, copper and steel. Their range of industrial applications far exceed any other material available to humans and are widely used in the manufacturing of adhesives, coatings, foams, films, plastics, textile, automotive parts, electronic devices, optics and so on. For instance, polymer based devices are now being used even in the semiconductor industry for the construction of *organic field-effect transistors* (OFETs) [21, 77]. Due to the recently reported high field-effect charge mobilities [70, 88] in polymer based field effect transistors (FETs), polymers have become an attractive alternative to silicon for the construction of transistors. Moreover, the electrical performance of OFETs has been reported to be either comparable or exceeding that of amorphous silicon [86]. Polymer based semiconductors are becoming increasingly attractive since polymers can be easily

deposited through a solution process in comparison to the expensive ion based implantation methods in use currently. The solution based deposition process is easy to scale-up while minimizing processing costs as demonstrated in [69]. Such properties are making polymer based materials and processes attractive in the semiconductor industry.

Smart/responsive materials are another interesting and novel application of polymers in industrial applications that is increasingly gaining popularity and driving research [160]. Responsive materials as well as structural systems are widely being used today to develop smart devices, sensors and actuators due to their ability to quickly respond to environmental stimuli with a detectable action. As pointed out by Brighenti et al. [26] responsive polymers are capable of producing observable responses under external stimuli and when their behaviour is properly understood and quantified their molecular scale response can be conveniently exploited in various ways to obtain desired macroscopic responses. Since these responses come from their molecular architectures, the arrangement of polymer chains and the nature of embedded active molecules, stimuli-responsive polymers can be tailored to have stimulus specific chemical, electrical, optical and mechanical responses and moreover can be engineered into different forms. Authors in [52, 112] study the underlying molecular mechanisms of such polymers in great detail and look to understand their molecular structures by minimizing the free energy of the whole system. Furthermore extensive research into such materials through molecular dynamic simulations is also being carried out in order to understand the responsiveness of polymers under multiple stimuli. Zhuang et al. ([206]) have done extensive work in understanding multi-stimuli responsive polymers. Coarse-grained molecular dynamics (MD) and dissipative particle dynamics (DPD) simulations have also been carried out in order to understand the large-scale behaviours of such stimuli responsive polymers ([89]) and the challenges therein have been well pointed out.

Apart from the novel industrial applications and research being currently carried out, polymers are also widely used in the medical/healthcare field. For instance, many biomaterials and natural polymers are being used in heart implants, artificial joints, dental implants and so on. Polymer based materials have become significantly more important nowadays in comparisons to other materials since they tend to result in fewer issues when incorporated into dental, neurological and cardiovascular gadgets and are easier to manufacture and last longer. As pointed out in the review works ([14, 93, 111]), the similarities between natural tissues, proteins and synthetic polymers with their long chain architecture make them better representations of natural tissue when compared against metals and ceramics. Due to these similarities in structure and properties, a wide array of materials have been developed that are being actively used in medical devices and procedures. Examples include acrylic cements for orthopedy, facial prostheses, joint surgeries, blood pushes, catheters, cardiac valves, pumps and so on.

Depending on their synthesis or intrinsic properties, certain polymers are biodegradable in nature. Such polymers are ideal candidates for developing therapeutic devices such as temporary prostheses, large implants such as bone screws, three-dimensional porous structures as scaffolds for tissue regeneration/engineering and as nano/micro sized drug delivery vehicles. For any biodegradable material to be used in biomedical applications, it must first be considered safe such that it does not evoke a sustained inflammatory or toxic response from the body upon implantation. Moreover, to be considered effective

the degradation time of the material should match the healing/regeneration time and the degradation should be non-toxic and be able to be metabolized and safely cleared from the body. Each of these requirements necessitates that the materials with carefully tuned physical, chemical, biological and degradation properties in order to prove effective. Given that many natural and synthetic polymers are capable of undergoing degradation by hydrolytic or enzymatic processes, they are being actively researched and considered for the last decade or more as viable materials in biomedical applications ([40, 74, 92, 103, 129, 194]).

Apart from the importance of polymers in industrial and biomedical applications, polymers play a key role in many vital functions within the human body itself. Proteins, which are essentially amino acid polymers arranged in a three dimensional folded structure, are the major structural components of many tissues and are one of the most important class of bio-molecules identified to date. Another crucial protein that is present in our circulatory system is the *von Willebrand factor* commonly known as VWF and is necessary to stop bleeding under high shear stress conditions as found in small blood vessels. In the following section we give some background on our first work involving polymers in shear flows and the effect monomer size has on such single chains.

1.1.1 Polymer margination in shear flow

VWF fibers and blood platelets play a crucial role in initiating blood clotting in the case of a rupture to small blood vessels ([36, 43, 108, 132, 138, 146]). VWF is known to mediate the adhesion of platelets to sites of vascular damage by binding to specific platelet membrane glycoproteins and to constituents of exposed connective tissue. It has been found that these binding activities are driven by hydrodynamic shear stresses and activate the VWF's binding potential. Schneider et al. [146] have studied the behaviour of single VWF chains by using microfluidic devices as well as through hydrodynamic computer simulations and have found evidence that an increase in hydrodynamic shear stress in the vicinity of single VWF chains activates its binding potential which in the presence of collagen eventually leads to the counterintuitive phenomena of enhanced chain adsorption under strong shear flow conditions. Intuitively, one might think that at high shear rates, as found in small blood vessels, hydrodynamic lift forces near surfaces will inhibit adsorption of objects from the blood onto arterial walls. Blood platelets and other vesicles might tend to roll and detach easily and most importantly remain unbounded as shear stresses are increased further [192].

However, the experimental evidence on blood platelet adhesion in small arteries have shown to contradict this behaviour. VWF mediated platelet adhesion is strongly enhanced under high shear flow conditions as pointed out by Ruggeri in [137]. This leads to an interesting research topic on the dynamics and migration properties of polymers in shear flows near surfaces. For instance a good understanding of the chain's dynamics and migration tendencies in flows is crucial for applications such as targeted drug delivery agents, shear activated polymeric systems [29, 57] and self-healing smart materials to name a few.

As mentioned earlier, VWF is one of the largest polymeric molecules with abnormally large monomer units ($\approx$ 70 nm long axis and $\approx$ 10 nm along short axis) found in the

blood plasma and is known to migrate towards blood vessel walls under high shear rates. Schneider et al. in ([146]) were able to directly visualize the chain unfolding i.e transitioning from a globular conformation to a linear stretched one in response to increase in shear flow as seen in the figure (1.3).

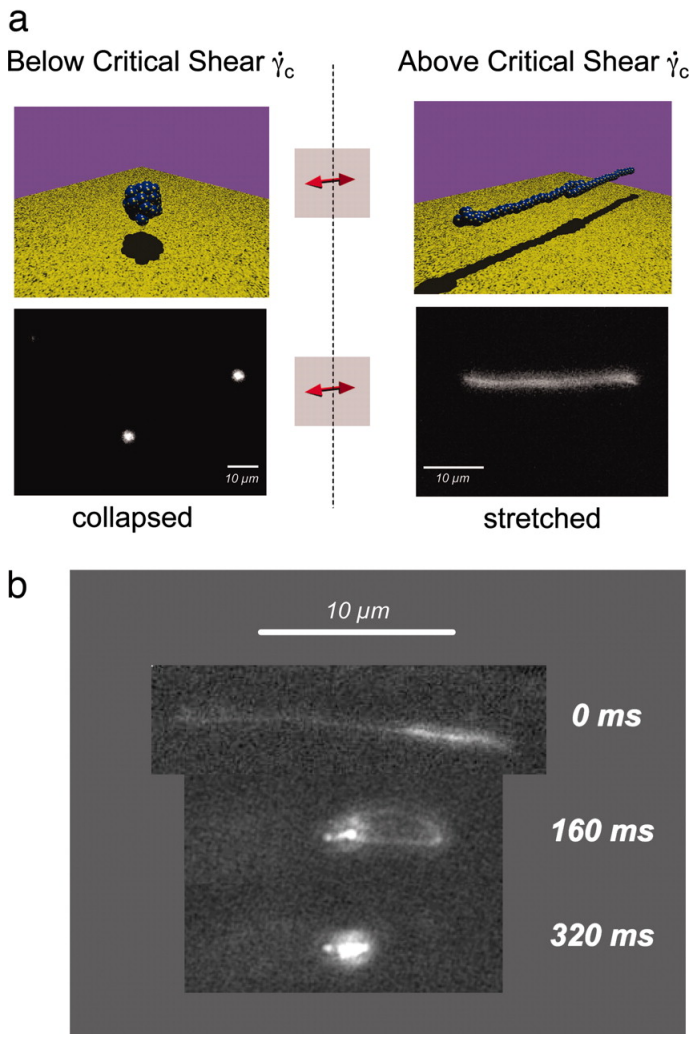

Figure 1.3: Dynamic conformation change of VWF under shear flow. Upper images are graphical illustrations of the globular-stretching transition whereas the bottom figure shows the fluorescence images of a video sequence captured by the authors at 25 frames per second of the VWF below and above the critical shear rate $\dot{\gamma}_c$. As time progress in the experiment, the shear rate is dropped and it can be seen that the single VWF fiber collapses back to its initial globular conformation. Reprinted under the PNAS Rights and Permissions for non-commercial use from Ref. ([146]). Copyright (2007) National Academy of Sciences

They also reproduced such a transition by the use of computer simulations and were able to demonstrate that beyond a critical shear rate i.e. $\dot{\gamma}_c$ the chains abruptly underwent a transformation from a globular state to a stretched conformation as seen in figure (1.4). Other works based on hydrodynamic simulations of single chains in shear flows by Katz

et al. ([5–7]) and Radtke et al. [133,134] have also reproduced such transitions exhibited by their chains. Most importantly, Schneider et al. in ([146]) have pointed out that the VWF's counter-intuitive response to shear stresses can be tracked back to its extremely large monomers. From their computer simulations and scaling analysis they also found that the critical shear rate beyond which the polymer undergoes the transition from a globular conformation to an elongated state was quite sensitive to the effective monomer size a rather than the polymer length.

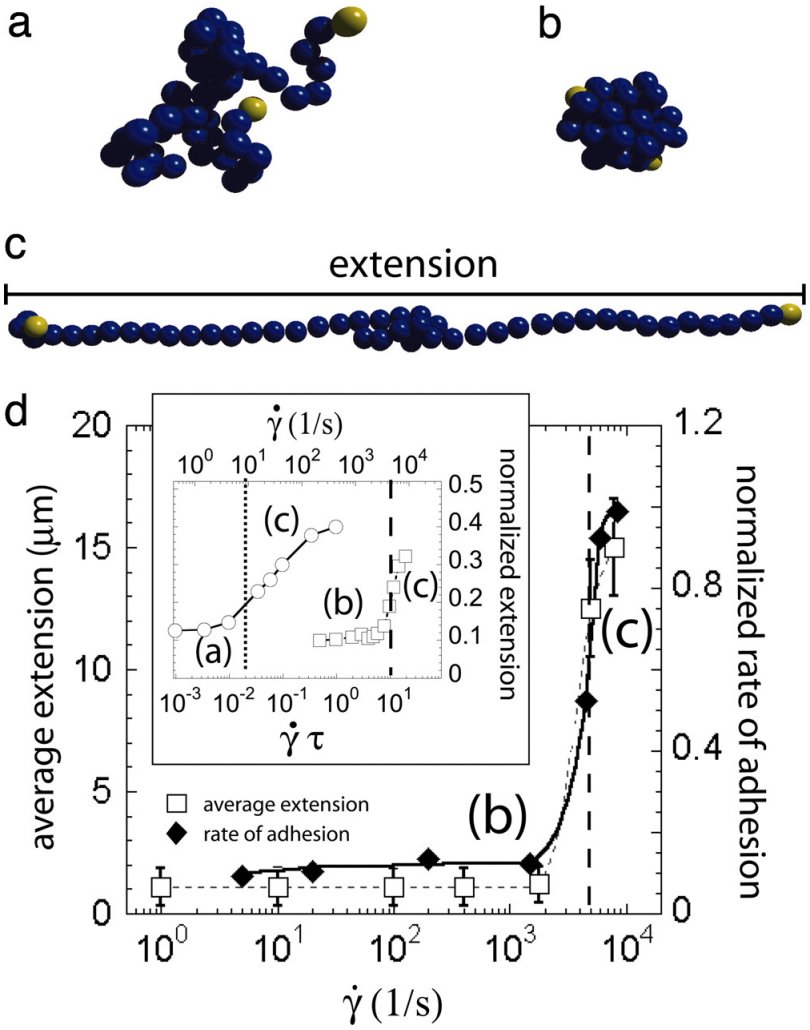

Figure 1.4: The top two figures are graphical representations of the different conformation of a single linear polymer (globular/elongated in shear). The bottom graph with insets shows the experimentally determined average extension (open squares) and the normalized rate of adhesion (filled diamonds) of the VWF multimers as a function of shear rate. The inset shows the results obtained of the same via hydrodynamic computer simulations of a 50-mer as a function of the dimensionless shear rate $\dot{\gamma}\tau$. Reprinted under the PNAS Rights and Permissions for non-commercial use from Ref. ([146]). Copyright (2007) National Academy of Sciences

From their experimental and simulation results, Schneider et al. concluded that the

VWF's abnormally large monomer size and shape play an important role in its elongation in high shear flows. In our work, as presented in subsequent sections, we show that the large monomer sizes play an important role during a chain's margination towards surfaces [1] at high shear rates.

Neutron scattering experiments have confirmed VWF monomers are in the shape of a prolate ellipsoid with dimensions 70 nm and 10 nm along its major and minor axes, respectively ([157]). These numbers show that the monomers are indeed quite large relative to other polymers found in the human body and as we will see from the results of our work large monomer sizes in chains prove to be crucial for margination of chains towards surfaces in shear flows.

Following their analysis of shear induced unfolding of the VWF multimers, the surface adsorption/adhesion properties of the same was also studied. Schneider et al. and others ([7,57,108,146,155,156]) also found that the VWF chains tended to adsorb onto collagen coated surfaces at elevated shear rates. Contrary to popular belief where higher shear rates should reduce chain adsorption onto surfaces, the adsorption of VWF multimers increased and formed a network as more and more chains adhered on the surfaces. This was attributed to the fact that, as the VWF chains elongated in shear flow that exposed more binding sites thus strongly increasing their adsorption tendency. As the adsorbed VWF network grows under shear, this provided a sticky interface for blood platelets to adhere to, thus initiating the blood clotting cascade under normal conditions.

The shear induced elongation and adsorption has also been studied quite extensively by Brownian dynamics simulation with hydrodynamic interactions included via the *Rotne-Prager* (RP) tensor approximation [5, 7, 133, 134, 155, 156]. In ([5]), the authors have argued that anisotropic nature of the hydrodynamic drag force felt by a sphere near surfaces leads to enhanced polymer chain elongation at lower shear rates. In ([133, 156]) the authors have investigated the adsorption phenomena of polymer chains in shear flows onto surfaces to be mediated by long lived *catch-bonds*[2] [174,175]. In their Brownian hydrodynamics simulations apart from the monomer-monomer interactions, the authors described the monomer surface interaction via stochastic bonds in order to mimic a catch bond type of interaction between the polymers and the surface. The authors demonstrated that once the polymer moves towards the surface, and elongates due to increased hydrodynamic drag forces more monomers from the chain become readily available to form stochastic bonds with the surface and thus adsorb at higher shear rates. Although, the authors were able to reproduce shear induced adsorption over a small range of shear rates, the effect of monomer size on the chain's migration towards the surface still remained unaddressed. Sing et al. in [156] mentioned that on occasion when a vWF molecule interacts with the surface, the pathways through which it could unbind get suppressed. Their work showed the importance of catch bond type interactions between the chains and the surface, but the issue of chain margination was left unaddressed.

Apart from polymers, recent works involving studying the margination tendencies of micro/nano sized particles in blood flow at different shear rates for drug delivery purposes

[1] tendency to migrate towards surfaces

[2] A catch bond is type of a noncovalent bond whose dissociation lifetime increases with tensile force applied to the bond

have addressed the effect of particle size and shape on their overall migration tendency. Lee *et al* [85] through capillary flow experiments observed that smaller nano/micron sized particles appeared to be more uniformly distributed throughout the tube in comparison with particles of larger sizes. Furthermore Muller *et al* [109], through 2D & 3D DPD (dissipative particle dynamics) and smoothed DPD (smoothed DPD) simulations showed that larger sized particles marginated more in flow in comparison to smaller particles. They constructed the probability distributions of finding a particle within a certain distance from the surface and found that the margination probability decreased with particle size. The observations discussed so far highlight the importance of the role of hydrodynamic interactions in shear flow, and the particle's size and shape in determining its overall margination tendency.

In light of these studies, in our work we primarily look to address the issue of chain margination towards surfaces in shear flow as a function of the monomer size. We address the issue of lateral migration of polymer chains in flows via hybrid LBMD (Lattice Boltzmann-Molecular Dynamics) so that the full gamut of hydrodynamic interactions near the surface as well as in the channel bulk are adequately captured. From our results, we were able to note that larger monomer sized chains marginated better. Despite only a weakly attractive potential at the surface, larger monomer sized chains showed greater margination tendencies in comparison to chains with smaller monomers. The equilibrium behaviour of both chains were exactly the same as they both escape the surface potential equally well. Due to this observation, we concluded that margination is a dynamic effect in shear flows that is ultimately coupled to the size of the monomers. In [5, 7, 133, 134, 155, 156], where Brownian dynamics with a *Rotne-Prager* type approximation for hydrodynamic interactions between monomers was used the margination effect could not be conclusively reproduced. Given that the RP tensor models pairwise hydrodynamic interactions between monomers while effectively treating them as point particles, the full gamut of hydrodynamic interactions throughout the chain as well as between chain and the surface is not captured sufficient well. However, since we used the LB method to effectively simulate the thermal fluid flow in a channel, the hydrodynamic interactions between the chain and surface as well as between monomers is properly captured.

1.1.2 Polymer melts and nanocomposites

Polymer solutions and melts are another novel area in polymer physics that has seen enormous growth and research attention over the past decade. Given their highly viscous and non-Newtonian flow behavior, polymer solutions and melts have become extremely relevant in many engineering and industrial processing techniques. As pointed out in [136], polymeric liquids are primarily of two kinds (i) polymer solutions and (ii) polymer melts. Polymer solutions are simple in the sense that they are obtained by dissolving a polymer into an existing solvent. Examples of a few polymer solutions include wood surfactants (varnish) and polyurethane coatings. Polymer solutions, depending on the mass concentration of the polymers added, can be largely categorized into two distinct categories (i) *dilute* and (ii) *semi-dilute*. The mass concentration, c is defined to be the ratio of the total mass of a polymer dissolved in a solution and the total volume of

the solutions [136]. Typically however, the distinction between a dilute and semi-dilute polymer solution is reported using the *volume fraction*, ϕ of the polymer. The volume fraction ϕ of a polymer in a solution is given by the ratio of its *pervaded volume* to the total volume of the solution. The *pervaded* volume of a polymer is simply the total volume of the solution spanned by the chain is is proportional to a measure of the chain's size, R i.e.

$$V \approx R^3, \tag{1.2}$$

where R is a suitable measure of the polymer's size in the solvent. Now using this measure, the *overlap* volume fraction, ϕ^* is defined as the fraction of occupied volume of polymers per unit volume of solution. If the volume fraction ϕ of a polymer solution is equal to the overlap volume fraction, ϕ^*, then by definition this defines a solution where the pervaded volumes of marcomolecules densely fill space. As illustrated in figure (1.5), all solutions with volume fraction, ϕ less than the overlap volume fraction ϕ^* i.e., $\phi < \phi^*$ are considered dilute since in such cases the average distance between chains is larger than their size. Hence in dilute solutions individual polymer chains are able to freely swim and diffuse with minimal influence from other chains. Due to this the overall properties of the solution remain close to that of the pure solvent (no chains) with only minor modifications.

In the other case, where the volume fraction is greater than the overlap i.e. $\phi > \phi^*$, the solutions is considered semi-dilute. Even those the volume fraction is greater than the overlap threshold, the actual values are still quite small i.e. $\phi << 1$ and most of the volume in the solution is still occupied by the solvent. As seen from figure (1.5 b), the pervaded volumes are quite close together and due to the vast number of conformations polymer chains can assume, their overlap with each other drastically influences the overall properties of the solution [136]. This entails that introducing even a small amount of polymer to a semi-dilute solution can dramatically change the solvent's intrinsic properties such as its viscosity. As the volume fraction increases further properties of polymer solutions and melts start to overlap.

In the absence of any kind of external solvent, polymer molecules form a liquid state referred to as a *melt*. Polymer melts are unique polymeric liquids that are well above their glass transition and melting temperatures. Some novel properties of melts is that they exhibit different properties over short and long time scales [136]. For instance, polymer melts typically behave like purely elastic objects over short time scales, they retain memory of their original shape and structure and quickly recover from small and quick deformations applied to to them. However, small deformations applied over a longer period of time cause them to behave similar to a viscous fluid and gradually flow over surfaces. Due to the time dependent nature of the mechanical and rheological properties, polymer melts are known to be *viscoelastic*. A very common example of a polymer melt is silly putty since over short time scales or quick deformations it responds like a rubber ball but if left under the influence of gravity it will behave like a highly viscous fluid and gradually flow over surfaces. Corn starch is another good example of a viscoelastic substance. For instance, if one vigorously disturbs it i.e. short time scale perturbations, the material tends to recover quite quickly but introducing slow, gradual deformation to it for instance moving a fork over it slowly for a minute or more, it starts to behave like

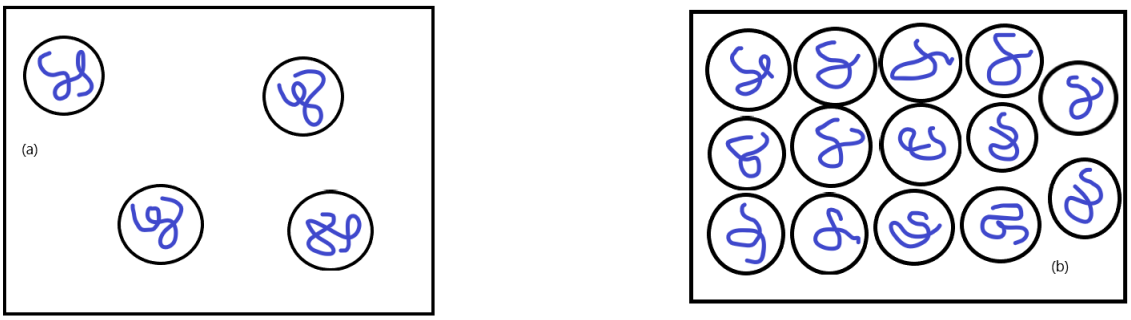

Figure 1.5: Illustrations of the different kinds of polymer solutions (a) **Dilute**, $\phi < \phi^*$, (b) **Semi-dilute**, $\phi > \phi^*$. The circles around each individual polymer is simply to illustrate the *pervaded* volume occupied by each individual chain in the solution. In the *dilute* solution, we can see that the distance between any two chains is on average larger than the equilibrium size of the chain, whereas in the *semi-dilute* case the chains are packed a lot closer to each other and the pervaded volumes of each overlap in some cases. The polymer solvent is still referred to as semi-dilute because the solvent's volume is still far greater than the pervaded volumes of the individual chains

a viscous Newtonian fluid.

Other properties of melts include *shear-thinning*. This effect is predominantly observed when polymer melts are put under large shear strains. Under such strains, the polymers near surfaces stretch out and align themselves along the direction of the shear. As more and more chains become aligned, slipping between different polymer layers begins to occur as more and more chains become un-entangled. Due to this, the melt begins to flow rapidly despite its originally high viscosity. At low shear strains, the relative elongation of the chains in the melt is low and the entanglement between chains is still high; viscosity of the melt remains relatively high and shear thinning does not occur. However this effect becomes predominant under large shear stresses since the chains in the melt give in and get aligned parallel to the direction of the applied strain. Shear thinning can be observed when painting surfaces using brushes. Given that the paints are largely polymer solutions, they exhibit shear thinning due to which the paint can be smoothly applied on surfaces via brushes. The brush induces a high shear strain which causes the paint to move smoothly over the surface. However once applied, the only predominant force acting on it is gravity which is a weak force and does not induce any significant shear strains on the melt, causing it to remain adhered on the surface. Another example where this effect materializes is in the use of ball point pens. The ink is gets squeezed through the ballpoint, and when it is moved over a surface shear thinning occurs and the ink flows smoothly.

Given that polymer melts by themselves have such novel and useful applications in today's world, since the discovery of carbon nanotubes (CNTs) research on polymer nanocomposities (PNC) has seen tremendous growth. CNTs have displayed excellent mechanical strength, electrical conductivity and magnetic properties, their potential to be used in technological applications cannot be overstated. PNCs are materials comprised of

polymers and different nanoscale fillers and have been shown to exhibit enhanced macroscopic properties such as improved mechanical durability and electrical conductance compared to pure polymeric melts. Moreover, mixtures of anisotropic fillers, especially nanofibres (NFs) and nanotubes (NTs) in polymer matrices have shown a great potential to produce high performance materials and therefore have received a lot of attention from scientific and engineering communities ([2,10,62,94,106,107,123,139,167,205]). On top of the intrinsic properties of the nanorods, their distribution and orientation in the polymer matrix, interaction with the matrix, and aspect ratio play a crucial role in the overall performance of the material ([3,31,80,126]). Larger aspect ratio of the nanofillers are known to increase dispersion and mechanical properties of the polymer nanocomposite [31, 126] and previous computational works have studied the effect of nanorod length [142, 178].

In ([95]), the authors have carried out extensive coarse-grained molecular dynamics simulations of polymer nanocomposites with nanorods with different type of surface functionalization (homogeneous/patchy). The authors modelled the surface chemistry of the nanorods by using isotropic and directionally dependent interactions between the nanorods in the system respectively. In their work, the showed how the PNC's morphology is impacted by the design of the nanorods and fillers. They looked at the effect of varying nanorod aspect ratios and surface functionalization chemistry has on the overall PNC's morphology and found that for PNCs with 10 vol % nanorods with an aspect ratio ≤ 5, the rods percolated with directional nanorod-nanorod attraction whereas they phase separated under an isotropic nanorod-nanorod interaction. This implies that the aspect ratio of the nanorods and the surface interaction potential between the rods and the polymers play a crucial role in determining the overall equilibrium properties of the melt. For nanorods with higher aspect ratios, the authors found that both types of attraction between the rods resulted in PNC morphologies where the rods were aggregated. This was attributed to the entropic driving forces that caused the longer nanorods to form orientationally ordered aggregates. The different morphologies are well illustrated in the following figure (1.6) for nanorods of varying aspect ratios i.e. $L = 3d, 5d, 15d$ where d is the diameter of a single monomer from the nanorods. The authors also reported that for concentration of nanorods in the melt less than 20 vol % the average matrix polymer conformation remained unperturbed, however the *interfacial* polymers i.e. the chains within the vicinity of the nanorods were on average in elongated conformations and statistically different from the bulk chain conformations.

In our work, we also observed such similar morphologies as we worked with polymer chains and nanorods with fixed lengths throughout the simulations and focused on dispersion patterns of the nanorods, their alignment, and the effect of polymer-rod attraction strength on these such percolation patterns. One of the main barriers in enhancing properties of polymeric materials through adding NTs or NFs is the formation of aggregates which leads to problems such as non-uniform stress distribution and slippage [32, 198]. In spite of the development of preparation and processing techniques such as in situ polymerization and surface modification that have been successful in promoting better dispersion of nanorods in a polymer matrix ([3, 51, 56, 67, 96, 135, 139, 149, 183, 198, 204]), there is a need for a deeper understanding of the underlying physics, that results in the observed phase behaviour of nanorod-polymer systems. As a result, it has been under an extensive examination both theoretically ([20, 54, 87, 165] and computation-

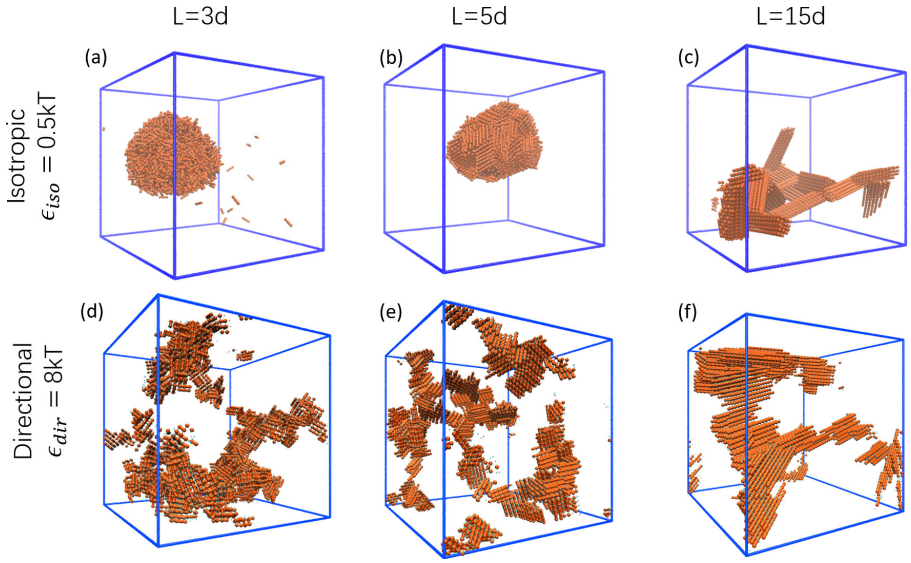

Figure 1.6: Snapshots of nanorods for PNCs with rod concentrations $\phi_r = 0.10$ and (a) $L = 3d$ nanorods with isotropic nanorod-nanorod attraction and $\epsilon_{isotropic} = 0.5k_bT$ (b) $L = 5d$ nanorods with $\epsilon_{isotropic} = 0.5k_BT$ (c) $L = 15d$ nanorods with $\epsilon_{isotropic} = 0.5k_bT$ (d) $L = 3d$ nanorods with directional nanorod-nanorod attraction and $\epsilon_{dir} = 8k_bT$ (e) $L = 5d$ nanorods with $\epsilon_{dir} = 8k_bT$ (f) $L = 15d$ nanorods with $\epsilon_{dir} = 8k_bT$. Reprinted with permission from Ref. [95]. Copyright (2021) American Chemical Society

ally [45, 59, 60, 95, 104, 140, 143, 159, 178]). Savenko and Dijkstra conducted Monte Carlo simulations of a polymer-nanorod system using an effective Hamiltonian that accounted for the effect of the polymer matrix implicitly [143]. The polymers were assumed to be non interacting in this study. Their results showed rod packing, and formation of nematic aggregates. Although understanding non-absorbing systems provide a great insight into depletion effects, they are not common in practical applications due to high number of aggregates and poorer performance.

Surface treatments like functionalization or adding sizing agents not only results in more uniform dispersion of nanorods but also improves the interfacial interactions between the rods and the polymer matrix which is critical for achieving good mechanical properties [73, 126, 169, 201, 202]. Stronger interfacial adhesion facilitates the stress transfer from the matrix to the nanorods thus improving the interfacial shear stress (IFSS) strength and performance of the nanocomposite [13, 90, 125, 197, 199]. Therefore, it is interesting and useful to investigate polymer nanocomposite (PNCs) systems with attractive polymer-rod interactions. By means of Monte Carlo (MC) and MD simulations, Toepperwein et al. studied a system of nanorods in an entangled polymer matrix where all interactions (i.e. rod-rod, polymer-polymer, and rod-polymer) were attractive [178]. The polymer-nanorod interactions were stronger to mimic a realistic and common system. They observed a well-dispersed mixture for shorter rods while the 16-mer rods phase separated to aligned aggregates. Our results, for an unentangled melt, which are discussed in section (4.0.3), manifest similar patterns of highly-ordered rod droplets. Another interesting observation by Toepperwein et al., which was observed in our simulation

as well, was the presence of polymer chains between the rods within the droplets despite their packed structure.

In a molecular dynamics study, Gao et al. investigated the effect of inter-component interaction strength, temperature, filler concentration, cross-linking density, external shear, aspect ratio, and nanorod grafting on the dispersion patterns and kinetics [45]. For a system in which the polymers were attracted to both rods, and with all other interactions being purely repulsive i.e. polymer-polymer and rod-rod, they found that there exists an optimum moderate polymer-rod attraction strength that promotes good dispersion. They categorized the source of the formation of aggregates to polymer-bridged, and direct contact. As illustrated in the following figure 1.7, we can see the different reported rod aggregation patterns observed by the authors at different polymer nanorod interfacial interaction strengths. On the basis of their simulations the authors concluded

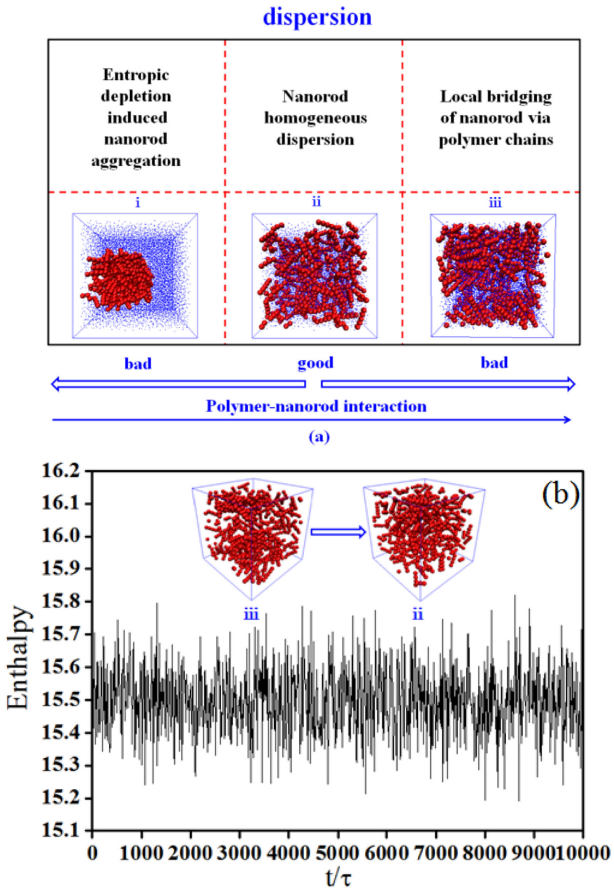

Figure 1.7: (a) Nanorod dispersion patterns observed as a function of the polymer nanorod interfacial strength (b) Change in system's enthalpy monitored during the dispersion process as the polymer-nanorod interaction strength ϵ is varied from $\epsilon = 12.0$ to $\epsilon = 2.0$. Reprinted with permission from [45]. Copyright (2014) Elsevier Ltd. All quantities plotted here are dimensionless.

that at weak polymer nanorod interaction, the macroscopic phase separation between the two can happen. Nanorod dispersion was seen to increase with increasing interaction

strengths as good dispersion of the rods throughout the melt was observed. At strong interaction strengths however the authors reported that the polymers aggregated via one or two polymer bead layers and local bridging of the nanorods via polymer chains occured. These three stages are clearly marked in figure 1.7. The transition from state (i) to (ii) in figure 1.7 can be understood on the basis of interfacial enthalpy gains i.e. given the attractive interaction between the polymers and rods, as the interaction strength between the two is increased, enthalpy gains increase as well. However the authors reported that the state transition from (iii) to (ii) in figure 1.7 was entropy driven as the interaction strength was changed from $\epsilon = 12$ to $\epsilon = 2.0$ from a suitable chosen equilibrium bridged conformation. As seen from figure (1.7 b) in this process the system enthalpy remained unchanged which goes to suggest that the transition back is primarily entropy dominated. This meant that one single chain tended to adsorb several nanorods in order to avoid too much loss of the chains entropy. Based on their observation at high interfacial interaction strengths the nanorod aggregation is seemingly caused because of polymer-rod bridging effects. However, in our work we will show later sections, for the range of attractive interactions studied here, increasing attractive strength only results in better dispersion, and smaller aggregates and polymer-bridging does not seem to be the mechanism behind formation of clusters.

In a recent article, Lu, Wu, and Jayaraman conducted MD simulations on polymer-rod nanocomposites with homogeneous and patchy surface to shed light on the effect of nanorod design on final PNC morphology [95]. In this study, the polymer-polymer, and polymer-nanorod interactions were purely repulsive while the nanorods interacted with an attractive potential. For short nanorods, they observed percolated nanorod structure for the system with patchy rods whereas the simple nanorods phase-separated to a cluster. In the case of long nanorods, both designs exhibited formation of ordered aggregates, either finite-sized or percolating. They also looked into the conformation of polymers at the nanorod interface where they discovered that although the average radius of gyration (R_g) of the polymers remained the same as that of a pure melt, the interfacial chains stretched out and expanded. We touch on the interfacial behaviour of polymer chains for a system with polymer-nanorod attractions in section (4.0.3).

The dispersion patterns of nanorods in a pool of attracting polymer chains is a less explored field and is the focus of our work on polymer melts. Using MD, we simulated a polymer-nanorod melt where all interactions were repulsive except for polymer-rod and looked at the dispersion and orientation of rods as well as the conformation of polymer chains at the rod interface. In polymer melt section (4.0.3) of this dissertation, we go over the simulation setup and details and report our findings. We also devote certain sections of the same to describe the dispersion patterns of the rods by means of auto-correlation of a number density and rod-rod distances and then delve into orientational behaviour of the nanocomposite melt.

Chapter 2

Methods

In this chapter we give an overview of the different scientific tools, techniques and simulation methodologies we used in our work on polymers in flows and melts. In section (2.1) we give a broad overview of what MD is and how using it one can model, simulate and study different physical systems. To this end we give an overview of the classical equations of motion and how they are integrated along with a force field to simulate the dynamics of a physical system. We discuss different interaction potentials and force-fields used in MD simulations as well as the different numerical techniques used for integrating the classical equations of motions in a stable manner. We give a simple overview of the steps involved in numerically integrating the motion of a system of particles that can be used to easily implement a simple program.

In section (2.2) we provide a overview of the Lattice-Boltzmann framework that is extensively used to simulate fluid flows as an easy alternative to conventional CFD methods (i.e. solving the Navier-Stokes equations numerically). We present the various algorithm details associated with this framework as well as how it is deeply rooted in Boltzmann's kinetic theory. Throughout this section we discuss how one can from this mesoscopic framework, extract macroscopic observables such as fluid density and momentum. We also present steps that can aid anyone in quickly writing a simple program to simulate fluid flow using the Lattice-Boltzmann (LB) methodology. In later sections, we also present methods and techniques used to simulate the interaction between fluids and rigid bodies and such interactions can be modeled. The inclusion of thermal fluctuations in a fluid is also presented along with discussions around how the fluid-rigid body interactions can be tuned in to reproduce the correct temperature.

In section 2.1 we begin by giving a broad overview of the subject at large with a quick overview on how one studies and models physical systems, materials and objects through the use of computer simulations. In sections 2.1.1 and 2.1.2 we present the theoretical foundations over which the MD framework is built upon as well as explain the ergodic hypothesis that proves to be extremely helpful when inferring observables from simulations using statistical analysis. In the next several sections 2.1.4-2.1.6 we explain in detail the different inputs needed to successfully run MD simulations. Given the goal is to understand the physics underlying several mechanisms observed in physical systems, accurately modelling the interactions between the system's constituents is extremely important. In these sections we elaborate on the multitude of interaction potentials and force fields commonly used in coarse grained and fully atomic MD simulations. Since we are running computer simulations to model physical systems, MD is entirely reliant upon efficient and numerically accurate integration schemes. In sections 2.1.7 we elaborate on the different numerically integration schemes available for this purpose and provide a short analysis on how they can be derived and the accuracy expected from each of those methods. In the final sections i.e. 2.1.8 we address the issue of boundary conditions in MD simulations and present details on the most commonly used periodic boundary conditions and the minimum image convention as they are really important when modeling really large systems through a small, computationally feasible representative sample. We additionally note that in presenting the material in this chapter we closely follow the format used by Schneider et al. in [145] and cite their work suitably throughout the chapter.

2.1 Molecular Dynamics

Molecular dynamics is the science of simulating the time evolution of a system of particles by simply numerically integrating the system's equations of motion whilst considering the system's boundary conditions. Generally speaking MD simulations treat particles as classical atoms and generate microscopic level data such as the positions, velocities and forces of all particles in the system. Macroscopic observables such as pressure, temperature, transport coefficients are later calculated using statistical mechanics. In order to calculate the microscopic trajectories of the particles involved, MD simulations require one to specify the potential and force fields under which the particles/atoms interact with each other. Once the potential/force fields have been completely specified, the time evolution of the system is, in principle, deterministic under the laws of classical mechanics. It is important to mention that the accuracy of the results of an MD simulation is closely tied to how well the potential/force fields used truly capture all the quantum mechanical/classical interaction effects exhibited by a true system.

MD simulations/techniques have been widely used in several branches of sciences and engineering. For instance, determining reaction rates coefficients for polymer chemistry [91, 102, 163], protein folding [68, 75, 144], solid state structures [16, 168, 200] and material science are just a few examples of where MD simulations have yielded significant insight into real processes. A disadvantage of classical force fields/potentials is that they typically confine the simulations to single molecule connectivity. Chemical processes

such as bond breaking/formation are harder to model since inherently such processes are quantum mechanical in nature. Alternatives to such limitations exists where classical MD simulations are combined with electronic structure where the forces are computed on the fly from an electronic structure calculation and consumed in the MD simulation as it progresses. Such methods are commonly known as *ab initio* molecular dynamics and specifying a potential/force field is not required. Although such methods are quite accurate in modeling certain chemical processes, they typically incur a significant computational overhead that increases quite quickly with the system size. [145]

2.1.1 Basic Formulation

As noted earlier, the key elements in a MD simulation are (i) the interaction potential/force fields for the particles and (ii) the equations of motion governing the dynamics of the system. In classical MD, one simply follows **Newton's** laws when considering the time evolution. In the case of a system of N classical particles, the equation of motion of the ith particle can simply be expressed as

$$\mathbf{F}_i = m_i \mathbf{a}_i \tag{2.1}$$

Here m_i is the mass of the ith atom in the system and $\mathbf{a}_i$ is its acceleration and $\mathbf{F}_i$ is the net force acting upon it due to its interactions with the other particles/atoms in the system. Equivalently, one can also solve the system's Hamilton equations of motion and determine each particle's position $\mathbf{r}_i$ and momenta $\mathbf{p}_i$

$$\dot{\mathbf{p}}_i = -\frac{\partial H}{\partial r_i} \tag{2.2}$$

$$\dot{\mathbf{r}}_i = \frac{\partial H}{\partial p_i}, \tag{2.3}$$

where H is the Hamiltonian of the system given as a function of all the particle's position and momenta

$$H(\mathbf{p}_i, \mathbf{r}_i) = \sum_{i=0}^{N} \frac{\mathbf{p}_i^2}{2m_i} + V(\mathbf{r}_i), \tag{2.4}$$

Given the interaction potential $V(\mathbf{r}_i)$, the force on the ith particle can easily be expressed as the negative gradient of V with respect to the particle's coordinates i.e

$$\mathbf{F}_i = m_i \mathbf{a}_i = -\nabla_i V \tag{2.5}$$

Given the forces can be computed using (2.5), at each timestep forces on all atoms in the system are first determined. From the forces, using any stable numerical integration scheme, the position and velocities of all the particles are then updated. It is to be noted that the forces acting on the particles are assumed to be constant over a timestep, Δt. These basic steps are repeatedly over and over again for the duration of the simulation.

2.1.2 Ergodic Hypothesis & Statistical Ensembles

MD simulations generate microscopic quantities such as position, velocities and forces acting on each particle/atom of the system. To extract macroscopic observables from such trajectory data, *statistical mechanics* needs to be used. Based on the ensemble concept, it is sufficient to average over a large number of independent microstates of the system to obtain the macroscopic observables such as pressure, temperature, transport coefficients etc. Ensembles are typically characterized, by thermodynamic variables such as pressure (P), temperature (T), volume (V), energy (E), particle number (N) or chemical potential (μ). Depending on which of the thermodynamic variables are held constant during simulations, the ensembles are largely categorized under three different frameworks.

The *microcanonical* ensemble is characterized by constant particle number (N), constant volume (V) and constant energy (E) and is commonly referred to as the NVE ensemble. The case where the particle number (N), volume (V) or pressure (P) and temperature (T) are held constant is referred to as the *canonical* or the NVT/NPT ensemble respectively. The *grandcanonical* or μVT ensemble refers to the case where the chemical potential (μ), volume (V) and temperature (T) are held constant.

Now, let us consider a system with N particles in a region with fixed volume V evolving as per Hamilton's equations of motion. Taking the time derivative of the Hamiltonian of such a system we get

$$\frac{dH}{dt} = \frac{d}{dt}\sum_{i=0}^{N} \frac{\mathbf{p}_i^2}{2m_i} + V(\mathbf{r}_i) \tag{2.6}$$

$$= \sum_{i=0}^{N} \left[\frac{\partial H}{\partial p_i}\dot{\mathbf{p}}_\mathbf{i} + \frac{\partial H}{\partial r_i}\dot{\mathbf{r}}_\mathbf{i}\right] \tag{2.7}$$

In (2.7) it is assumed that the masses of the individual particles do not change over time. Now substituting (2.3) into (2.7) we get

$$\frac{dH}{dt} = \sum_{i=0}^{N} \left[\frac{\partial H}{\partial r_i}\frac{\partial H}{\partial p_i} - \frac{\partial H}{\partial p_i}\frac{\partial H}{\partial r_i}\right] = 0 \tag{2.8}$$

From (2.8) we can see that for such systems the Hamiltonian, H is conserved and the total energy (E) in the system remains constant. Now as the system evolves over time, its $3N+1$ dimensional state will generate a trajectory in phase space. Since the energy of the system is constant i.e. $H(\mathbf{p}, \mathbf{r}) = E$, this limits all the accessible states of the system to a constant energy hyper-surface in phase space. The assumption here is that given an infinite amount of time, the system will sample all the points on this hyper-surface. This is known as the *ergodic hypothesis*, which simply states that any system evolving under Hamilton's equations of motion will eventually sample all accessible microstates. Thus, statistical averages of any observable A over a large number of independent ensembles can safely be replaced by time averages over the system's trajectory i.e., $\langle A \rangle_t = \langle A \rangle_{ensemble}$ where $\langle A \rangle_t$ is given by

$$\langle A \rangle_t = \lim_{\tau \to \infty} \frac{1}{\tau} \int_{t=0}^{\tau} A(\mathbf{p}(t), \mathbf{r}(t)) dt \tag{2.9}$$

and $\langle A \rangle_{ensemble}$ is given by

$$\langle A \rangle_{ensemble} = \int \int d\mathbf{p}^N d\mathbf{r}^N A(\mathbf{p}, \mathbf{r}) \rho(\mathbf{p}, \mathbf{r}) \tag{2.10}$$

where $\rho(\mathbf{p}, \mathbf{r})$ is the probability distribution of the ensembles. With the *ergodic hypothesis* in mind, the goal of MD simulations is to evolve the system such that the phase space is sampled sufficiently and use time averages to compute the macroscopic observables.

2.1.3 Temperature & Pressure scaling

The equipartition theorem, states that energy is shared equally amongst all energetically accessible (quadratic) degrees of freedom of a system and is a general statement on how all systems evolve in order to maximize their entropy. This implies that in thermal equilibrium all molecules have the same average energy associated with each independent degree of freedom of their motion. For translational motion, the average kinetic energy of each molecule can then be expressed as

$$\langle KE \rangle = \frac{1}{2} m(v_x^2 + v_y^2 + v_z^2) = \frac{3}{2} k_B T \tag{2.11}$$

where k_B is the Boltzmann constant and T is the temperature. Temperature plays an important role in molecular dynamics simulations since it dictates the overall average energy of the molecules in the system. When studying systems in the NVT/NPT ensembles, the temperature and pressure of the system needs to be held constant. A possible way to achieve constant temperature in simulations could be to force it to be exactly T at every time step. In practice, this proves to be quite a severe perturbation and its side effects are quite large in systems with small number of particles. Better methods for thermostating/barostating systems are available and are presented in [9, 17, 58].

In [17], the *Berendsen method* of scaling temperature in a MD simulation is presented. In this method, the system's temperature is scaled directly but its effects are relaxed over a time constant, τ_T. Assuming T_0 is the desired temperature, Δt is the simulation time step, the *Berendsen* thermostat scales all velocities of the particles at each time step by the following factor, λ

$$\lambda = \sqrt{1 + \frac{\Delta t}{\tau_T} \left(\frac{T_0}{T} - 1 \right)} \tag{2.12}$$

According to Berendsen, $\tau_T > 100\Delta t$ typically results in the system having natural fluctuations about the desired temperature. Similarly, the pressure of a system can be scaled to a desired target using the *Berendsen* barostat. Barostating is achieved by changing the positions of all atoms and system volume during the simulation. If the target pressure is P_0 and τ_P is the timescale over which the system's pressure is relaxed, the scaling factor μ is given by [17, 145]

$$\mu = \left[1 - \frac{\beta \Delta t}{\tau_P} (P_0 - P) \right]^{1/3}, \tag{2.13}$$

where β is the system's isothermal compressibility and P is the current pressure in the system. From the scaling factor μ, the positions of all particles and the system size can then be scaled as

$$\mathbf{r}(t+\delta t) = \mu \mathbf{r}(t) \tag{2.14}$$
$$V(t+\delta t) = \mu^3 V(t), \tag{2.15}$$

where $V(t)$ is the time dependent volume of the system.

2.1.4 Interaction Potentials/Force Fields

The key input in MD simulations is defining the means through which the particles/atoms interact with each other. One of the simplest ways to describe interactions in an MD system is through the *Lennard-Jones* potential also known as the $12-6$ potential. In its simplest form, this potential is described by the following equation

$$V(r) = 4\epsilon \left[\left(\frac{\sigma}{r}\right)^{12} - \left(\frac{\sigma}{r}\right)^{6} \right]. \tag{2.16}$$

Here ϵ is the energy well depth, σ is the distance scale i.e $V(\sigma) = 0$ and r is the radial distance between two particles. The $(\sigma/r)^{12}$ term describes the repulsive nature of the potential and is supposed to model the repulsive forces felt by molecules due to overlapping of their electron orbitals. The exponent 12 does not have a true physical motivation other than that it can be calculated efficiently by simply squaring the 6 term. The $(\sigma/r)^6$ term describes the attractive nature of the potential (Van der Waals) and can be derived analytically by considering how two charged spheres induce dipole-dipole interactions onto each other. The *Lennard-Jones* (LJ) potential has been used successfully to model the properties of liquid argon as shown in [184] with the results from the simulation being in excellent agreement with physical observables. In figure 2.1 we show a plot of the potential for $\epsilon = 1$ and $\sigma = 1$. From this we can clearly see the attractive and repulsive regimes introduced by the potential as well as the equilibrium distance where potential is minimum (zero force) In figure 2.1, we mark all distances in dimensionless units as pointed in the following section and scale everything by the potential length scale, σ i.e. $\hat{r} = r/\sigma$.

2.1.4.1 Dimensionless Units

When considering numerical simulations, care must be taken to ensure that no quantity either underflows or overflows the precision available on the machine. Such situations become all too common when studying systems where either the length, time and energy scales involved are too small. In MD simulations, there are two possible ways to circumvent such situations 1) either work in atomic scale units i.e. (picoseconds, nanometers ...) 2) or make all involved length, energy and timescales dimensionless with respect to certain characteristic scales inherently present in the system. In systems being studied under the LJ potential, one such characteristic scale can easily be constructed by using different combinations of the potential's energy ϵ, length scale σ and particle's mass

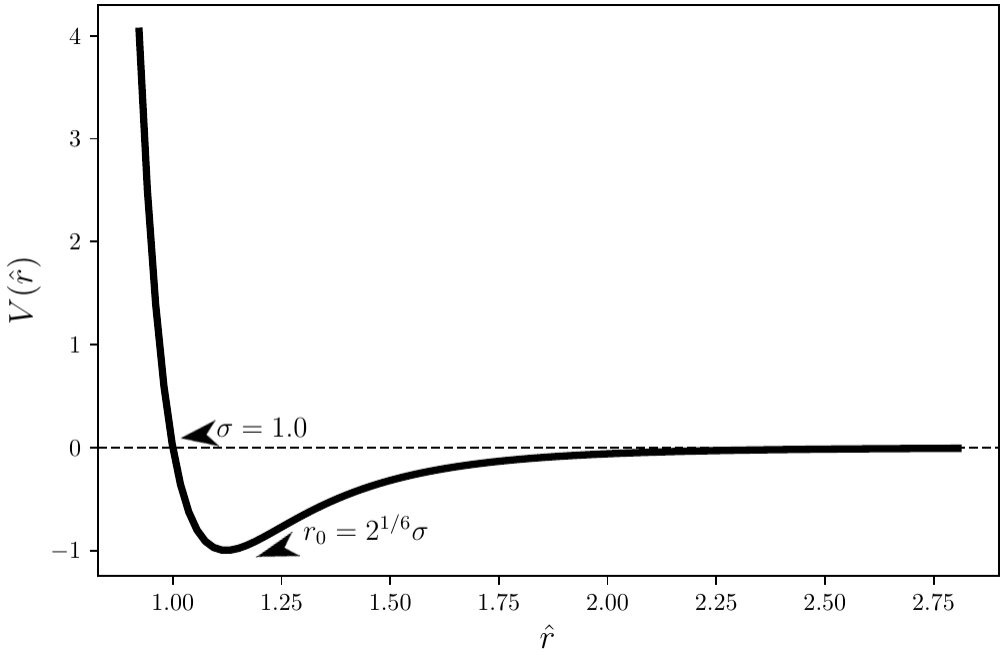

Figure 2.1: 12-6 Lennard Jones potential. Sigma, σ is the Lennard Jones interaction length scale where $V(r) = 0$ and r_0 is the potential minimum i.e. $\partial V/\partial r = 0$

m. Using these values, the dimensionless energy can be described as $E^* = E/\epsilon$, dimensionless distance $r^* = r/\sigma$, temperature $T^* = k_B T/\epsilon$ and time $t^* = t/\left[\sigma(m/\epsilon)^{1/2}\right]$. In dimensionless units, the Lennard-Jones potentials looks even simpler i.e.

$$V^*(r^*) = 4\left[\left(\frac{1}{r^*}\right)^{12} - \left(\frac{1}{r^*}\right)^{6}\right]. \tag{2.17}$$

We can see that none of the initial parameters appear in equation (2.17). Using such dimensionless potentials in MD simulations is extremely useful as all values/results are always easily comparable. Results obtained via dimensionless simulations can then be easily transferred to different system via a straightforward scaling of the obtained simulation quantities using the model parameters i.e. ϵ, σ and m.

2.1.5 Bonded potentials

So far we have discussed the Lennard-Jones potential as it is an excellent candidate to describe non-bonded interactions between atoms and molecules in simulations. However, to describe and model complex bonded interactions present in molecules and between atoms, more complicated interaction potentials need to be considered. When describing covalent bonds in molecules a lot of details need to be considered such as the angles between the bonds, bond rotation and torsion, changes in bond length etc.

In order to describe/capture such effects a large suite of inter-atomic potentials/force fields have been developed and are extensively used in MD simulations. In simplified terms, the total energy of a molecule can be described as a sum of contributions from

different interatomic potentials i.e. [145]

$$E_{total} = E_{bond} + E_{angle} + E_{torsion} + E_{oop} + E_{cross} + E_{nonbond}, \tag{2.18}$$

where

- E_{bond} is the contribution to the total energy due to changes in bond length
- E_{angle} describes the contribution to E_{total} due to the changes in the angle between atoms and is considered a three body potential
- $E_{torison}$ captures the contributions to E_{total} due to the rotational motion of different parts of a molecule relative to each other
- E_{oop} describes the *out of plane* contributions that happen when one part of the molecule is out of plane with respect to the rest
- E_{cross} combines the effects of all cross terms from other interactions
- $E_{nonbond}$ describes the contributions to the total energy from all other sources that are not associated with covalent bonds e.g. Lennard-Jones and Coulomb interactions

2.1.5.1 E_{bond} energy

As described earlier, this reflects the contribution to the total energy of a molecule due to the stretching/compression of bonds between atoms of a molecule. As it describes interactions between two atoms, it is simply a pair potential and in its simplest form can be described by a *harmonic* potential i.e

$$E_{bond} = \sum_{bonds} \frac{1}{2} k_b \left(b - b_0\right)^2, \tag{2.19}$$

where b_0 is the desired equilibrium bond length and b is the current bond length. Expressing (2.19) in terms of the coordinates of the atoms involved in the interaction [145]

$$E_i = \sum_j \frac{1}{2} k \left(r_{ij} - r_0\right)^2. \tag{2.20}$$

From (2.20) it can easily be seen that such a potential is approximating the bond as a spring with a spring constant k. This approximation is quite simple and indeed does work well in most scenarios but has a few drawbacks. For instance, the harmonic bond potential cannot describe large displacements from the equilibrium bond length, b_0 quite well. Secondly, it cannot also describe the situations where the bonds between atoms spontaneous break. To improve approximations for non-elastic regimes one can easily add higher order terms in $b - b_0$ and refine the potential as needed. Adding higher order terms can help in describing larger displacement and strains, but effects of bond breaking are still not covered.

Another effective bond potential that is also widely used is the *Morse Potential* i.e [145]

$$E_{bond} = \sum_{bonds} D_b \left(1 - \exp\left[-a\left(b - b_0\right)\right]\right)^2 \tag{2.21}$$

The *Morse Potential* is used quite often in simulations to describe bond energies since it tends to zero for large displacements from the equilibrium, so in principle it can describe bond breaking. However since the potential is approximated via a decaying exponential, the effect is never fully zero so small long range effects might still be an issue.

Another much used and useful bond potential is the *FENE* (Finite Extensible Non-linear Elastic) bond potential and is used quite often when studying polymer chains and melts. It is described by

$$E_{bond} = -\frac{1}{2} K R_0^2 \log\left[1 - \left(\frac{r}{R_0}\right)^2\right] \tag{2.22}$$

where R_0 describes the maximum extent of the bond. In addition to (3.1), if one also includes the repulsive part of the $12-6$ Lennard Jones, this potential asymptotically approaches the harmonic potential described earlier for small displacements of the bond length near R_0 whereas it diverges as the bond length approaches R_0. The FENE bond potential is quite useful when studying polymer chains as it prevents spurious bond crossing that are not physical to begin with.

2.1.5.2 E_{angle}

This terms captures the contributions to the total potential energy of a molecule due to changes in the angle formed by two different bonds. Most kinds of covalent bonds have some angle that is most favored by them for instance for sp^3 hybridized bonds, 109° is most favored, for $sp^2 120^\circ$ is most favored [145]. Similar to the E_{bond} case, the simplest way to describe the angular potential is again through a harmonic potential i.e

$$E_{angle} = \sum_{\theta} H_\theta \left(\theta - \theta_0\right)^2, \tag{2.23}$$

where θ_0 is the equilibrium angle made by two bonds and H_θ is like a spring constant that maps angular displacements to potential energy. For larger angles again, one can improve the potential by adding higher order terms in $\theta - \theta_0$ [145].

2.1.5.3 Torsional Energy, $E_{torsion}$

To describe energy contributions from rotational motions of different parts of a molecule relative to each other, *torsional* effects need to be considered. Unlike the bond and angular harmonic potentials, describing torsional effects is little involved and typically involves trigonometric functions. A simple example of torsional motion exhibited by a molecule can be provided by considering the rotation of the ethane molecule C_2H_6 around its central bond axis [145].

If one models the angle between the two different parts of a molecule by ϕ, the potential function needs to be periodic in ϕ i.e. $f(\phi) = f(\phi + 2\pi)$ as it is possible to do a full rotation about a central axis and return to the initial position. Due to this periodic requirement, the trigonometric sin and cos functions are useful in this situation. A commonly used expression for the *torsional* potential energy is constructed by taking a few terms from a Fourier series in ϕ [145]

$$E_{torsion} = V_1 \left(1 + \cos\left(\phi\right)\right) + V_2 \left(1 + \cos\left(2\phi\right)\right)) + V_3 \left(1 + \cos\left(3\phi\right)\right) \tag{2.24}$$

where V_1 describes the dipole-dipole interactions between the parts of the molecule involved, V_2 describes the bond configuration and V_3 relates to the steric energy.

2.1.5.4 Out-of-Plane, E_{oop}

As the name illustrates, the *out-of-plane* terms describe the energy stored in a molecule if certain parts of itself are mis-aligned and shifted out of plane with respect to a common plane of axis. The functional form of such a potential is quite simple [145] and can be written as

$$E_{oop} = \sum_{\chi} H_{\chi}\, \chi^2, \tag{2.25}$$

where χ is a measure of the displacement out of the plane.

2.1.5.5 Cross/Nonbonded terms, $E_{cross}, E_{nonbonded}$

The cross terms are simply all the functions that contain several of the above mentioned potentials. For instance, the cross terms can describe how a stretched bond can have a weak angular dependence than a regular bond, or they can also describe the relations between two displacements, an angle as well as including torsional effects [145]. We can quickly see that by mixing such effects, one can model rather complicated motions present within molecules. Careful inclusion of cross terms in describing the total energy of a molecule can significantly improve the accuracy of the simulations, whilst it must also be mentioned that including higher order effects typically result in higher computational costs.

The *non-bonded* terms, $E_{nonbond}$ amalgamates all the effects from non bonded interactions a molecule may have with others. These interactions can possibly include Var der Waals type forces, Coulomb forces for charged molecules as well as effects from hydrogen bonds. Considering these contributions, one can write the $E_{nonbond}$ term simply as a sum of the three i.e. [145]

$$E_{nonbond} = E_{vdW} + E_{Coulomb} + E_{hBond} \tag{2.26}$$

2.1.6 Reactive Potentials

The potential functions considered so far enable one to model physical processes via MD simulations quite accurately. However, if the system to be studies exhibits chemical processes such as the spontaneous formation and breaking of bonds between atoms in a molecule or between molecules themselves the potentials considered so far fail to address

such phenomena. Although the chemical processes concerning the formation and breaking of bonds is inherently quantum mechanical in nature, having a classical description of such processes can yield significant benefits in terms of computational costs incurred during MD simulations.

One such classical analogue for describing the chemical bond formation/breaking processes is the *Tersoff* type potentials as described in [145,170–173]. Unlike the traditional molecular mechanics force fields [33,53,65,66,114,164], the Tersoff model allows for the formation and breaking of chemical bonds during simulations. In doing so, Tersoff potentials consider the many body effects arising from the local interaction environment of each atom and uses that to modify the strength of more conventional pairwise terms. With this approach, individual atoms are not constrained to remain attached to specific neighbors. Models of this sort, despite being classical in nature can provide realistic descriptions to the covalent bonding process which are inherently quantum mechanical in nature. Tersoff potentials have been developed and applied successfully to study systems involving silicon [172], carbon [171], germanium [173], oxygen or hydrogen [22].

The REBO (Reactive Empirical Bond Order) potential is one particularly useful type of Tersoff potential developed by Brenner [23, 24]. The REBO potential uses a Tersoff-style potential to describe covalent bonding interactions in carbon and hydrocarbon systems. This potential has also been used successfully to model different materials such as fullerenes [24] and carbon nanotubes [63].

2.1.7 Numerical Integration

Given the typical number of particles and the nonlinearity of the potentials involved in MD simulations, analytical solutions to the system's equations of motion are not possible. Due to this limitation one has to resort to numerical methods/techniques to solve for the dynamics of the system and study its evolution through time. There are several numerical algorithms proposed in this regard, but the (1) *Verlet algorithm* [184], (2) *Leap-frog algorithm*, and (3) *Velocity-Verlet* are three widely used algorithms in MD. The major benefits to these algorithms is that they are symplectic in nature and conserve energy and momentum of the system for simple potentials. These algorithms are also time reversible respecting the time symmetry present in dynamics. Moreover, these algorithms share the properties that numerical errors made during time marching typically decay over time resulting in long stable simulations.

2.1.7.1 Verlet Method

This algorithm is one of the most commonly used finite difference time marching algorithm and was first used by Verlet in [184]. It can be easily derived by taking a Taylor expansion of the position of a given particle one step Δt forward and backward in time i.e

$$\mathbf{r}\left(t+\delta t\right)=\mathbf{r}(t)+\delta t\mathbf{v}(t)+\frac{1}{2}\delta t^{2}\mathbf{a}(t)+\frac{1}{3!}\delta t^{3}\dot{\mathbf{a}}(t)+\mathcal{O}\left(\delta t^{4}\right) \tag{2.27}$$

$$\mathbf{r}\left(t-\delta t\right)=\mathbf{r}(t)-\delta t\mathbf{v}(t)+\frac{1}{2}\delta t^{2}\mathbf{a}(t)-\frac{1}{3!}\delta t^{3}\dot{\mathbf{a}}(t)+\mathcal{O}\left(\delta t^{4}\right) \tag{2.28}$$

Summing the two equations yields

$$\mathbf{r}(t+\delta t) = 2\mathbf{r}(t) - \mathbf{r}(t-\delta t) + \delta t^2 \mathbf{a}(t) \tag{2.29}$$

Since the update to the positions is calculated using the position at time t as well as at time $t-\delta t$, the *Verlet* algorithm is a two step method. The velocities are calculated by averaging the position updates i.e

$$\mathbf{v}(t) = \frac{\mathbf{r}(t+\delta t) - \mathbf{r}(t-\delta t)}{2\delta t} \tag{2.30}$$

The global error in computing the positions and the velocities of the particles scales as $\mathcal{O}(\delta t^2)$ due to which the *Verlet* algorithm is also known as a second order integrator.

2.1.7.2 Leap-Frog Method

In the *Leap-Frog* [19] method, the velocities of all the particles involved are calculated at half time step i.e $t+\delta t/2$. These velocities are then used to update the positions. In the subsequent step, the positions then leap over velocities and the time marching continues in this manner. An advantage of this approach is that velocities are calculated explicitly but the drawback is that they are not calculated at the same time step as the positions. One can approximate the velocities at time t as follows

$$\mathbf{v}(t) = \frac{1}{2}\left[\mathbf{v}\left(t - \frac{1}{2}\delta t\right) + \mathbf{v}\left(t + \frac{1}{2}\delta t\right)\right] \tag{2.31}$$

The main equations of the *Leap-Frog* algorithm are

$$\mathbf{r}\left(t+\delta t\right) = \mathbf{r}\left(t\right) + \mathbf{v}\left(1 + \frac{1}{2}\delta t\right)\delta t \tag{2.32}$$

$$\mathbf{v}\left(t + \frac{1}{2}\delta t\right) = \mathbf{v}\left(t - \frac{1}{2}\delta t\right) + \mathbf{a}(t)\delta t \tag{2.33}$$

2.1.7.3 Velocity Verlet Method

The *Velocity-Verlet* [166] method is widely used in MD simulations since unlike the *Verlet* method, this algorithm is self-starting i.e one does not need to know the position at time $t-\delta t$ to start integrating. Another advantage of this method is that both the positions, $\mathbf{r}(t)$ and velocities, $\mathbf{v}(t)$ are calculated at the same time step and explicitly without the need of any averaging. The derivation of this method is fairly simple and can be started by considering the Taylor expansion of the positions at time $t+\delta t$ i.e

$$\mathbf{r}\left(t+\delta t\right) = \mathbf{r}(t) + \delta t \mathbf{v}(t) + \frac{1}{2}\delta t^2 \mathbf{a}(t) + \mathcal{O}\left(\delta t^3\right). \tag{2.34}$$

Using Netwon equation of motion, we can replace the acceleration term with the forces, $\mathbf{F}$ acting on the particles at time t and position $\mathbf{r}(t)$. With this substitution, we obtain

$$\mathbf{r}\left(t+\delta t\right) = \mathbf{r}(t) + \delta t \mathbf{v}(t) + \frac{1}{2}\delta t^2 \frac{\mathbf{F}\left(\mathbf{r}(t)\right)}{m} + \mathcal{O}\left(\delta t^3\right). \tag{2.35}$$

Similarly, considering the Taylor expansion of the velocities we obtain

$$\mathbf{v}(t+\delta t) = \mathbf{v}(t) + \delta t \mathbf{a}(t) + \frac{1}{2}\delta t^2 \dot{\mathbf{a}}(t) + \mathcal{O}\left(\delta t^3\right). \tag{2.36}$$

In (2.36), we can again replace the acceleration by the forces acting on the particles at time t at position $\mathbf{r}(t)$, but we still need an expression for $\dot{\mathbf{a}}$. To this end, one can consider the Taylor expansion of $\mathbf{a}(t+\delta t)$,

$$\mathbf{a}\left(t+\delta t\right) = \mathbf{a}(t) + \delta t \dot{\mathbf{a}}(t) + \mathcal{O}(\delta t^2) \tag{2.37}$$

Multiplying by $\frac{\delta t^2}{2}$ and rearranging the terms in (2.37), we obtain

$$\frac{\delta t^2}{2}\dot{\mathbf{a}}(t) = \frac{\delta t}{2}\left(\mathbf{a}(t+\delta t) - \mathbf{a}(t)\right) + \mathcal{O}(\delta t^3). \tag{2.38}$$

Now with this approximation for $\dot{\mathbf{a}}(t)$, and using the equations of motion we can rewrite equation (2.36) as

$$\mathbf{v}(t+\delta t) = \mathbf{v}(t) + \frac{\delta t}{2m}\left(\mathbf{F}(\mathbf{r}(t+\delta t)) + \mathbf{F}(\mathbf{r}(t))\right) + \mathcal{O}(\delta t^3). \tag{2.39}$$

With these simplifications, the *Velocity-Verlet* equations are

$$\mathbf{r}\left(t+\delta t\right) = \mathbf{r}(t) + \delta t \mathbf{v}(t) + \frac{1}{2}\delta t^2 \mathbf{a}(t) + \mathcal{O}\left(\delta t^3\right) \tag{2.40}$$

$$\mathbf{v}(t+\delta t) = \mathbf{v}(t) + \frac{\delta t}{2m}\left(\mathbf{F}(\mathbf{r}(t+\delta t)) + \mathbf{F}(\mathbf{r}(t))\right) + \mathcal{O}\left(\delta t^3\right) \tag{2.41}$$

In practice the evaluation of these equations happens as follows

1. Initialize all the forces on the particles to zero

2. Compute the forces, $\mathbf{F}$ at time t using the current positions of all particles, $\mathbf{r}(t)$

3. Perform a partial update of the velocities and a full update of the particles positions as follows

$$\boldsymbol{v}^* = \boldsymbol{v}(t) + \frac{\delta t}{2m}\boldsymbol{F}(t) \tag{2.42}$$

$$\boldsymbol{r}(t+\delta t) = \boldsymbol{r}(t) + \boldsymbol{v}^*(t)\delta t \tag{2.43}$$

4. Compute the forces, $\mathbf{F}$ again using the updates positions i.e. $\mathbf{r}(t+\delta t)$

5. Update the velocities using the computed forces $\mathbf{F}(\mathbf{r}(t+\delta t))$ via

$$\boldsymbol{v}(t+\delta t) = \boldsymbol{v}^*(t) + \frac{\delta t}{2m}\boldsymbol{F}(\boldsymbol{r}(t+\delta t)) \tag{2.44}$$

2.1.8 Periodic Boundary Conditions

Rudimentary MD algorithms typically scale as N^2 where N is the number of particles involved in the simulation. This is primarily due to the fact that computing pairwise interactions to determine the net forces acting on the particle is quite computationally expensive. With tricks such as neighbour lists, Verlet lists and interaction cutoffs one can get the algorithms to scale as $O(N)$ but still the computational costs incurred can be high. To deal with such complexities, one typically employs *periodic boundary conditions* in their simulations which allow one to approximate a very large/infinite system by using a small part commonly referred to as the *unit cell*. Particles that leave the unit cell immediately enter it back from the opposite side with the same velocity and momentum. The other copies of the unit cell are commonly referred to as *images* and during the simulation only the properties of the original unit cell/simulation box need to be recorded and carried forward in time.

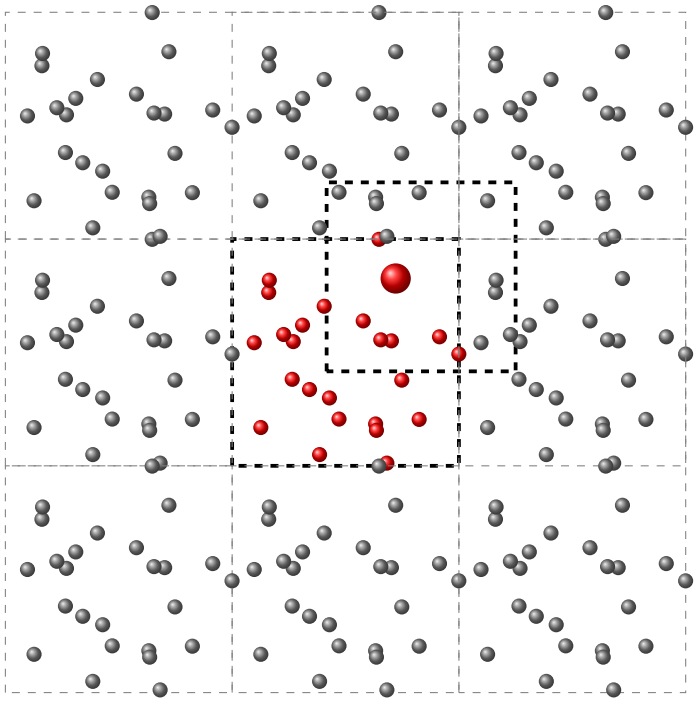

Figure 2.2: Illustration of periodic boundary conditions for a 2D system of particles. The center cell with red particle is the *unit cell* and the neighbouring cells are periodic images of the same. The offset cell marks the *minimum images* of the enlarged particle within the unit cell.

2.1.8.1 Minimum image convention

Having briefly explained the usefulness of the periodic boundary conditions and how it simplifies simulating large systems by simply considering a small unit cell from it, it is necessary to discuss how pairwise interactions between particles are computed. Having mentioned that if a particle passes through a periodic boundary it or its periodic image should enter the *unit cell* via the opposite end. This way the number of particles within the unit cell is always conserved as particles leaving the cell are automatically replaced by their nearest images. Keeping this in mind, commonly in molecular dynamics simulations the pairwise interactions between particles are computed using their *nearest images*, and is commonly referred to as the *minimum image convention*. As per this convention, say in order to compute the potential energy for force between two particles i and j, if the distance between the two is larger than $L/2$, with L being the unit cell length, then particle j will be disregarded as the interaction partner of i and its image located at $x_j - L$ will be used instead.

2.2 Lattice-Boltzmann Methods

Lattice-Boltzmann methods are a systematic framework built upon the famous Boltzmann equation describing the mesoscopic dynamics of particles within a fluid. The Lattice-Boltzmann equation (LBE) is a discretized version of the Boltzmann equation and is used heavily to simulate the dynamics of fluid flows without ever having to solve the all encompassing Navier-Stokes equations. Via solving for the mesoscopic *particle* populations/distribution function, the macroscopic fluid observables emerge as various moments of the distribution functions. Originally being derived from lattice cellular automata [195, 196], the LB framework has rapidly evolved into a rigorous and well studied method for simulating fluid behaviour. Due to its computational simplicity and high parallel approach, the LB framework has proven to be a vital method in simulating large fluid flow problems and its implementations have known to scale extremely well with problem sizes. A distinctive feature of the LB framework as a computational solver for fluid problems is its space-time locality, and the fact that all particle information travel in straight lines predefined within the model. This makes it relatively easy to parallelize and easy to scale. Due to these properties, the LB approach counts today for an impressive array of applications across several fields of fluid dynamics and has proven vital in the development of many technologies.

In this section, we detail out the framework starting from the very basics of fluid dynamics and the governing Navier-Stokes equations and work our way up to the fully discrete LB equation. In section (2.2.1), we begin by outlining the Navier-Stokes equations and present short derivations of the mass and momentum conservation equations. Following that, since the Boltzmann equation is deeply rooted in the kinetic theory of particles, in section (2.2.2) we elaborate on the quantities involved in the Boltzmann equation and how macroscopic observables are tied to the particle population distribution functions. In section (2.2.3) we present the LB equation from a broader perspective in order to set the stage for details presented in the subsequent sections. We also mention the role of collision operators in the LB framework and explain the widely popular BGK (Bhatnagar-Gross-Krook) collision operator. In the subsequent section (2.2.4) we explain in detail how the velocity space is discretized in the LB framework in order to reduce its dimensionality to a finite number. We show how in practice the Boltzmann equation is made dimensionless and from this how discrete velocities are derived via expressing the particle and equilibrium particle distributions as finite series over Hermite polynomials. In the following section, (2.2.5), the address the issue of boundary conditions within the LB framework and work through how different types of boundary conditions under different geometries can be implemented for the LB equation. In section (2.2.6) we cover the methodology through which external forces can be included in the LB equation and how the external forcing terms are discretized over a Hermite basis.

In the final sections i.e (2.2.7 - 2.2.10), we address how thermal fluctuations can be added into the LB equation via adding spontaneous fluctuations to the stress tensor in such a way so that the *fluctuation-dissipation* theorem is satisfied. We also describe the immersed boundary method that is used quite often in fluid simulations when external particles/bodies are to be immersed within the fluid. In these sections we also describe how in our framework we couple the fluid and external particles together so that on

the fluid-particle interface, the *no-slip* boundary condition is upheld and discuss how the coupling constant can be properly calibrated to ensure the same. In these sections we also highlight the importance of proper calibration if one wishes the fluid to act as a thermal heat bath for all the particles immersed within. Throughout this section we adopt the approach followed by Kruger et al. in ([79]) and cite the work suitably throughout.

2.2.1 Navier Stokes Equations

2.2.1.1 Conservation of Mass

Conventionally, the study of fluid dynamics is concerned with macroscopic phenomena where the molecular nature of fluids is not considered. The fluid under consideration is treated as a continuous media that evolves over time in a particular region. Under such a treatment, macroscopic quantities such as mass and momentum are to be conserved. To understand the conservation of these quantities and to derive the *Navier-Stokes* equations, we consider a small fluid element i.e. fluid enclosed within a region of volume V_0. The mass of this fluid element can be represented by

$$m = \int_{V_0} \rho \, dV \tag{2.45}$$

To introduce dynamics into the picture, we can consider the rate of change of the fluid element's mass over time. Given that the fluid can neither be created or destroyed, the only way through which the mass of the fluid element can change is if new fluid enters or exits the region V_0. This relationship can be expressed as

$$\frac{\partial}{\partial t} \int_{V_0} \rho dV = - \oint_{\partial V_0} \rho \mathbf{u} \cdot d\mathbf{A} \tag{2.46}$$

where the right hand side represents a surface integral over the boundary enclosing region V_0 and $\mathbf{u}$ is the fluid velocity. Using the *divergence theorem*, equation (2.46) can be rewritten as a volume integral

$$\frac{\partial}{\partial t} \int_{V_0} \rho dV = - \int_{V_0} \nabla \cdot (\rho \mathbf{u}) \, dV \tag{2.47}$$

where $\nabla \cdot (\rho \mathbf{u})$ is the divergence of the momentum density of the fluid i.e. $\rho \mathbf{u}$. As (2.47) is true for arbitrary V_0, the integrand must be zero and we get the *continuity equation* that implies fluid mass conservation

$$\frac{\partial \rho}{\partial t} + \nabla \cdot (\rho \mathbf{u}) = 0 \tag{2.48}$$

Frequently in fluid dynamics literature, equation (2.48) is also expressed as the *material derivative* by expanding the divergence of the momentum density

$$\frac{\partial \rho}{\partial t} + \mathbf{u} \cdot \nabla \rho + \rho \nabla \cdot \mathbf{u} = 0 \tag{2.49}$$

$$\frac{D \rho}{D t} + \rho \nabla \cdot \mathbf{u} = 0 \tag{2.50}$$

where the material derivative is introduced to be

$$\frac{D}{Dt} = \frac{\partial}{\partial t} + \mathbf{u} \cdot \nabla \tag{2.51}$$

which denotes the rate of change as the fluid element moves around in space as compared to it being a stationary point in space [15, 79]

2.2.1.2 Conservation of Momentum

The *continuity equation* (2.48) marks the relationship between fluid density and the momentum density flux, $\rho\mathbf{u}$. Similar to the analysis carried above, we can derive the equation describing the conservation of momentum of the fluid element with density ρ and velocity $\mathbf{u}$ within the region V_0 [15, 79]. Under ideal conditions for a simple fluid (i.e. no internal viscous stresses) the net change in the fluid element's momentum can be attributed to (i) momentum flow into or out of the region V_0 (ii) pressure gradient across the region V_0 and (iii) external body forces F acting on the the fluid element in region V_0. These relationships can be summarized as

$$\frac{d}{dt}\int_{V_0} \rho\mathbf{u} dV = -\oint_{\partial V_0} \rho\mathbf{u}\mathbf{u} \cdot d\mathbf{A} - \oint_{\partial V_0} p d\mathbf{A} + \int_{V_0} \mathbf{F} dV \tag{2.52}$$

where $\mathbf{uu}$ is the fluid velocity outer product with element $u_\alpha u_\beta$ [79] and the surface integrals are over the boundary enclosing region V_0. By converting the surface integrals to volume integral using the divergence theorem we get [79]

$$\int_{V_0} \frac{\partial(\rho\mathbf{u})}{\partial t} dV = -\int_{V_0} \nabla \cdot (\rho\mathbf{u}\mathbf{u})\, dV - \int_{V_0} \nabla p dV + \int_{V_0} \mathbf{F} dV \tag{2.53}$$

Again, this is true for arbitrary V_0 so the integrand must be zero and equation (2.53) yields the famous *Euler equation*

$$\frac{\partial(\rho\mathbf{u})}{\partial t} + \nabla \cdot (\rho\mathbf{u}\mathbf{u}) = -\nabla p + \mathbf{F}. \tag{2.54}$$

Grouping all the velocity and pressure terms on the left hand side, we can express the *Euler equation* using the **momentum flux density tensor** for an ideal fluid i.e.

$$\Pi_{\alpha\beta} = \rho u_\alpha u_\beta - \sigma_{\alpha\beta} \tag{2.55}$$

and we obtain the *Cauchy momentum equation* [79]

$$\frac{\partial(\rho\mathbf{u})}{\partial t} + \nabla \cdot \Pi = \mathbf{F}. \tag{2.56}$$

The momentum flux density tensor $\mathbf{\Pi}$ describes the momentum flux between cross velocity terms as well as the stresses involved during momentum transfer within the moving fluid. The term $\sigma_{\alpha\beta}$ is the *stress tensor* and for simple ideal fluids is simply $\sigma_{\alpha\beta} = -p\delta_{\alpha\beta}$ and is entirely diagonal and isotropic in all directions.

The Cauchy momentum equation as described in (2.56) provides a good description of the momentum conservation for ideal fluids only. For real fluids, the equation needs to be modified to include the viscous effects present in fluids due to relative motion between different parts of the fluid element itself. Due to such internal friction, the momentum transfer from one fluid element to another is not reversible and dissipates over space and time [15, 79]. To formulate a closed form for such a viscous stress tensor, σ, it can be argued that it must vanish in the case of simple fluids in uniform motion. Furthermore it can also be noted that if the relative velocities between the different fluid elements is small, i.e. small velocity gradients, then the momentum transfer and dissipation due to viscous effects can entirely be represented via the first derivatives of the velocities [82]. A generic rank two tensor satisfying these requirements can be written as follows [79, 82]

$$\sigma_{\alpha\beta} = \eta \left(\frac{\partial u_\alpha}{\partial x_\beta} + \frac{\partial u_\beta}{\partial x_\alpha} \right) + \zeta \delta_{\alpha\beta} \frac{\partial u_\gamma}{\partial x_\gamma}, \tag{2.57}$$

where η and ζ are coefficients of viscosity. These coefficients are usually assumed to be isotropic and uniform. The viscous stress tensor is typically broken down into a *traceless* shear stress component and a *normal* stress component as follows [79]

$$\sigma_{\alpha\beta} = \eta \left(\frac{\partial u_\alpha}{\partial x_\beta} + \frac{\partial u_\beta}{\partial x_\alpha} - \frac{2}{3} \delta_{\alpha\beta} \frac{\partial u_\gamma}{\partial x_\gamma} \right) + \eta_B \delta_{\alpha\beta} \frac{\partial u_\gamma}{\partial x_\gamma} \tag{2.58}$$

where η is known as the *shear viscosity* of the fluid and $\eta_B = 2\eta/3 + \zeta$ is termed as the *bulk viscosity* of the fluid.

Now, with having arrived at a closed form for the viscous stress tensor that describes the dissipative and viscous effects during momentum transfer between fluid elements, the full *Navier-Stokes* equations can be listed as follows [79, 82]

$$\frac{\partial (\rho u_\alpha)}{\partial t} + \frac{\partial (\rho u_\alpha u_\beta)}{\partial x_\beta} = -\frac{\partial p}{\partial x_\alpha} + \frac{\partial}{\partial x_\beta} \left[\eta \left(\frac{\partial u_\alpha}{\partial x_\beta} + \frac{\partial u_\beta}{\partial u_\alpha} \right) + \left(\eta_B - \frac{2\eta}{3} \right) \frac{\partial u_\gamma}{\partial x_\gamma} \delta_{\alpha\beta} \right] + F_\alpha \tag{2.59}$$

The *Navier-Stokes* equation can be simplified considerably if we assume that the fluid flow is incompressible i.e. $\rho = const.$ If the density of the fluid is assumed to be constant, then via the continuity equation (2.48) we obtain $\nabla \cdot \mathbf{u} = 0$. In this case, the *incompressible Navier-Stokes* equations are written as follows

$$\rho \frac{D\mathbf{u}}{Dt} = -\nabla p + \eta (\nabla \cdot \nabla) \mathbf{u} + \mathbf{F}. \tag{2.60}$$

2.2.1.3 Equation of State

Based on the discussions so far, we have in total four equations describing the dynamics of a fluid namely, the continuity equation (2.48) and the momentum conservation equations (one for each component of the fluid velocity) (2.59). However, it can be noted that this system is incomplete since we have five unknowns namely, the fluid density, ρ, pressure, p and the three velocity components i.e. u_x, u_y, u_z and we have only four equations describing their evolution. As a result, the system of equations is unsolvable since we

have more unknowns than equations at hand. One way to circumvent this issue would be by assuming the fluid density is constant throughout, i.e. $\rho = C$. This fixes the fluid density for the system effectively rendering the system to have four equations with four unknowns. This approach is quite useful in our case, since in our work we simulate systems with density fairly constant throughout, thus the fluid pressure can be linearly related to its density. Any additional constants do not impact the dynamics per say since, the pressure gradient is the quantity of interest in the Navier-Stokes equations (NSE).

In other cases, more general approaches can be used by adding another equation that is derived from the *state principle* of equilibrium thermodynamics. This equation of state is simply a relationship between the system's thermodynamic state variable i.e. the fluid density, ρ, pressure p, temperature, T, internal energy e and entropy s. The **ideal gas law** is an example of such an equation of state and simply relates the pressure to density and temperature through the specific gas constant, R

$$p = \rho RT. \tag{2.61}$$

2.2.2 Kinetic Theory & The Boltzmann Equation

Unlike the description of fluids provided in section (2.2.1), where all fluids are treated as a continuous media, the *kinetic theory* description of the same lies somewhere in between the *microscopic* description of the motions of the atoms and molecules comprising the fluid, and the macroscopic observables such as pressure, density, fluid momentum and velocity and temperature. This *mesoscopic* approach deals with the *distribution* of particles in fluids (gas, liquids) and derives all the macroscopic observables from such a quantity. The distribution of particles is assumed to evolve on timescales that is, on average, equal to the mean collision time of the fluid particles [79].

The fundamental quantity in kinetic theory of fluids is the *particle distribution function*, $f(\mathbf{x}, \xi, t)$, which represents the density of particles with velocity $\xi = (\xi_x, \xi_y, \xi_z)$ at position $\mathbf{x}$ at time t. Although the particle distribution function at first glance seems to describe quantities relevant to the microscopic scales, the macroscopic observables such as fluid density, $\rho(\mathbf{x}, t)$ and velocity $\mathbf{u}(\mathbf{x}, t)$ can be easily obtained through the moments of f. These moments are simply weights integrals of f over the entire velocity space. For instance, density of the fluid can be easily recovered from the first moment of the distribution function

$$\rho(\mathbf{x}, t) = \int f(\mathbf{x}, \xi, t) d^3\xi. \tag{2.62}$$

By integrating velocity out, we are able to recover the contribution to the density of fluid by particles of all velocities at position $\mathbf{x}$ at time t.

Similarly, taking the first moment of the distribution over the entire velocity space, i.e. ξf we recover the fluid's momentum density at all positions $\mathbf{x}$ at time t,

$$\rho(\mathbf{x}, t)\mathbf{u}(\mathbf{x}, t) = \int \xi f(\mathbf{x}, \xi, t) d^3\xi. \tag{2.63}$$

2.2.2.1 Equilibrium Distribution Function

Given that we are considering fluid/gas where the particles are free to collide, it can be reasonably expected that over sufficiently long periods of time such a system will tend towards an equilibrium distribution function provided no external time dependent forces/factors are at play. Under this assumption, we can assume that the particle distribution function $f(\mathbf{x}, \xi, t)$ will tend towards f^{eq} which is isotropic in velocity space around $\xi = \mathbf{u}$ in a reference frame that is moving with speed $\mathbf{u}$ [79].

Assuming collisions between the particles in our fluid are fully elastic, we can impose further restrictions on the distribution function by requiring it to be separable over velocity space

$$f^{eq}(|\mathbf{v}|^2) = f^{eq}(\xi_x^2 + \xi_y^2 + \xi_z^2) = f^{eq}(\xi_x^2) f^{eq}(\xi_y^2) f^{eq}(\xi_z^2). \tag{2.64}$$

We note that in 2.64, the equilibrium distribution appearing on the left hand side is the full 3-D distribution whereas the f^{eq} appearing on the right hand side are the 1-D equivalents of the same. Holding the velocity magnitude constant i.e. $|\boldsymbol{\xi}|^2 = C$, we can write 2.64 as

$$f^{eq}(|\boldsymbol{\xi}|^2) = \log f^{eq}(\xi_x^2) + \log f^{eq}(\xi_y^2) + \log f^{eq}(\xi_z^2) = C \tag{2.65}$$

Such a relationship is only fulfilled when each of the 1-D equilibrium distribution functions are of the form [79]

$$\log f^{eq}(v_i^2) = a + b\xi_i^2, \tag{2.66}$$

where $i = x, y, z$. With this simplification, we obtain

$$\log f^{eq}(\xi_x^2) + \log f^{eq}(\xi_y^2) + \log f^{eq}(\xi_z^2) = 3a + b(\xi_x^2 + \xi_y^2 + \xi_z^2). \tag{2.67}$$

From (2.67), one can easily derive the equilibrium distribution function to be

$$f^{eq}(|\boldsymbol{\xi}|) = e^{3a} e^{b|\boldsymbol{\xi}|^2}. \tag{2.68}$$

The constants a and b can be fixed by demanding that collisions conserve energy and momentum as well as f^{eq} have the same energy and density moments as f. With this condition, the equilibrium particle distribution function is found to be

$$f^{eq}(\mathbf{x}, |\boldsymbol{\xi}|, t) = \rho \left(\frac{1}{2\pi RT} \right)^{3/2} \exp\left(-\frac{|\boldsymbol{\xi}|^2}{2RT} \right). \tag{2.69}$$

This form of the equilibrium distribution function is commonly referred to as the *Maxwell-Boltzmann* distribution function. Although this derivation was a little simplistic in nature, a more rigorous derivation of the same can be found in [50] where the author also goes to show that this expression is also unique and how to derive it as a solution for equation (2.71) in the limiting case.

2.2.2.2 Boltzmann Equation

So far we have described f as the particle distribution function and whose moments over velocity space yield the macroscopic observables such as fluid density, ρ, momentum density $\rho\mathbf{u}$ etc. The *Boltzmann equation* now simply describes the time evolution of the particle distribution function under the influence of external forces and inter-particle collisions. Considering the total derivative of $f(\mathbf{x}, \xi, t)$

$$\frac{df}{dt} = \left(\frac{\partial f}{\partial t}\right) + \left(\frac{\partial f}{\partial x_\alpha}\right)\frac{dx_\alpha}{dt} + \left(\frac{\partial f}{\partial \xi_\alpha}\right)\frac{d\xi_\alpha}{dt} \tag{2.70}$$

From equation (2.70), we can see that various terms arise in the processes of taking the total derivative of f. It can be noted that dx_α/dt is simply the local particle velocity, ξ_α whereas $d\xi_\alpha/dt$ describes an acceleration term. Using Newton's second law of motion, we can rewrite this term as F_α/ρ that has units of force per unit mass. With these substitutions we get the final expression for the the Boltzmann equation

$$\frac{\partial f}{\partial t} + \xi_\alpha\frac{\partial f}{\partial x_\alpha} + \frac{F_\alpha}{\rho}\frac{\partial f}{\partial \xi_\alpha} = \Omega(f), \tag{2.71}$$

where $\alpha = x, y, z$ and $\Omega(f)$ acts as a source term for the equation and represents changes to f due to local collisions between particles. The term $\Omega(f)$ is also commonly known as the *collision* operator [79, 161]

In Boltzmann's original work, the collision operator is in the form of a complicated double integral over velocity space as it considers all the possible outcomes of two particle collisions. However, in practice the collision operators used are quite simple in nature and the most commonly used operator is the **BGK collision operator** [18]

$$\Omega(f) = -\frac{1}{\tau}\left(f - f^{eq}\right) \tag{2.72}$$

This collision operator describes how the collisions deviate the distribution function f away from is local equilibrium value f^{eq} and how it relaxes back towards f^{eq} over a time period τ also known as the **relaxation time**. The value of τ directly determines the fluid transport coefficients such as viscosity and heat diffusivity [79, 161]

2.2.3 The Lattice Boltzmann Equation

The *Lattice Boltzmann Equation*, LBE for short, is basically the Boltzmann equation 2.71 fully discretized on a lattice with cell spacing Δx, temporal resolution Δt as well as over a discrete set of velocities $\mathbf{c}_i$. The fully discretized version of the particle distribution, $f_i(\mathbf{x}, t)$, one for each discrete velocity $\mathbf{c}_i$ is commonly referred to as *populations*. In the LBM framework, the particle populations are the central quantity to be solved since through it the macroscopic quantities such as fluid density, $\rho(\mathbf{x}, t)$ and velocity, $\mathbf{u}(\mathbf{x}, t)$ are derived. However, since everything is discretized, the moments of the particle distribution functions get simply replaced by discrete sums of the the populations i.e. [79, 161]

$$\rho(\mathbf{x}, t) = \sum_i f_i(\mathbf{x}, t) \qquad \rho\mathbf{u}(\mathbf{x}, t) = \sum_i \mathbf{c}_i f_i(\mathbf{x}, t). \tag{2.73}$$

The weights associated with the discrete velocities appear when computing the discrete equilibrium particle distribution function and the discrete moments are simply computed as the vector dot product between the discrete particle populations and velocities c_i. The rationale behind discretizing the velocity space is explained in the subsequent sections, but for understanding the mechanics behind the LB framework it suffices to know that the particle velocities entering in the Boltzmann equation ξ are discretized into specific sets of velocities along with their characteristic weights, ω_i. Depending on the number of discrete velocities chosen in a given LBE implementation it is conventional to reference that approach with a tag DdQq (velocity sets) where d is the number of spatial dimensions and q is the number of discrete velocities chosen for the particular problem. Some popular choices for the velocity sets are D1Q3, D2Q9, D3Q15, D3Q19 and D3Q27 and are frequently used to solve the Navier-Stokes equations using the LBM framework. In table 2.1 the discrete D3Q15 velocity set is presented for illustration purposes. In figures

i	0	1	2	3	4	5	6	7	8	9	10	11	12	13	14
ω_i	$\frac{2}{9}$	$\frac{1}{9}$	$\frac{1}{9}$	$\frac{1}{9}$	$\frac{1}{9}$	$\frac{1}{9}$	$\frac{1}{9}$	$\frac{1}{72}$	$\frac{1}{72}$	$\frac{1}{72}$	$\frac{1}{72}$	$\frac{1}{72}$	$\frac{1}{72}$	$\frac{1}{72}$	$\frac{1}{72}$
c_x	0	1	-1	0	0	0	0	1	-1	1	-1	1	-1	-1	1
c_y	0	0	0	1	-1	0	0	1	-1	1	-1	-1	1	1	-1
c_z	0	0	0	0	0	1	-1	1	-1	-1	1	1	-1	1	-1

Table 2.1: D3Q15 discrete velocity set, where ω_i are the lattice weights and $c_{i=x,y,z}$ are the corresponding lattice velocities

2.3 and 2.4 the discrete velocities emanating from a single lattice site are illustrated for the D2Q9 and D3Q15 cases. It should be noted that D3Q15 and D3Q19 are by far the most commonly used velocity sets in practice when simulating fluid flow according to Navier-Stokes equations. Adopting higher velocity set approaches results in a trade off between simulation accuracy, stability and computational costs. For most laminar flow situations, the D3Q15 and D3Q19 models are adequate in recovering hydrodynamics described by NSE but for turbulent flow it has been shown in [154] that under these two velocity sets certain truncation terms, non-linear momentum advection corrections are not rotationally invariant. Thus for simulating highly turbulent flows (a.k.a high Reynolds number) the D3Q27 velocity set is the better choice [162, 193]

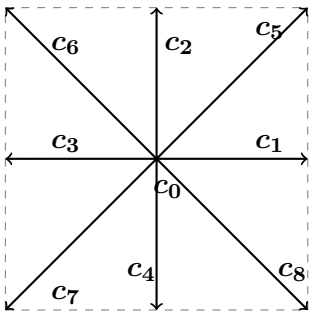

Figure 2.3: LB velocity set D2Q9 for a simple unit lattice cell

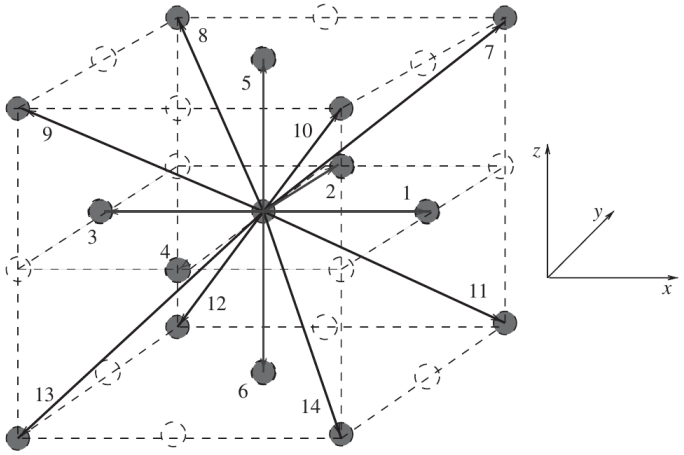

Figure 2.4: LBM D3Q15 velocity set used when simulating Navier-Stokes equations in 3 dimensions. The empty circles are lattice velocities omitted under this constructions based on symmetry arguments. Reprinted from [8]. Copyright 2022 by Philosophical Transactions of the Royal Society of London. Series A: Mathematical, Physical and Engineering Sciences

Above we pointed out that the LBM framework discretizes the Boltzmann equation on a lattice with grid spacing Δx and temporal spacing of Δt. These space and time steps, depending on the problem at hand can be specified in any units (SI, Imperial etc). Typically though, to lower numerical and round off errors, it is conventional to scale the units such that $\Delta x = 1$ and $\Delta t = 1$. In these *lattice* units the LBM equations are made dimensionless as all units are scaled out by the relevant length, velocity and time scales. This approach has the added flexibility that the actual units can be recovered by simply scaling the dimensionless quantities back by their appropriate factors. Moreover, for each velocity set and a choice of grid and temporal spacing, one can derive the *speed of sound*, c_s in the lattice to be

$$c_s^2 = \frac{1}{3}\frac{\Delta x^2}{\Delta t^2} \tag{2.74}$$

With the above mentioned discretizations, the Boltzmann equation can then be formulated on the lattice as follows

$$f_i\left(\mathbf{x} + \mathbf{c}_i\Delta t, t + \Delta t\right) = f_i\left(\mathbf{x}, t\right) + \Omega_i\left(\mathbf{x}, t\right) \tag{2.75}$$

where $f_i\left(\mathbf{x}, t\right)$ is the population of particles at the $\mathbf{x}$ lattice site at time t with velocity $\mathbf{c}_i$ and $\Omega_i\left(\mathbf{x}, t\right)$ is the discretized Boltzmann collision operator. Equation (2.75) describes how, post a collision step, particle populations $f_i\left(\mathbf{x}, t\right)$ *stream* to neighboring lattice sites with velocity $\mathbf{c}_i$ at $\mathbf{x} + \mathbf{c}_i\Delta t$ at time $t + \Delta t$.

As mentioned in the earlier section, the BGK approximation to the original Boltzmann collision operator is most widely used in practice. On the discrete lattice, the operator simplifies to

$$\Omega_i(f) = -\frac{\Delta t}{\tau}\left(f_i - f_i^{eq}\right) \tag{2.76}$$

which relaxes the particle populations f_i at lattice site $\mathbf{x}$ and time t towards the equilibrium value f_i^{eq} at the same location over the time period τ. The equilibrium populations over this discrete domain simplifies to

$$f_i^{eq}(\mathbf{x},t) = \omega_i \rho \left(1 + \frac{\mathbf{u}\cdot\mathbf{c}_i}{c_s^2} + \frac{(\mathbf{u}\cdot\mathbf{c}_i)^2}{2c_s^4} - \frac{\mathbf{u}\cdot\mathbf{u}}{2c_s^2}\right) \tag{2.77}$$

where ω_i and $\mathbf{c}_i$ are the weights and the discrete velocities from the chosen velocity set. It can noted that the equilibrium populations at a particular lattice site is determined entirely from local quantities i.e. f_i and fluid velocity $\mathbf{u}$ at the same site. This greatly reduces the computational cost and typically results in performance gains during simulations.

Lastly, it is important to note that the link between the LBE framework and the continuum Navier-Stokes description of hydrodynamics can be obtained via the *Chapman-Enskog* expansion [28]. Through this expansion, the authors were able to show that the LBE framework results in the correct macroscopic behavior in accordance with the Navier-Stokes equations, with a kinematic shear and bulk viscosity given by

$$\nu = c_s^2\left(\tau - \frac{\Delta t}{2}\right) \tag{2.78}$$

$$\nu_B = \frac{2}{3}\nu. \tag{2.79}$$

The viscous stress tensor, $\sigma_{\alpha\beta}$ can additionally be determined by the particle populations by

$$\sigma_{\alpha\beta} = -\left(1 - \frac{\Delta t}{2\tau}\right)\sum_i c_{i\alpha}c_{i\beta}\left(f_i - f_i^{eq}\right). \tag{2.80}$$

2.2.3.1 Implementation

From the previous section, it should somewhat be apparent that the LBE equation with the discretized BGK collision operator (commonly referred to as the LBGK equation) is fairly straightforward to understand and implement in a numerical simulation. Substituting (2.76) into (2.75) we obtain

$$f_i(\mathbf{x} + \mathbf{c}_i\Delta t, t + \Delta t) = f_i(\mathbf{x},t) - \frac{\Delta t}{\tau}\left(f_i(\mathbf{x},t) - f_i^{eq}(\mathbf{x},t)\right) \tag{2.81}$$

While at first glance this appears to be a first order (in Δt) scheme, in fact it can be shown to be equivalent to an implicit trapezoidal scheme that is second order in Δt [35]. To simplify computation and implementation, we can decompose (2.81) into two essential parts (i) the *collision* step (ii) followed by a *streaming* step. The collision step can be realized by looking at the right hand side of 2.81 i.e.

$$f_i^c(\mathbf{x},t) = f_i(\mathbf{x},t) - \frac{\Delta t}{\tau}\left(f_i(\mathbf{x},t) - f_i^{eq}(\mathbf{x},t)\right) \tag{2.82}$$

where we denote the populations of particles with velocity c_i at the lattice site $\mathbf{x}$ at time t after collisions by f_i^c. These populations are then *streamed* to the neighbouring lattice sites by simply updating their populations by

$$f_i\left(\mathbf{x}+\mathbf{c}_i\Delta t, t+\Delta t\right) = f_i^c\left(\mathbf{x}, t\right) \tag{2.83}$$

These steps are conveniently illustrated in figure (2.5)

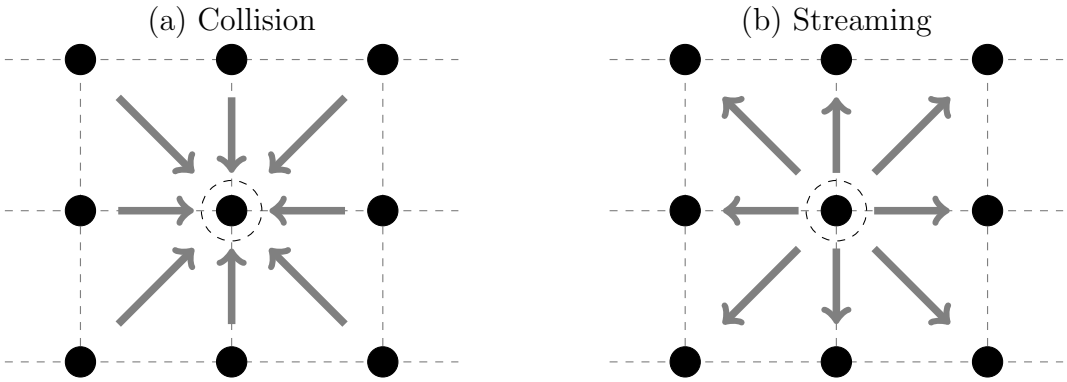

Figure 2.5: (a) Collision step where the the particle populations at the central node (black) is updated based on the collisions with the populations from the neighboring lattice sites (grey) (b) Streaming step, where the updated populations at the central lattice site (black) are streamed outwards to the neighboring sites

With these simplifications in mind, to numerically solve the LBGK equation is quite straightforward and can be broken down into the following steps after initializing the lattice with initial values for the particle populations

1. Compute the macroscopic quantities $\rho(\mathbf{x}, t), \mathbf{u}(\mathbf{x}, t)$ at each lattice site from $f_i\left(\mathbf{x}, t\right)$ via (2.73)

2. Compute the equilibrium particle populations at each site from f_i^{eq} via (2.77)

3. (Optional) Compute the viscous stress tensor, $\sigma_{\alpha\beta}$ from 2.80 and save the macroscopic observables to disk

4. Perform the *collision* step i.e. evaluate f_i^c via (2.82)

5. Update the populations at the neighbouring lattice sites by *streaming* the post collision populations via 2.83

6. Update the time step by Δt and repeat the above steps until convergence or the maximum simulation time step is reached

2.2.4 Velocity space Discretization

In the previous section we saw that in the LBM framework, the Boltzmann equation is fully discretized over space, velocity and time dimensions. Multiple choices of discrete velocity sets exists that are successfully able to reproduce the hydrodynamics at macroscopic scales as modelled by Navier-Stokes equations. To better understand how the velocity space discretization is carried out, we need to first consider making the Boltzmann equation dimensionless.

2.2.4.1 Dimensionless Boltzmann Equation

Physical phenomena typically have multiple length, velocity and time scales associated with them. For instance, when studying flow of air over the wing of an airplane the associated length scales would be over a couple of meters, the relevant velocity scales could potentially be hundreds of meters per second and the time scales could range from a couple seconds to potentially several hours. At the same time, if one is studying flow in micro channels, the associated length scales would of order 10^{-6} meters and the relevant time scales could be in the range 10^3 seconds. It is key to note that the underlying physics is the same regardless the physical scales involved i.e. the Boltzmann equation remains the same in both situations.

Considering this, it is often very convenient to express the Boltzmann equation in such a way so that the physical scales associated with the problem at hand are scaled out and the quantities involved are completely dimensionless. Assuming that for a given problem at hand, l is the relevant length scale, V is a representative velocity and ρ_0 is the characteristic density, we can scale all the quantities entering the Boltzmann equation dimensionless. To this end we introduce the following dimensionless variables

$$\hat{t} = \frac{V}{l}t, \hat{\rho} = \frac{\rho}{\rho_0}, \hat{\xi}_\alpha = \frac{\xi_\alpha}{V}. \tag{2.84}$$

Moreover, since the Boltzmann distribution function, $f(\mathbf{x}, \xi, t)$ represents the probability of finding a particle with velocity ξ at position $\mathbf{x}$ at time t, and its integral over the entire velocity space yields the mass density, the units of f can be expressed as

$$[f] = \frac{[M][T]^3}{[L]^3[V]^3}, \tag{2.85}$$

where $[M], [T], [L], [V]$ represents units of the associated mass, time, length and velocity scales respectively in 3D space. Using the dimensionless quantities from 2.84 we obtain the dimensionless 3D distribution function, $\hat{f}$ as follows

$$\hat{f} = \frac{V^3}{\rho_0}f. \tag{2.86}$$

The BGK collision operator, given in 2.72 that depends on f and f^{eq} can also be made

dimensionless by substituting 2.86 into 2.72 as follows

$$\begin{aligned}\Omega(f) &= -\frac{1}{\tau}(f - f^{eq}) \\ &= -\frac{V}{l}\frac{\rho_0}{V^3}\frac{\hat{f} - \hat{f}^{eq}}{\hat{\tau}} \\ &= \frac{\rho_0}{lV^2}\hat{\Omega}\left(\hat{f}\right).\end{aligned} \tag{2.87}$$

Having scaled the BGK collision operator, we can make the Boltzmann equation dimensionless by scaling all the derivatives

$$\frac{\partial}{\partial t} = \frac{V}{l}\frac{\partial}{\partial \hat{t}} \qquad \frac{\partial}{\partial x_\alpha} = \frac{1}{l}\frac{\partial}{\partial \hat{x}_\alpha} \qquad \frac{\partial}{\partial \xi_\alpha} = \frac{1}{V}\frac{\partial}{\partial \hat{\xi}_\alpha} \tag{2.88}$$

Substituting 2.88, 2.86 into the individual terms of the Boltzmann equation we get

$$\begin{aligned}\frac{\partial f}{\partial t} &= \frac{\rho_0}{lV^2}\frac{\partial \hat{f}}{\partial \hat{t}} \\ \xi_\alpha \frac{\partial f}{\partial x_\alpha} &= \frac{\rho_0}{lV^2}\hat{\xi}_\alpha \frac{\partial \hat{f}}{\partial \hat{x}_\alpha} \\ \frac{F_\alpha}{\rho}\frac{\partial f}{\partial \xi_\alpha} &= \frac{\rho_0}{lV^2}\frac{\hat{F}_\alpha}{\hat{\rho}}\frac{\partial \hat{f}}{\partial \hat{\xi}_\alpha},\end{aligned} \tag{2.89}$$

where $\hat{F}_\alpha$ is the dimensionless body force acting on the fluid and is given by

$$\hat{F}_\alpha = \frac{l}{\rho_0 V^2}F_\alpha. \tag{2.90}$$

Now, rewriting the Boltzmann equation in terms of the dimensionless expressions we get

$$\begin{aligned}\frac{\rho_0}{lV^2}\left(\frac{\partial \hat{f}}{\partial \hat{t}} + \hat{\xi}_\alpha \frac{\partial \hat{f}}{\partial \hat{x}_\alpha} + \frac{\hat{F}_\alpha}{\hat{\rho}}\frac{\partial \hat{f}}{\partial \hat{\xi}_\alpha}\right) &= \frac{\rho_0}{lV^2}\hat{\Omega}\left(\hat{f}\right) \\ \frac{\partial \hat{f}}{\partial \hat{t}} + \hat{\xi}_\alpha \frac{\partial \hat{f}}{\partial \hat{x}_\alpha} + \frac{\hat{F}_\alpha}{\hat{\rho}}\frac{\partial \hat{f}}{\partial \hat{\xi}_\alpha} &= \hat{\Omega}(\hat{f}),\end{aligned} \tag{2.91}$$

where the factor $\rho_0/(lV^2)$ drops out from both sides. We now use equation 2.91 as the basis for discretizing it over velocity space. Lastly, in dimensionless units, the equilibrium distribution function f^{eq} becomes

$$\hat{f}^{eq} = \frac{\hat{\rho}}{(2\pi\theta)^{3/2}}\exp\left[-\frac{\left(\hat{\xi} - \hat{\mathbf{u}}\right)^2}{2\theta}\right] \tag{2.92}$$

where $\theta = RT/V^2$ is the dimensionless temperature. From here on, all references to the distribution function and Boltzmann equation will be to their non-dimensional counterparts i.e. $\hat{f}$ and $\hat{f}^{eq}$.

2.2.4.2 Velocity discretization

In the earlier sections, when discussing the LBM framework we eluded to discretizing the Boltzmann equation in velocity space using different velocity sets such as D3Q15, D3Q19. We noted that several such velocity sets along with their respective weights exist and suitably reproduce the Navier-Stokes macroscopic hydrodynamics. In this section, we describe the discretization in greater detail and illustrate how these discrete velocity sets arise in practice.

As we have pointed out so far, the moments of the Boltzmann distribution over velocity space result in the macroscopic observables such as the fluid density, ρ, and velocity, $\boldsymbol{u}$. These moments are continuous integrals over the entire velocity space and if one is primarily interested in recovering the correct macroscopic behavior, then to some extent the physics right down at the microscopic/mesoscopic level is irrelevant. The velocity moments of the distribution function are nothing more than a weighted integral of f over the velocity space. It can be shown that a vast number of functions can satisfy the integrals. So in order to simplify the physics and analysis, the goal is to discretize the Boltzmann equation/distribution function over the velocity space such that the macroscopic observable remain exactly the same. Furthermore, the velocity space discretization reduces the continuous 3D velocity space to a finite number of discrete velocities without compromising the moments of the distribution function. The main idea behind this discretization is to project the Boltzmann distribution function and the equilibrium distribution function over a Hilbert space spanned by *Hermite polynomials* [79, 150].

The goal is to seek solutions of the Boltzmann equation (2.91) and the macroscopic moments of the distribution function (dimensionless) (2.93) by projecting the dimensionless distribution function $\hat{f}$ onto a Hermite basis in the velocity space i.e. $H^n(\boldsymbol{\xi})$. In a monomial basis

$$\rho(\boldsymbol{x},t) = \int \hat{f}\left(\hat{\boldsymbol{x}},\hat{\boldsymbol{\xi}},\hat{t}\right) d\hat{\boldsymbol{\xi}} = \int \hat{f}^{eq}\left(\hat{\boldsymbol{x}},\hat{\boldsymbol{u}},\hat{\xi},\theta\right) d\hat{\boldsymbol{\xi}} \tag{2.93a}$$

$$\rho\boldsymbol{u}(\boldsymbol{x},t) = \int \boldsymbol{\xi} f(\boldsymbol{x},\boldsymbol{\xi},t)\, d\boldsymbol{\xi} = \int \hat{\boldsymbol{\xi}}\, \hat{f}^{eq}\left(\hat{\boldsymbol{x}},\hat{\boldsymbol{u}},\hat{\boldsymbol{\xi}},\theta\right) d\hat{\boldsymbol{\xi}} \tag{2.93b}$$

$$\rho E(\boldsymbol{x},t) = \int \frac{|\boldsymbol{\xi}|^2}{2} \hat{f}\left(\hat{\boldsymbol{x}},\hat{\boldsymbol{\xi}},\hat{t}\right) d\hat{\boldsymbol{\xi}} = \int \hat{f}^{eq}\left(\hat{\boldsymbol{x}},\boldsymbol{u},\hat{\boldsymbol{\xi}},\theta\right) \frac{|\hat{\boldsymbol{\xi}}|^2}{2} d\hat{\boldsymbol{\xi}}. \tag{2.93c}$$

We begin by projecting the equilibrium distribution function $f^{eq}(\rho,\boldsymbol{u},\theta,\boldsymbol{\xi})$ (2.92) onto the Hermite basis (note we depict only the dependence on $\boldsymbol{\xi}$). We do so primarily because the equilibrium distribution function has the same form as the Hermite polynomials weight function $\omega(\boldsymbol{\xi})$

$$f^{eq}(\rho,\boldsymbol{u},\theta,\boldsymbol{\xi}) = \frac{\rho}{2\pi\theta^{3/2}} \exp\left[-\frac{(\boldsymbol{\xi}-\boldsymbol{u})^2}{2\theta}\right] = \frac{\rho}{\theta^{3/2}}\omega\left(\frac{\boldsymbol{\xi}-\boldsymbol{u}}{\sqrt{\theta}}\right)$$

$$f^{eq}(\rho,\boldsymbol{u},\theta,\boldsymbol{\xi}) = \omega(\boldsymbol{\xi}) \sum_{n=0}^{\infty} \frac{1}{n!} \boldsymbol{a}^{(n),eq}(\rho,\boldsymbol{u},\theta) H^{(n)}(\boldsymbol{\xi}). \tag{2.94}$$

In (2.94), we scale the series by the weight Hermite polynomial generating function/integrating weight factor so that the integrals determining the series coefficients simplify. As mentioned in appendix B, the Hermite polynomials form a orthogonal basis and the series coefficients can easily be obtained by

$$\boldsymbol{a}^{(n),eq} = \int f^{eq}\left(\rho, \boldsymbol{u}, \theta, \boldsymbol{\xi}\right) H^{(n)}(\boldsymbol{\xi}) d\boldsymbol{\xi}, \tag{2.95}$$

where the integration is carried out over the entire velocity space of $\boldsymbol{\xi}$. Substituting the closed form for the equilibrium distribution function into 2.94 we get

$$\boldsymbol{a}^{(n),eq} = \frac{\rho}{\theta^{3/2}} \int \omega\left(\frac{\boldsymbol{\xi} - \boldsymbol{u}}{\sqrt{\theta}}\right) H^{(n)}(\boldsymbol{\xi}) d\boldsymbol{\xi}. \tag{2.96}$$

Making a simple change of variables, $\boldsymbol{\zeta} = (\boldsymbol{\xi} - \boldsymbol{u})/\sqrt{\theta}$ yields

$$\boldsymbol{a}^{(n),eq} = \rho \int \omega(\boldsymbol{\zeta}) H^{(n)}\left(\sqrt{\theta}\boldsymbol{\zeta} + \boldsymbol{u}\right) d\boldsymbol{\zeta} \tag{2.97}$$

Given that the first few Hermite polynomials are

$$H^{(0)}(\sqrt{\theta}\boldsymbol{\zeta} + \boldsymbol{u}) = 1 \tag{2.98a}$$
$$H^{(1)}(\sqrt{\theta}\boldsymbol{\zeta} + \boldsymbol{u}) = \sqrt{\theta}\boldsymbol{\zeta} + \boldsymbol{u} \tag{2.98b}$$
$$H^{(2)}(\sqrt{\theta}\boldsymbol{\zeta} + \boldsymbol{u}) = \left(\sqrt{\theta}\boldsymbol{\zeta} + \boldsymbol{u}\right)^2 - 1 \tag{2.98c}$$

we can compute the first few coefficients directly by integrating the following [79, 150]

$$a^{(0),eq} = \rho \int \omega(\boldsymbol{\zeta}) H^{(0)}(\sqrt{\theta}\boldsymbol{\zeta} + \boldsymbol{u}) d\boldsymbol{\zeta} = \rho \int \omega(\boldsymbol{\zeta}) d\boldsymbol{\zeta} = \rho \tag{2.99}$$

$$a^{(1),eq} = \rho \int \omega(\boldsymbol{\zeta}) H^{(1)}(\sqrt{\theta}\boldsymbol{\zeta} + \boldsymbol{u}) d\boldsymbol{\zeta} = \rho \int \omega(\boldsymbol{\zeta}) \left(\sqrt{\theta}\boldsymbol{\zeta} + \boldsymbol{u}\right) d\boldsymbol{\zeta} = \rho\boldsymbol{u} \tag{2.100}$$

$$a^{(2),eq} = \rho \int \omega(\boldsymbol{\zeta}) H^{(2)}(\sqrt{\theta}\boldsymbol{\zeta} + \boldsymbol{u}) d\boldsymbol{\zeta} = \rho \int \omega(\boldsymbol{\zeta}) \left(\left(\sqrt{\theta}\boldsymbol{\zeta} + \boldsymbol{u}\right)^2 - 1\right) d\boldsymbol{\zeta} = \rho\left(\boldsymbol{u}^2 - 1\right) \tag{2.101}$$

In terms of the scalar components the coefficients can be expressed as [79, 150]

$$a^{(0),eq} = \rho \tag{2.102a}$$
$$a_{\alpha}^{(1),eq} = \rho u_{\alpha} \tag{2.102b}$$
$$a_{\alpha\beta}^{(2),eq} = \rho\left(u_{\alpha\beta} + (\theta - 1)\,\delta_{\alpha\beta}\right) \tag{2.102c}$$

From the above expansions, it can be clearly seen that the first few coefficients of the Hermite series expansion of the equilibrium distribution function are exactly the macroscopic moments. This is one of the reasons why the Hermite series expansion is useful for the discretization of the Boltzmann equation, since the series coefficients themselves are directly connected to the macroscopic moments of the distribution function. It is to

be noted that equations (2.99), (2.100) and (2.101) entirely hold even for the distribution function itself i.e. $f(\boldsymbol{x}, \boldsymbol{\xi}, t)$ since the macroscopic moments are exactly the same regardless the way they are evaluated.

It can be further noted that if one is primarily interested in obtaining the correct macroscopic behaviour and satisfying the conservation laws, it is not imperative that the full continuum distribution be considered. As seen from the equations (2.99), (2.100), (2.101), the first three terms of the Hermite series expansion are sufficient to preserve the macroscopic moments. This one observation results in significant reductions in computational costs. Thus as an approximation to the distribution function, we truncate its Hermite series at order N and obtain

$$f(\boldsymbol{x}, \boldsymbol{\xi}, t) \approx f^N(\boldsymbol{x}, \boldsymbol{\xi}, t) = \omega(\boldsymbol{\xi}) \sum_{i=0}^{N} \frac{1}{n!} \boldsymbol{a}^{(n)}(\boldsymbol{x}, t) H^{(n)}(\boldsymbol{\xi}), \tag{2.103}$$

where f^N is the n^{th} order approximation to the distribution function and is able to exactly match its first N macroscopic moments in velocity space. Similarly, the equilibrium distribution can also be truncated. From equations (2.99), (2.100), (2.101) we can write a third order approximation to f^{eq} (N = 0, 1, 2) as follows [79, 150]

$$f^{eq}(\rho, \boldsymbol{u}, \theta, \boldsymbol{\xi}) = \approx \omega(\boldsymbol{\xi}) \rho \left[1 + \boldsymbol{\xi} \cdot \boldsymbol{u} + (\boldsymbol{u}\boldsymbol{u} + (\theta - 1)\,\mathbb{I})\,(\boldsymbol{\xi}\boldsymbol{\xi} - \mathbb{I})\right], \tag{2.104}$$

where $\boldsymbol{u}\boldsymbol{u}$ and $\boldsymbol{\xi}\boldsymbol{\xi}$ represents a tensor product of each respectively i.e. $\boldsymbol{u}\boldsymbol{u} = u_\alpha u_\beta$. This third order approximation to the equilibrium distribution correctly produces the first three macroscopic moments as shown in equations (2.99), (2.100), (2.101). It is also quite crucial to realize that the N^{th} order approximation to either the distribution or the equilibrium distribution function, is merely a polynomial of degree at most $2N$ is $\boldsymbol{\xi}$ and thus the integrands for computing the coefficients $\boldsymbol{a}^{(n)}$ can be conveniently expressed as

$$f(\boldsymbol{x}, \boldsymbol{\xi}, t)\, H^{(n)}(\boldsymbol{\xi}) \approx f^N(\boldsymbol{x}, \boldsymbol{\xi}, t)\, H^{(n)}(\boldsymbol{\xi}) = \omega(\boldsymbol{\xi}) p(\boldsymbol{x}, \boldsymbol{\xi}, t) \tag{2.105}$$

where $p(\boldsymbol{x}, \boldsymbol{\xi}, t)$ is a polynomial in $\boldsymbol{\xi}$ of the order of at least $2N$. The truncated equilibrium distribution can also be simplified this way to make its polynomial nature more apparent.

2.2.4.3 Gauss-Hermite Quadrature

So far we have seen how the first few terms in the Hermite series expansion of the distribution function yield the macroscopic moments, however the integration was still carried out over the entire velocity space $\boldsymbol{\xi}$. The other important reason as to why the Hermite polynomial basis was chosen to project the distribution functions is because, on this basis it is possible to evaluate integrals of certain functions by simply using a weighted discrete sum of the function values on a small number of discrete points *abscissae*, *Gauss-Hermite Quadrature*. For more details refer to appendix B.1. As a quick example, if we consider a 1-D polynomial $p(x)$ of degree N and consider its weighted integral with respect to the Hermite weight functions $\omega(x)$ then we can evaluate it exactly as follows

$$\int_{-\infty}^{\infty} \omega(x) p(x)\, dx = \sum_{i=1}^{n} \omega_i p(x_i), \tag{2.106}$$

where the n different values x_i are roots of the n^{th} order Hermite polynomial i.e. $H^{(n)}(x)$ and ω_i are its associated weights. This is the *Gauss-Hermite* quadrature rule and it states that in order to exactly integrate a polynomial of order N, a minimum of $n = (N+1)/2$ abscissae x_i and weights ω_i are needed. This rule can very easily be extended to higher dimensions as follows

$$\int \omega(\boldsymbol{x}) p(\boldsymbol{x})\, d\boldsymbol{x} = \sum_{i=1}^{n} \omega_i p(\boldsymbol{x}_i)\,. \tag{2.107}$$

With regards to our issue at hand, we can use the Gauss-Hermite quadrature rules to evaluate the series coefficients, $\boldsymbol{a}^{(n),eq}$. Using equations (2.103) and (2.105) we can write

$$f^{eq}(\rho, \boldsymbol{u}, \theta, \boldsymbol{\xi})\, H^{(n)}(\boldsymbol{xi}) \approx f^{N,eq}(\rho, \boldsymbol{u}, \theta, \boldsymbol{\xi})\, H^{(n)}(\boldsymbol{\xi}) = \omega(\boldsymbol{\xi}) Q(\rho, \boldsymbol{u}, \theta, \boldsymbol{\xi})\,. \tag{2.108}$$

Using equation (2.108) to compute its series coefficients we obtain

$$\boldsymbol{a^{(n),eq}} = \rho \int f^{N,eq}(\rho, \boldsymbol{u}, \theta, \boldsymbol{\xi})\, H^{(n)}(\boldsymbol{\xi}) d\boldsymbol{\xi} = \rho \sum_{i=0}^{n} \omega_i Q(\rho, \boldsymbol{u}, \theta, \boldsymbol{\xi}_i)\,, \tag{2.109}$$

where $\boldsymbol{\xi}_i$ are discrete velocities that are roots of the n^{th} order Hermite polynomial and ω_i are a set of discrete weights corresponding to those roots. Now in terms of these discrete velocities i.e velocity abscissae the third order approximation to the equilibrium distribution function simplifies to

$$f_i^{eq} = \omega_i \rho \left[1 + \xi_{i\alpha} u_\alpha + \frac{1}{2}\left(u_\alpha u_\beta + (\theta - 1)\,\delta_{\alpha\beta}\right)\left(\xi_{i\alpha}\xi_{i\beta} - \delta_{\alpha\beta}\right)\right] \tag{2.110}$$

We can further simplify (2.110) by assuming the fluid flow is *isothermal* i.e. $\theta = 1$ and by scaling the discrete velocities ξ_i by $\sqrt{3}$ as this factor repeatedly occurs in the roots of the N^{th} order Hermite polynomial.

$$\boldsymbol{c}_i = \frac{\boldsymbol{\xi}_i}{\sqrt{3}}. \tag{2.111}$$

For more details refer to appendix B.1.

So far we have shown with some rigor as to why the Hermite expansion is vital and how it naturally leads to discretization of the distribution functions in velocity space. This however, leads to the question as to which set of discrete velocities one can choose. The answer to this question lies in balancing the numerical accuracy with which the simulations must match up with the Navier-Stokes hydrodynamics with the numerical/computational costs to be incurred with increasing the number of discrete velocities used in the simulations. As discussed earlier, the most commonly used velocity set when studying fluid flows are the D3Q15 and D3Q19 velocity sets as they strike a good balance between numerical accuracy and computational costs.

2.2.5 Boundary conditions

In solving PDEs, *boundary conditions* play an essential role. Given that the NSE describe the fluid flow in general, additional details regarding the flow domain boundaries, and the

value of the macroscopic quantities ρ, $\boldsymbol{u}$ or $\nabla \boldsymbol{u}$ at those boundaries need to be specified in order to obtain a unique solution to the problem at hand. From all the possible solutions to the NSE, the boundary conditions allow one to single out the solution specific to the flow domain under consideration.

Within the Lattice Boltzmann framework however, the quantity that is solved for is the discrete particle distribution function on the lattice i.e. $f_i(\boldsymbol{x}, t)$. This entails, that the boundary conditions are rather specified on the particle populations rather than imposing them on the macroscopic observables i.e. ρ and $\boldsymbol{u}$. Due to this, there are a plethora of boundary conditions schemes that one can use to restrict the values of the particle populations at the domain boundaries in order to match the macroscopic observables with varying degrees of numerical accuracy [8, 30, 48, 79, 185].

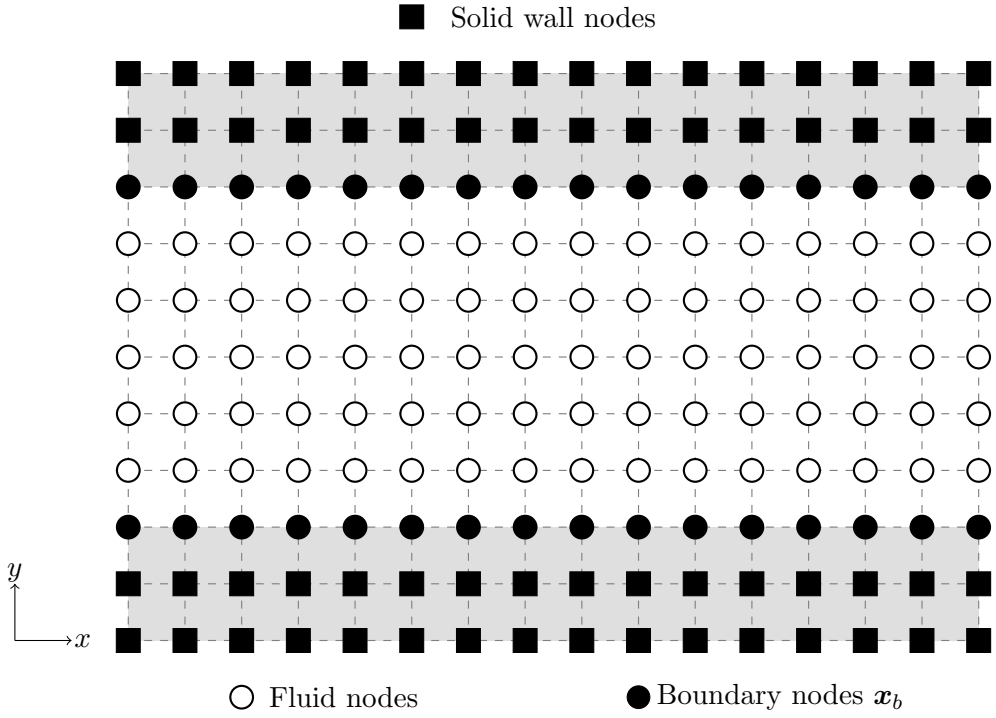

Figure 2.6: Different types of lattice nodes in a 2D rectangular channel. The shaded area represents solid wall where the LBE must not be solved

In the LB framework, since the Boltzmann equation is discretized in space $\boldsymbol{x}$, the value of the particle distribution functions is computed on a lattice. When bounded domains are discretized in this manner, the notion of different node types arises. In this discrete lattice, each node can be categorized as either (a) *Fluid node* (b) *Boundary node* or (c) *solid wall node*. By definition a *fluid node* is simply the bulk where LBE applies and are exclusively surrounded by either other fluid nodes or boundary nodes. A *boundary node* has at least one link to a fluid node and a solid wall node. Lastly, a *solid* node is one where LBE does not apply and is surrounded by either boundary nodes or other solid nodes. In figure 2.6 we illustrate the different node types for a 2D rectilinear channel. Such a classification of nodes into the three categories is important since the manner with

which the particle populations are updated depends on the node type. Since *fluid nodes* are exclusively surrounded by either other fluid nodes or boundary nodes, updating the particle populations on them follows the standard collision/streaming update process as described in earlier sections. The problem of *boundary conditions* in LB arises when one has to update the particle distributions at the boundary nodes since the populations streaming out of the boundary nodes to the adjacent fluid nodes are unknown. We illustrate this problem graphically in 2.7

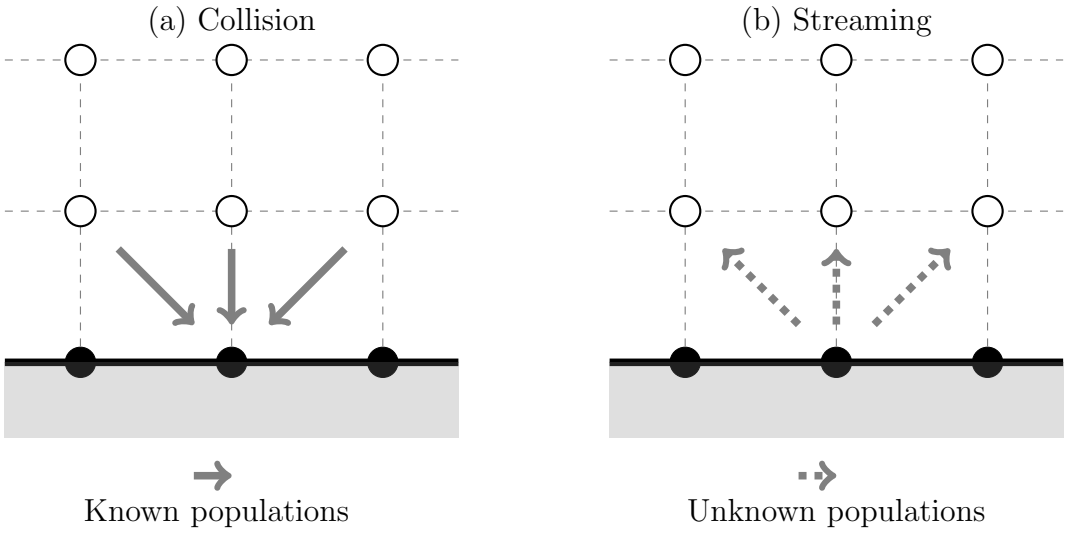

Figure 2.7: The *boundary condition* issue in the LB framework (a) incoming particle populations to a boundary node are *known* (b) whereas the populations values to be streamed back to the fluid nodes from the boundary nodes are *unknown*

In short, we can state that the role of *boundary conditions* in the LB framework is to prescribe means through which proper values can be assigned to the population that ought to stream outwards from boundary nodes into the fluid region. In comparison to traditional computational fluid dynamics (CFD) methods, prescribing boundary conditions within the LB framework is more involved [48,83,113] since the boundary conditions are set at the *mesoscopic* scale i.e. on the particle populations. Since there are more degrees of freedom at this scale i.e. larger number of f_i at each lattice node setting proper boundary conditions on each becomes more involved [79]. Even the macroscopic observables are simply the moments of the particle populations, the inverse relationship is rather *non-trivial* and non-unique. Due to this non-uniqueness, there exists a plethora of hydrodynamically consistent schemes for prescribing boundary conditions on the discrete populations. Despite the large number, most of the schemes can largely be grouped under two different approaches (a) *link-wise* approach where the boundary nodes lie on lattice links and (b) *wet node* approach where the boundary nodes like directly on lattice nodes.

Another aspect that needs to be addressed is the *accuracy* [1] and *exactness* [2] with

[1] How the error in the solution scales with discretization

[2] Ability of a method to resolve a fluid flow of certain order i.e. if a method is second order exact, it

which any given LB boundary condition scheme models the true fluid flow. As per the Chapman-Enskog expansion [28] where the distribution function is expressed as a perturbation series in ϵ[3] i.e.

$$f_i = f_i^{eq} + \epsilon f_i^{(1)} + \epsilon^2 f_i^{(2)} + \mathcal{O}(\epsilon^3) \tag{2.112}$$

the LB framework is second order spatially accurate in the bulk i.e. its error scales as $\mathcal{O}(\Delta x^2)$. This means that the LB method is second order accurate and can exactly reproduce fluid flows up to that order i.e. Couette and quadratic Poiseuille flows. To match the Navier-stokes hydrodynamics in the bulk, the Chapman-Enskog analysis need only to worry about the macroscopic conservation equations. Near the boundary however one also has to recover the exact values of the macroscopic quantities from the particle populations. This entails that in order to be able to resolve the populations f_i at a fluid boundary with second order spatial accuracy, one needs to consider the expansion [55, 113, 186]

$$f_i = f_i^{eq} + \epsilon f_i^{(1)} + \mathcal{O}(\Delta x^2) \tag{2.113}$$

Although this expansion matches the second order accuracy of the LBE in the bulk, it fails to be exact for fluid flows of order $\mathcal{O}(\Delta x^2)$ and higher due to the exclusion of the $\epsilon^2 f^{(2)}$ term in the expansion. This implies that parabolic flows are exactly captured in the bulk but fail to be properly resolved near the boundaries. Similarly, in order to be second order exact near the boundaries, one needs to consider third order accurate schemes i.e. to resolve the populations as [47, 48, 101]

$$f_i = f_i^{eq} + \epsilon f_i^{(1)} + \epsilon^2 f_i^{(2)} + \mathcal{O}\left(\Delta x^3\right) \tag{2.114}$$

The choice of second or third order accurate scheme depends on how well we intend to model the fluid flow versus the computational cost one is willing to incur in terms of the spatial discretization. This trade off is also dependent on the problem at hand in the domain involved.

2.2.5.1 Periodic Boundary Conditions

The *periodic boundary conditions* apply only when the underlying fluid flow i.e. the Navier-Stokes solution of the flow is periodic to begin with. Similar to the PBC involved in MD simulations, PBC in the LB framework mean that the fluid leaving one end of the domain immediately enters the domain from the opposing side. As can be seen evidently, the PBCs conserve mass and momentum of the flow by definition. The periodic boundary conditions also entail that an external source of momentum exists, otherwise any initial flow conditions will decay over time to a homogeneous velocity throughout the domain [76].

Using periodic boundary conditions is often justified when one is interested in studying a finite portion of a larger flow field which is repeated. For example, for small Reynolds

can exactly reproduce a fluid flow whose third order and higher velocity gradients vanish

[3] ϵ is related to the Knusden number of the flow which is given by Kn= l_{mfp}/l, where l_{mfp} is the mean free path and l is the macroscopic length scale

numbers laminar flow in a long channel can be quite well approximated by imposing periodic boundary conditions to the LB equations. Another example is when studying turbulence in physical systems of size L. Although turbulence is not periodic, approximating such systems with PBC introduces finite size effects, but the underlying physics at length scales much smaller than L is still well approximated. More frequently, PBCs help simulating 2D flow problems with existing 3D simulation code by easily adopting periodic flow along one of the cartesian directions. Imposing periodic condition on the macroscopic quantities in a system of size L can be easily done by requiring

$$\rho\left(\boldsymbol{x},t\right)=\rho\left(\boldsymbol{x}+\boldsymbol{L},t\right) \tag{2.115}$$

$$\rho\boldsymbol{u}(\boldsymbol{x},t)=\rho\boldsymbol{u}(\boldsymbol{x}+\boldsymbol{L},t) \tag{2.116}$$

To realize this in LB framework, we have to impose similar conditions on the discrete populations when they are computed on the nodes residing on the boundary being treated as periodic i.e.

$$f_i(\boldsymbol{x},t)=f_i(\boldsymbol{x}+\boldsymbol{L},t). \tag{2.117}$$

We illustrate this in figure 2.8 for the D2Q9 model. For computational convenience, we add a set of *virtual/ghost* nodes as these facilitate updating adjacent node populations. Before streaming, the node populations are copied over to the virtual nodes and the local values are updated subsequently.

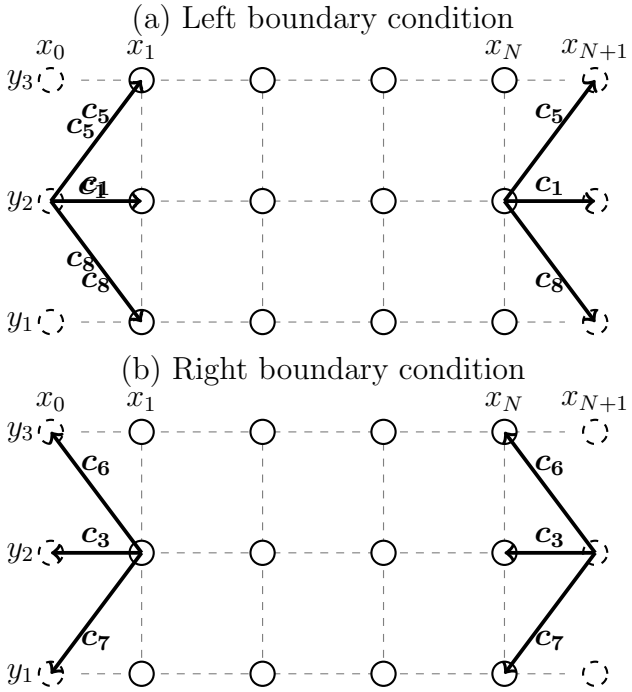

Figure 2.8: Illustration of the periodic boundary conditions in the D2Q9 model. The dotted circles are *virtual nodes* added for computational convenience at $x_0 = x_1 - \Delta x$ and $x_{N+1} = x_N + \Delta x$

In terms of implementation, following 2.8, we can update the populations, f_i on the

left boundary as

$$f_1(\boldsymbol{x}_0, y_2 t) = f_1(\boldsymbol{x}_N, y_2, t) \tag{2.118}$$
$$f_5(\boldsymbol{x}_0, y_2, t) = f_5(\boldsymbol{x}_N, y_2, t) \tag{2.119}$$
$$f_8(\boldsymbol{x}_0, y_2, t) = f_8(\boldsymbol{x}_N, y_2, t). \tag{2.120}$$

Similarly, we update the populations at the right boundary as

$$f_3(\boldsymbol{x}_{N+1}, y_2, t) = f_3(\boldsymbol{x}_1, y_2, t) \tag{2.121}$$
$$f_6(\boldsymbol{x}_{N+1}, y_2, t) = f_6(\boldsymbol{x}_1, y_2, t) \tag{2.122}$$
$$f_7(\boldsymbol{x}_{N+1}, y_2, t) = f_7(\boldsymbol{x}_1, y_2, t). \tag{2.123}$$

2.2.5.2 Bounce Back Approach: Solid boundaries

The *bounce-back* approach is a quite commonly used scheme to implement the no-slip boundary condition between a fluid-solid interface [42, 46, 81]. Despite its age, it is the most commonly used boundary condition scheme in LB simulations primarily due to its ease of implementation in software. Since the populations are bounced back to their source of origin, this implicitly implies that there is a net zero flux of populations across the wall. And it is important to note that the bounce back is different from reflection where the velocities in only one direction is reversed. This way, implementing the bounce back scheme also implies that the fluid has no tangential velocity component along the wall, thus effectively enforcing the no-slip boundary condition. The working principle behind this scheme is to simply reverse the populations incoming to a rigid wall back to its source of origin. We illustrate this schematically for a wall at rest in figure 2.9

(a) Incoming velocity at t (b) Bounce back velocity at $t + \Delta t$

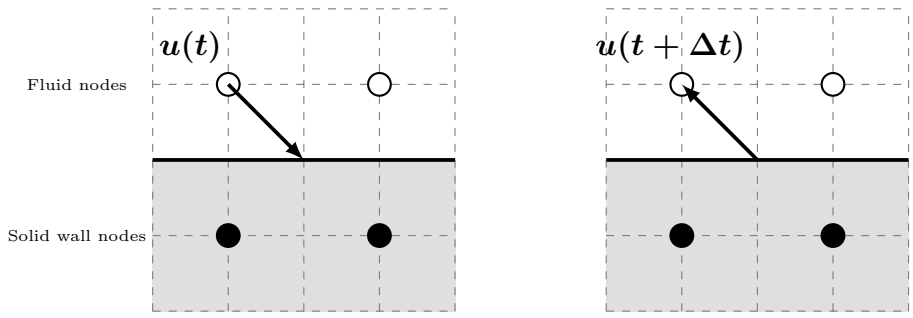

Figure 2.9: Illustration of how a incoming velocity/population is bounced back to its source of origin, both the normal and tangential components of the velocity are reversed effectively rendering the relative fluid velocity at the wall to zero

In practice the bounce back approach can be implemented in two distinct ways i.e (a) **fullway bounce-back** where particles/populations are considered to stream the complete link path from the fluid/boundary node to the solid wall node. The velocity/population is then inverted in the subsequent collision step (b) **halfway bounce-back** where the particles are considered to traverse only half the streaming distance and

are reverted back to their source node at half time step. This way the bounce back takes place during the streaming step itself. Both of these approaches requires specific modifications to the LB framework. In the fullway bounce back scheme solid nodes are required in order to store the populations which are then bounced back at the next collision step whereas in the other approach, explicit solid nodes are not needed as the bounce back happens half way through and the populations are updated during streaming step itself. Considering this it can be said that the fullway bounce-back modifies the collision step in the algorithm whereas the halfway approach modifies the streaming step. Despite the differences in the implementation the underlying assumption that the solid wall boundary lies approximately midway between the solid and the fluid/boundary nodes is the same in either case. It is important to note that the solid boundary does not reside on the solid nodes themselves. The reason for this becomes apparent when one carries out the Chapman-Enskog expansion of the distribution functions near the boundary. It can be shown that placing the boundary exactly on top of the lattice nodes introduces a first order error even for straight boundaries whereas if the boundary location is updated to be approximately in the middle of the solid and fluid/boundary nodes, the method becomes *second order* accurate near the walls.

2.2.5.3 Resting Walls

In this case the boundary walls are at rest and not in motion. In this scenario, the particle populations leaving a boundary/fluid node $\boldsymbol{x_b}$ at time t meets the surface halfway i.e. at time $t+\frac{\Delta t}{2}$ upon which they are bounced back with perfect velocity reversal i.e. $\boldsymbol{c_i} = -\boldsymbol{c_i}$, thus arriving back at the boundary node at time $t + \Delta t$. In implementation, this can be expressed as show in equation (2.126) and illustrated graphically in figure 2.10 (for the D2Q9 scheme)

$$f_2(\boldsymbol{x}_b, t + \Delta t) = f_4(\boldsymbol{x}_b, t) \tag{2.124}$$
$$f_5(\boldsymbol{x}_b, t + \Delta t) = f_7(\boldsymbol{x}_b, t) \tag{2.125}$$
$$f_6(\boldsymbol{x}_b, t + \Delta t) = f_6(\boldsymbol{x}_b, t) \tag{2.126}$$

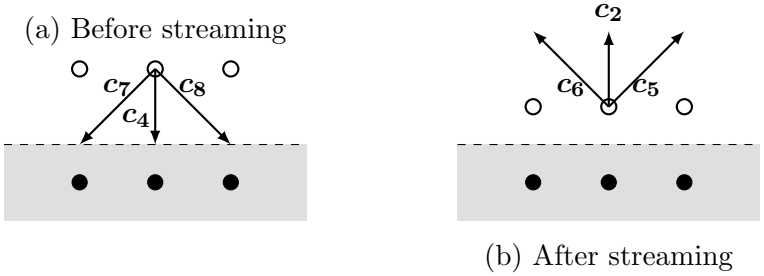

Figure 2.10: Implementation of the bounce back scheme for a stationary wall in the D2Q9 case. The shaded area is the solid wall with the solid nodes within where the LBE does not apply. The dashed line represents the no-slip physical wall boundary

2.2.5.4 Moving Walls

Having shown the bounce back boundary condition implementation for the no-slip boundary condition in the previous section, we investigate the same in for the case where the boundary walls are in motion. In this case, if the no-slip boundary condition has to be enforced the fluid hitting the boundary walls either has to gain or lose certain amount of momentum in order to satisfy Galilean invariance [81]. One way to show this would be to transform to the rest frame of the wall, perform a standard bounce back scheme there and then transform back to the initial frame. Doing this results in the following bounce back scheme for a wall moving with velocity $\boldsymbol{u_w}$

$$f_i(\boldsymbol{x_b}, t + \Delta t) = f_i(\boldsymbol{x_b}, t) - 2\omega_i \rho_w \frac{\boldsymbol{c_i} \cdot \boldsymbol{u_w}}{c_s^2}, \tag{2.127}$$

where the subscript w denotes the density at the location of the wall boundary which presumably is at $\boldsymbol{x_w} = \boldsymbol{x_b} + \frac{1}{2}\boldsymbol{c_i}\Delta t$

Since in our study we have a sheared system, the moving wall boundary conditions need to be implemented properly. To this end, we give a concrete example on how this can be achieved for the D3Q15 scheme [8]. As mentioned earlier, for a sheared system in the y direction, given the wall is located at $z = 0$, a no slip boundary condition implies $\sum_i f_i e_{iz} = 0$. This can be realized by requiring the following

$$f_5 + f_7 + f_8 + f_9 + f_{10} = f_6 + f_{11} + f_{12} + f_{13} + f_{14} \tag{2.128}$$

In order to ensure no slip along the wall in the x direction we can set $\sum_i f_i e_{ix} = 0$ by

$$f_1 + f_7 + f_{10} + f_{11} + f_{14} = f_3 + f_8 + f_9 + f_{12} + f_{13} \tag{2.129}$$

Now, given the wall is sheared along the y direction, to ensure no-slip the fluid velocity at the wall needs to match the wall velocity i.e. u_y. This can be established by requiring $\sum_i f_i e_{i,y} = \rho u_y$. This implies that certain distributions need to satisfy the following constraint

$$f_2 + f_7 + f_8 + f_{11} + f_{12} - f_4 - f_9 - f_{10} - f_{13} - f_{14} = \rho u_y \tag{2.130}$$

Now for the wall at $z = 0$, there are five unknown distributions i.e. $f_5, f_7, f_8, f_9, f_{10}$. In order to determine these, two additional constraints apart from the above three are needed. Using symmetry arguments, the following relation can be inferred

$$f_7 - f_8 = f_{10} - f_9 \tag{2.131}$$

Lastly, conservation of mass can be easily obtained by setting $f_5 = f_6$. Now using these constraints, the five unknown populations can be easily solved to give

$$f_5 = f_6 \tag{2.132a}$$

$$f_7 = \frac{1}{4}\left(-f_1 - f_2 + f_3 + f_4 - f_{11} + f_{12} + 3f_{13} + f_{14} + \rho u_y\right) \tag{2.132b}$$

$$f_8 = \frac{1}{4}\left(f_1 - f_2 - f_3 + f_4 + f_{11} - f_{12} + f_{13} + 3f_{14} + \rho u_y\right) \tag{2.132c}$$

$$f_9 = \frac{1}{4}\left(f_1 + f_2 - f_3 - f_4 + 3f_{11} + f_{12} - f_{13} + f_{14} - \rho u_y\right) \tag{2.132d}$$

$$f_{10} = \frac{1}{4}\left(-f_1 + f_2 + f_3 - f_4 + f_{11} + 3f_{12} + f_{13} - f_{14} - \rho u_y\right) \tag{2.132e}$$

Considering the simplicity of this scheme, there are a few advantages and disadvantages to this approach. The bounce back approach is a numerical stable scheme even in the case when the BGK relaxation parameter approaches the instability limit. Secondly, since this scheme is based on reflections, mass conservation is guaranteed and this is an important feature to consider in the cases when absolute mass is important and lastly it is extremely straightforward to implement and scale to any number of spatial dimensions. One major disadvantage of this approach is when curved boundaries are considered. The bounce back approach is only capable of approximating curved surfaces through *staircase* shaped lattice nodes around the boundary. Moreover, this approach only guarantees first/second order accuracy when the boundary wall either aligns with the lattice nodes or is midway between the boundary and solid nodes respectively. Both of these conditions get violated when the geometries are curved and makes the scheme first order accurate at best [79]

2.2.6 External Forces

Forces play a central role in hydrodynamics so it is important that we discuss how external forces are accommodated within the LB framework and how the implementation is modified to take the forces into account. In hydrodynamics, one deals more with force densities rather than forces themselves since the momentum conservation equation (2.59) is a PDE for momentum density. Net forces on surfaces are obtained by integrating surface stresses/bulk force densities over the surface/volume of the object/region of interest respectively. Equivalently one can state that a force density is a source for momentum density within a fluid. Examples for where taking external forces into account is vital include studying charged and magnetic particles immersed in a fluid which requires one to consider the effects of external forces on the fluid as the particles interact with each other as well as the surroundings. This becomes extremely important when modelling the effects of external electric fields on charged particles immersed in electrolytes in a confined space [190,191]. When considering incompressible flows the mechanism behind a pressure gradient field can be considered as a *divergence-free* fluid body force. Moreover, as we will see in subsequent chapters when modelling the dynamics of particles immersed in fluid i.e. studying the fluid particle interactions via the *immersed boundary method*, one tends to model the particle surfaces as a continuum of point-sized forces acting on the fluid media. In a nutshell the LB update algorithm in the presence of external forces can be broken down as follows [79]

1. Determine the force density F at time t
2. Compute the macroscopic observable i.e. ρ and $\boldsymbol{u}$ by

$$\rho = \sum_i f_i \qquad \boldsymbol{u} = \frac{1}{\rho}\sum_i f_i \boldsymbol{c}_i + \frac{\boldsymbol{F}\Delta t}{2\rho} \tag{2.133}$$

3. Determine the equilibrium distribution, $f_i^{eq}(\rho, \boldsymbol{u})$ and build the BGK collision operator

$$\Omega_i = -\frac{1}{\tau}\left(f_i - f_i^{eq}\right) \tag{2.134}$$

4. Optionally, compute the stress tensor resulting from the fluid velocity and external forces

$$\sigma_{\alpha\beta} \approx -\left(1-\frac{\Delta t}{2\tau}\right)\sum_i f_i c_{i\alpha}c_{i\beta} - \frac{\Delta t}{2}\left(1-\frac{\Delta t}{2\tau}\right)(F_\alpha u_\beta + u_\alpha F_\beta) \tag{2.135}$$

5. Update the momentum source term S_i due to the external force

$$S_i = \left(1-\frac{\Delta t}{2\tau}\right)\omega_i\left(\frac{c_{i\alpha}}{c_s^2} + \frac{c_{i\alpha}c_{i\beta}-c_s^2\delta_{\alpha\beta}}{c_s^4}\right)F_\alpha \tag{2.136}$$

where the source term S_i is related to F_i via

$$S_i = \left(1-\frac{1}{2\tau}\right)F_i \tag{2.137}$$

6. Update the post collision populations under the effect of the collision as well as the source term, S_i

$$f_i = f_i + (\Omega_i + S_i)\,\Delta t \tag{2.138}$$

7. Stream the populations to neighboring lattice nodes

8. Update time step and go back to step 1

2.2.6.1 Discretization

In section 2.2.4 we reviewed how one can reduce the continuous velocity space $\boldsymbol{\xi}$ to finite velocity sets $\boldsymbol{c}_i$ while preserving the model's ability to properly reproduce the hydrodynamics at the macroscopic scales. This was accomplished by approximating the distribution function via a linear sum of Hermite polynomials in $\boldsymbol{\xi}$ and using the *Gauss-Hermite* quadrature rules to convert the moment integrals over velocity space to discrete sum. Now we discretize the continuous Boltzmann equation (2.91)

$$\frac{\partial f}{\partial t} + \xi_\alpha\frac{\partial f}{\partial x_\alpha} + \frac{F_\alpha}{\rho}\frac{\partial f}{\partial \xi_\alpha} = \Omega(f) \tag{2.139}$$

To proceed with the discretization, we focus on the external force/source term

$$S = \frac{F_\alpha}{\rho}\frac{\partial f}{\partial \xi_\alpha} \tag{2.140}$$

and make use of the derivative property of the Hermite polynomials i.e.

$$\omega(\boldsymbol{\xi})\boldsymbol{H}^{(n)} = (-1)^n\boldsymbol{\nabla}_\xi^n\omega(\boldsymbol{\xi}) \tag{2.141}$$

Using (2.141), we begin by rewriting the Hermite expansion of the distribution function

$$f(\boldsymbol{x},\boldsymbol{\xi},t) \approx \omega(\boldsymbol{\xi})\sum_{n=0}^{N}\frac{1}{n!}\boldsymbol{a}^{(n)}(\boldsymbol{x},t)\cdot\boldsymbol{H}^{(n)}(\boldsymbol{\xi}) \tag{2.142}$$

$$\approx \sum_{n=0}^{N}\frac{(-1)^n}{n!}\boldsymbol{a}^{(n)}\cdot\boldsymbol{\nabla}_{\boldsymbol{\xi}}^n\omega. \tag{2.143}$$

Using (2.143) the expansion (2.139) can be modified as follows

$$\frac{\boldsymbol{F}}{\rho}\cdot\nabla_{\xi}f \approx \frac{\boldsymbol{F}}{\rho}\cdot\sum_{n=0}^{N}\frac{(-1)^n}{n!}\boldsymbol{a}^{(n)}\cdot\nabla_{\xi}^{n+1}\omega \tag{2.144a}$$

$$\approx \frac{\boldsymbol{F}}{\rho}\cdot\omega\sum_{n=1}^{N}\frac{n}{n!}\boldsymbol{a}^{n-1}\cdot\boldsymbol{H}^{(n)}. \tag{2.144b}$$

Following equation (2.144b), the discretization in velocity space can be performed directly by replacing the continuous variable $\boldsymbol{\xi}$ by the discrete set $\boldsymbol{c}_i$. For convenience, we scale the velocities $\boldsymbol{c}_i = \boldsymbol{\xi}_i/\sqrt{3}$ and normalize the respective weights, ω_i. With these substitutions, we then obtain the discrete form of the external forcing term to be included in the discrete LB equation

$$W_i(\boldsymbol{x},t) = -\frac{\omega_i}{\omega(\boldsymbol{\xi})}\frac{\boldsymbol{F}}{\rho}\cdot\nabla_{\boldsymbol{\xi}}f|_{\boldsymbol{\xi}\to\sqrt{3}\boldsymbol{c}_i}. \tag{2.145}$$

With the forcing term being discretized, the discrete Boltzmann equation can be updated to include (2.145) as follows

$$\frac{\partial f_i}{\partial t} + c_{i\alpha}\frac{\partial f_i}{\partial x_\alpha} = \Omega_i + W_i, \qquad i = 0,\ldots,q-1 \tag{2.146}$$

Lastly, the truncation of the forcing term, $W_i(x,t)$ up to second velocity order (N = 2), corresponding to the expansion of f^{eq} reads

$$W_i = \omega_i\left(\frac{c_{i\alpha}}{c_s^2} + \frac{\left(c_{i\alpha}c_{i\beta} - c_s^2\delta_{\alpha\beta}\right)u_{\alpha\beta}}{c_s^4}\right)F_\alpha \tag{2.147}$$

The first three velocity moments of the forcing term are

$$\sum_i W_i = 0 \tag{2.148a}$$

$$\sum_i W_i c_{i\alpha} = F_\alpha \tag{2.148b}$$

$$\sum_i W_i c_{i\alpha}c_{i\beta} = F_\alpha u_\beta + u_\alpha F_\beta \tag{2.148c}$$

With the external forcing term discretized in the velocity space as described above, one solves the following modified version of the LBE including the forcing term on a discrete lattice

$$f_i\left(\boldsymbol{x}+\boldsymbol{c}_i\Delta t, t+\Delta t\right) = f_i\left(\boldsymbol{x},t\right) - \frac{\Delta t}{\tau}\left(f_i(\boldsymbol{x},t) - f_i^{eq}(\boldsymbol{x},t)\right) + W_i\left(\boldsymbol{x},t\right) \tag{2.149}$$

2.2.7 Thermal Lattice-Boltzmann

So far, we have discussed the LB framework with the assumptions that thermal fluctuations in the fluid are irrelevant at length scales involved. However, when studying submicron dynamics of colloidal suspensions in channels and flows, thermal fluctuations become extremely important. The idea of Brownian motion of a particle suspended in a fluid dates back to Einstein's original work [38]. Diffusion of lone colloids can be modelled as simple Brownian motion, but involving several colloids requires one to properly model the hydrodynamic interactions along with the individual Brownian motions [39]. To efficiently and accurately study such systems through Lattice-Boltzmann the current formulation must be modified to include thermal effects.

Thermal fluctuations were first included in the LB framework by Ladd [81] in order to model Brownian motion of solid particles in a fluid medium. Following Landau & Lifschitz, Ladd applied thermal noise to the fluid stress tensor only, which gave good results for cases near thermal equilibrium. However, discretizing the Boltzmann equation to obtain the Lattice-Boltzmann equation results in lattice-specific independent degrees of freedom commonly referred to as *ghosts* [161]. These *ghosts* do not enter the macroscopic equations of mass and momentum conservation and as the moments of the LB particle distributions corresponding to momentum and energy are coupled, noise applied purely to the stress tensor results in poor temperature reproduction in the fluid. This is likely because the isothermal LB model does not conserve energy. If the ghost modes are not properly accounted for when calculating the macroscopic moments the temperature reproduction is far from ideal. However Adhikari et.al. in [1] demonstrated that proper inclusion of *ghosts* modes in the moment calculations, improves local temperature reproduction in the isothermal LB model.

In our work we follow the method described in [117] and implemented by Mackay et.al in [97] where a standard integration scheme as specified in [161] in use. A simple finite difference scheme is employed to solve the discrete Boltzmann equation 2.149. Solving the Boltzmann equation this way yields

$$\eta = \rho\left(\tau - \frac{\Delta t}{2}\right) v_c^2/3, \qquad \Lambda = \eta\left(5/3 - 3a_0/v_c^2\right) \tag{2.150}$$

for the shear and bulk viscosity respectively and $v_c = \Delta x/\Delta t$. In a real fluid, finite temperature results in fluctuations in the local fluid velocity. These spontaneous fluctuations produce local stresses in the fluid and ought to be governed by the *fluctuation-dissipation* theorem i.e.

$$\left\langle s_{\alpha\beta}(\boldsymbol{x}, t), s_{\gamma\nu}(\boldsymbol{x}, t)\right\rangle = 2\eta_{\alpha\beta\gamma\nu} k_B T \delta\left(\boldsymbol{x} - \boldsymbol{x}'\right)\delta\left(t - t'\right) \tag{2.151}$$

In practice, random noise is added to the system through the discrete forcing term, W_i (2.149). To keep analysis easier, we decompose the forcing term into two separate parts

$$W_i = p_i + \zeta_i. \tag{2.152}$$

The p_i term is chosen in order to satisfy the constraints imposed on the forcing term,

namely

$$\sum_i W_i = 0 \tag{2.153}$$

$$\sum_i W_i c_{i\alpha} = F_\alpha \tag{2.154}$$

$$\sum_i W_i c_{i\alpha} c_{i\beta} = F_\alpha u_\beta + u_\alpha F_\beta \tag{2.155}$$

while ζ_i are required to satisfy

$$\sum_i \zeta_i = 0 \tag{2.156a}$$

$$\sum_i \zeta_i c_{i\alpha} = 0 \tag{2.156b}$$

in order to conserve mass and momentum globally in the system. Higher order moments of ζ_i are chosen such that the fluctuating stress tensor satisfies the fluctuation dissipation theorem (2.151). Having implemented the noise in this manner, the fluid acts as an effective heat bath for the particles immersed within it. For complete details, see [117] and [97].

2.2.8 Immersed Boundary Method

Immersed boundary (IB) methods were first developed by Peskin [127] in order to study blood flows in human cardiac valves. A major advantage of this method as demonstrated by Peskin is that method/techniques used for solving Navier-Stokes (NS) equations on cartesian domains can now be applied to problems with immersed objects/boundaries. Following the approach in [105], Conventional methods for studying flows past immersed rigid bodies constituted constructing grids that conformed to the geometry of the immersed rigid body [105]. First a grid covering the surface of the body, Γ_b enclosing a volume $\mathcal{D}_b$ is generated. This is then used as a boundary condition to generate a grid covering the fluid domain i.e. $\mathcal{D}_f$. The NS equations are then rewritten and discretized in some curvilinear coordinates dictated by the local geometry imposed by the immersed rigid body.

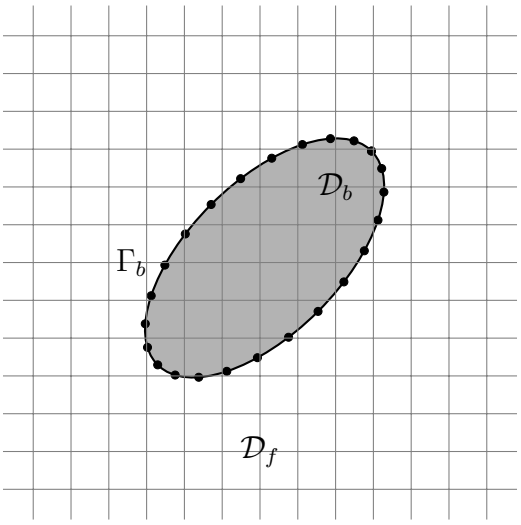

Figure 2.11: Illustration of the coupling between nodes on the particle surface with the fluid mesh background as per the *immersed boundary* (IB) method. The immersed body occupies the volume, $\mathcal{D}_b$ enclosed by Γ_b and $\mathcal{D}_f$ is the ambient volume occupied by the fluid.

IB methods employ a completely different approach where the boundary Γ_b is replaced by a field of point forces acting from a mesh of points covering the rigid body surface. In IB methods, the rigid body surface is discretized using a mesh of points of sufficient density so as to appropriately cover the geometry of the immersed object. The cartesian grid covering the fluid region, $\mathcal{D}_f$ is then constructed independently of the rigid body. Since the rigid body mesh and the fluid cartesian grid were independently generated, incorporating the no-slip boundary on Γ_b requires modifying NS equations near Γ_b. The advantage of this approach is that despite the modifications to the NS equations they can be discretized using any appropriate finite-difference scheme without having to resort to any curvilinear coordinates respecting the local geometry imposed by the immersed rigid body.

Imposing boundary conditions on Γ_b is central to any immersed boundary method. For instance, an incompressible flow around Γ_b in 2.11 is fully described by the following set of equations

$$\begin{aligned}
&\frac{\partial \mathbf{u}}{\partial t} + \mathbf{u}\cdot\nabla\mathbf{u} + \frac{1}{\rho}\nabla p - \frac{\mu}{\rho}\nabla^2\mathbf{u} = 0 \\
&\nabla\cdot\mathbf{u} = 0 \,\text{in}\, \mathcal{D}_f \\
&\mathbf{u} - \mathbf{u}(\Gamma_b) = 0 \,\text{on}\, \Gamma_b,
\end{aligned} \tag{2.157}$$

where $\mathbf{u}$ is the fluid velocity, p is the fluid pressure, ρ and μ are the fluid density and viscosity respectively. Conventional methods generally discretize the NS equations on a grid system which respects the rigid body geometry. This way imposing the *no-slip* boundary condition becomes straightforward. However in an IB scheme, the NS equations are discretized on a grid irrespective of the rigid body and the *no-slip* boundary condition is imposed via directly modifying the NS equations via the addition of a forcing term.

The forcing term, f_b acts as a source term in the NS equations and acts to incorporate the boundary effect imposed by the immersed body. The modified NS equations can then be written as

$$\begin{aligned} &\frac{\partial \mathbf{u}}{\partial t} + \mathbf{u} \cdot \nabla \mathbf{u} + \frac{1}{\rho} \nabla p - \frac{\mu}{\rho} \nabla^2 \mathbf{u} = f_b \\ &\nabla \cdot \mathbf{u} = 0 \, \text{in} \, \mathcal{D}_f + \mathcal{D}_b \end{aligned} \tag{2.158}$$

As the immersed body's surface is discretized into a set of nodes, the no-slip boundary condition on its surface is now enforced at each node $\mathbf{X}_k$ by requiring

$$\frac{\partial \mathbf{X}_k}{\partial t} = \mathbf{u}(\mathbf{X}_k, t) \tag{2.159}$$

Since the immersed body's surface is discretized into set of points/nodes, the force transfer is written as

$$f_b = \sum_k \mathbf{F}_k(t) \delta \left(|\mathbf{x} - \mathbf{X}_k| \right) \tag{2.160}$$

However as the surface nodes will generally not coincide with the fluid mesh/grid points thus the effect of the nodes is generally spread out smoothly over the local grid points via a smooth distribution function. Moreover, the fluid density ρ, velocity $\mathbf{u}$ and stress σ need to be interpolated to the IB nodes. As explained in [110], an interpolation weight $\xi_{i\alpha} = \phi_i(x_\alpha)\phi_i(y_\alpha)\phi_i(z_\alpha)$ is assigned to each surface node located at (x_i, y_i, z_i) and nearby fluid mesh sites labelled by α located at $(x_\alpha, y_\alpha, z_\alpha)$. The interpolation weights satisfy

$$\sum_i \xi_{i\alpha} = 1 \tag{2.161}$$

and smoothly range over the interval $[0, 1]$ and are computed based on the distance between the fluid mesh sites and the surface node. These weights are then used to perform a weighted sum of different quantities such as fluid density, velocity at the nearby fluid mesh sites to obtain an interpolated value at the surface node. Based on this interpolation, any force applied by the immersed object on the fluid can, using Newton's third law be directly applied back to the body weighted by $\xi_{i\alpha}$.

Now to smoothly spread the influence of a node onto nearby lattice mesh sites, the sharp Dirac delta function used in (2.160) is typically replaced by a smooth approximation. A 4-point approximation of the delta function providing a 64 point fluid mesh support is typically used in simulations. The grid weights are then given by

$$\phi_i \left(r_\alpha \right) = \begin{cases} \frac{1}{8} \left(3 - 2\Delta r + \sqrt{1 + 4\Delta r - 4\Delta r^2} \right), 0 < \Delta r < 1 \\ \frac{1}{8} \left(5 - 2\Delta r - \sqrt{-7 + 12\Delta r - 4\Delta r^2} \right), 1 < \Delta r < 2 \\ 0, \qquad 2 < \Delta r \end{cases} \tag{2.162}$$

where r_α is the location of the fluid grid point and $\Delta r = \left(r_\alpha - r_i \right) / \Delta x$ is the distance between the i^{th} surface node positioned at r_i and the fluid mesh point at r_α, scaled by the

lattice spacing Δx. This method is also commonly referred to as the Peskin (P) stencil and is commonly used in immersed boundary methods.

Now, based on this description each surface node i affects the four nearest neighbour in the respective lattice mesh, amounting to a total of $n = 4^d$ affected mesh sites in d dimensions. In the Peskin stencil case, this implies the weight of the i^{th} surface node on the j^{th} lattice site can be determined by

$$\xi_{ij}^{P} = \phi\left(\frac{x_{ij}}{\Delta x}\right)\phi\left(\frac{y_{ij}}{\Delta x}\right)\phi\left(\frac{z_{ij}}{\Delta x}\right) \tag{2.163}$$

where (x_{ij}, y_{ij}, z_{ij}) is the displacement vector from the j^{th} fluid mesh site to the i^{th} surface node on the particle. The set ξ_{ij} is commonly referred to as a *stencil* and has the property that for each surface node

$$\sum_{j=1}^{n} \xi_{ij} = 1 \tag{2.164}$$

2.2.9 Velocity coupling

As mentioned in the earlier section, the overall idea in an immersed body scheme is solve a modified form of the Navier-Stokes equation where the presence of an immersed body and the fluid boundary conditions on its surface is captured via a forcing term, f_b (2.160). Given that the immersed body's surface is discretized into a set of surface nodes, the forcing term essentially becomes localized over the positions of the surface nodes.

As described in [110], consider the case of a sphere of radius a moving slowly through an infinite medium with a velocity $\mathbf{u}_b$. Assuming *no-slip* boundary conditions at its surface and the background fluid velocity is $\mathbf{U}$, the fluid drag force experienced by the sphere is given by *Stokes Law* as

$$\mathbf{F}_d = -6\pi\eta a\mathbf{v} \tag{2.165}$$

where $\mathbf{v} = \mathbf{U} - \mathbf{u}_b$ and holds true as long as $v = \|\mathbf{v}\|$ is relatively small. Moreover, for a sphere in shear flow when kept from rotating experiences a drag torque described by

$$\mathbf{T}_S = 4\pi\eta a^3 s_0 \hat{\mathbf{w}} \tag{2.166}$$

where s_0 is the shear rate and $\hat{\mathbf{w}}$ is the unit normal to the shear plane. These expressions describe the *Stokes* drag that immersed body experiences when moving through a fluid and can be used to verify the accuracy of numerical implementations as described in the subsequent method sections.

Based on this idea where the fluid drag force acting on a body is proportional to its relative velocity to the fluid, a local force coupling between the surface nodes and the fluid mesh can be written as [115]

$$\mathbf{F} = \pm\lambda\gamma\left(\mathbf{v} - \mathbf{u}\right) \tag{2.167}$$

In equation 2.167, $\mathbf{u}$ is the local fluid velocity near the nodes and is not the same as $\mathbf{U}$ and λ is the density of the nodes covering the immersed body's surface. Because of this

the *coupling* factor γ bears no similarity to the *Stokes* drag i.e. $6\pi\eta a$ and its value must be calibrated accordingly. The positive/negative sign indicates whether the force exerted on the immersed body via the fluid or vice verse respectively.

As demonstrated in [115], solving Navier-Stokes equations with this sort of coupling, (called the *Brinkman equations*) it is possible to show that the drag force and torque felt by a immersed body, for large γ is

$$\begin{aligned} \frac{F}{F_S} &= \frac{2\beta^2}{2\beta^2+9} \\ \frac{F}{T_S} &= \frac{\beta^2}{\beta^2+9} \end{aligned} \tag{2.168}$$

where $\beta = \sqrt{\frac{\gamma\lambda}{\eta}}$. From equations 2.168 it can be seen that as $\gamma \to \infty$

$$\frac{F}{F_S} \to 1 - \frac{9}{2}\frac{1}{\beta^2} \tag{2.169}$$

This indicates that equations 2.168 approach *Stokes* equations as $1/\gamma$ as $\gamma \to \infty$.

Now considering, that the particles immersed in the fluid are discretized using a set of *surface nodes* and given the appropriate stencil used, the local forces at each fluid mesh site j affect the i^{th} surface node by

$$\boldsymbol{F}_{ij} = \gamma\xi_{ij}\left(\boldsymbol{v}_i - \boldsymbol{u}_i^{(I)}\right) \tag{2.170}$$

where $\boldsymbol{v}_i = \boldsymbol{v} + \boldsymbol{\omega}\,\mathrm{x}\,\boldsymbol{r}_i$ is the velocity of the i^{th} surface node located at $\boldsymbol{r}_i$ from the particle's center of mass and $\boldsymbol{\omega}$ is the angular velocity of the solid. Moreover, in equation 2.170, $\boldsymbol{u}_i^{(I)}$ is the *interpolated* fluid velocity to the location of the surface node and is obtained as follows using the stencil weights ξ_{ij} and the fluid velocity at the actual mesh site i.e. $\boldsymbol{x}_j$

$$\boldsymbol{u}_i^{(I)} = \sum_{j=1}^{n} \xi_{ij}\boldsymbol{u}(\boldsymbol{x}_j) \tag{2.171}$$

Using the interpolated velocity, the net force acting on the i^{th} surface node due to the influence of all the $n = 4^d$ Peskin stencil nodes can be calculated as

$$\boldsymbol{F}_i = \sum_{j=1}^{n} \boldsymbol{F}_{ij} = \left(\boldsymbol{v}_i - \boldsymbol{u}_i^{(I)}\right)\gamma \tag{2.172}$$

Assuming that the particle is discritized using N_v surface nodes, the total fluid force acting on the j^{th} fluid lattice site is them simply a sum of equation 2.172 for all the nodes i.e.

$$\boldsymbol{F}_j = \sum_{i=1}^{N_v} \boldsymbol{F}_{ij} \tag{2.173}$$

This then gives us a three dimensional mesh $\boldsymbol{F}_j = \boldsymbol{F}(\boldsymbol{x}_j)$ of local forces on the fluid which goes equation 2.149 through 2.147. From here onwards, one can compute the local

forces, $\boldsymbol{F}_i$ and torques $\boldsymbol{T}_i$ acting on each surface node of the particle by summing over the affected fluid mesh sites i.e. over the stencil

$$\boldsymbol{F}_i = \sum_{j=1}^{n} \boldsymbol{F}_{ij}, \qquad \boldsymbol{T}_i = \boldsymbol{r}_i \,\mathrm{x}\, \boldsymbol{F}_i \tag{2.174}$$

and the net force and torque on the particle can be computed by simply summing equation 2.174 for all the surface nodes

$$\boldsymbol{F} = \sum_{i=1}^{N_v} \boldsymbol{F}_i \qquad \boldsymbol{T} = \sum_{i=1}^{N_v} \boldsymbol{T}_i \tag{2.175}$$

2.2.10 Hydrodynamic Radius of a sphere

As discussed in the immersed boundary section, to couple rigid bodies to the fluid lattice, the surfaces are discretized using a mesh of points. For instance, a rigid spherical particle can be represented as a *fullerene* as shown in figure 2.12

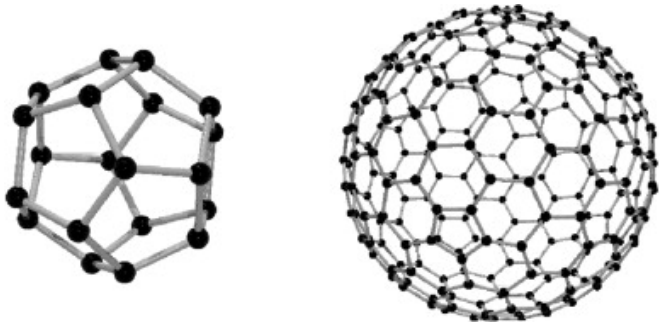

Figure 2.12: Illustration of discretizing the surface of a sphere using *fullerenes* with different surface node densities.

In order to reduce the surface discretization effects and to achieve sufficient surface node density, the spacing between the surface nodes is recommended to be less than the lattice spacing, Δx. Using the method described above, as the rigid particles move through the fluid, the effect of the surface nodes is smoothed out over several lattice sites via the 4-point Dirac delta approximation as described by equation (2.162). Now given that the influence of a surface node is spread out over multiple lattice sites, the question of what is the *hydrodynamic radius*, a_h of the particle become quite relevant. Since the surface nodes of the immersed sphere interact with several neighbouring lattice sites, the effective size of the particle as seen by the fluid is expected to different from its actual size. Now in order to require the LB simulations to match physical results, different LB schemes need to yield the same measure of the particle's hydrodynamic radius.

The hydrodynamic radius of a sphere, a_h can be measured via several methods such as measuring the drag force acting on a sphere moving through a fluid, hydrodynamic interactions between multiple particle or measure the hydrodynamic torque on the same. In fact, any measurement that is sensitive to the particle's size can be used as a measure

for its hydrodynamics radius, a_h. In essence, two different measures of the hydrodynamic radius of the particle i.e. a_h, a'_h need to agree with each other within a lattice spacing i.e. $|a_h - a'_h| < \Delta x$. In this work we compute the hydrodynamic radius of the spherical particle using two different approaches. The first one being by computing the drag force acting on a sphere moving with velocity $\boldsymbol{v}$ through the fluid as given by equation (2.165) and; the second being computing the net drag torque acting on a sphere in steady shear flow which is given by equation (2.166). We refer to these two different measures of the hydrodynamic radii as $a_{h,F}$ and $a_{h,T}$ respectively and can be easily solved from using equations (2.165) and (2.166). The hydrodynamic radius of a sphere moving with uniform velocity, $\boldsymbol{U}$ in the y-direction can be expressed in terms of the drag force as $a_{h,F} = F_y/6\pi\eta U$ and the same can be obtained by computing the net torque on it when it is held stationary in a uniform shear flow at rate s_0 via $a_{h,T} = \left[\frac{T_z}{4\pi\eta s_0}\right]^{1/3}$.

2.2.10.1 Calibration

In methods where frictional type coupling between the surface nodes and the fluid lattice sites is used to implement the fluid particle interactions as shown in equation (2.160), the coupling constant, γ needs to be calibrated properly in order to ensure consistency between the different measures of hydrodynamic radius of a particle, a_h. Now in order to calibrate the coupling constant γ one can carry out simulations for each of the two cases i.e. (a) sphere moving in a fluid with uniform velocity U to compute the fluid drag force F_y and (b) measure the total torque, T_z on a stationary sphere in uniform shear flow for different values of γ. Ollilia et al. in [120] have carried out this analysis in detail and have presented consistent results for the two cases. As an illustration we present our calibration results for a sphere of radius $a = 2.8\Delta x$ in figure 2.13. Further details about our analysis are discussed later in the implementations sections.

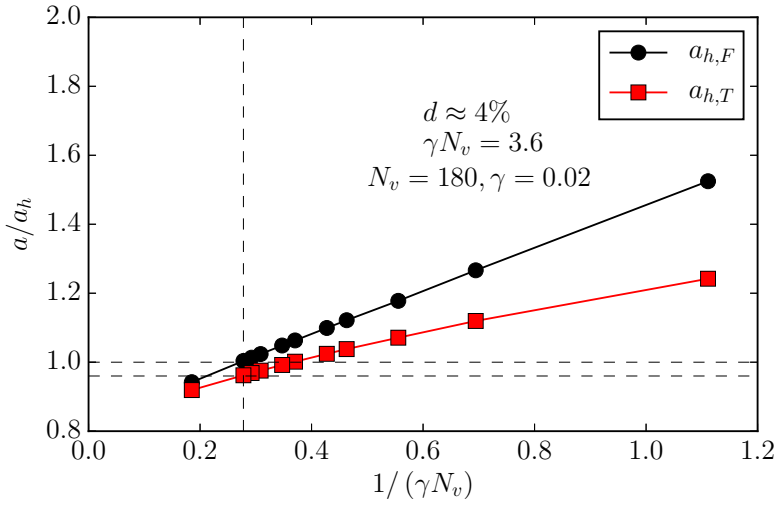

Figure 2.13: Hydrodynamic radius of a sphere with nodes placed at radius, $a = 1.4\,\text{nm}$ obtained from drag force, $a_{h,F}$ and torque, $a_{h,T}$ simulations

From figure 2.13, we note that hydrodynamic radius calculated using the two different approaches results in very different values for a_h expect for the case where γ, the coupling constant is set to a large values. Now, in practice setting γ to infinity is not feasible, so the relevant question is simply how large does γ need to be for the torque and drag force experiments to yield consistent results in imposing the no-slip boundary condition on the particle's surface. We can see that for all values of γ beyond 0.02, the agreement between hydrodynamic radii of the sphere obtained from the two different approaches is within 4% and continues to improve for values beyond that. It is also worth noting that once the system is calibrated with a sphere of any given size what Ollila et al. [120] one can use the calibration information for spheres of different sizes given a key quantity namely the ration of γ to the area per node, A_n is kept constant i.e.

$$\text{constant} = \frac{\gamma}{A_n} = \frac{\gamma N_v}{4\pi a^2}. \tag{2.176}$$

With this relationship, if one calibrates γ for a sphere of radius a and then wants to scale the sphere to size $2a$, then γ must be scaled by 4. Lastly, as mentioned earlier to calibrate the coupling constant, any measure sensitive to the particle's size can be used, Ollila et al. [120] also computed the hydrodynamic radius of a sphere by measuring its diffusion constant in the LB fluid and found that as long as γ is calibrated properly and different measurements of the hydrodynamic radius are in good agreement with each other, the LB fluid also acts as a good heat bath for all the particles immersed in it and the diffusion observed is as per the *fluctuation-dissipation* theorem.

Chapter 3

Polymer margination in shear flows

In this section, we present our work and results on the topic of polymer margination in shear flow. As mentioned earlier in the introductory sections, in this work we primarily investigate the effects of monomer size on a polymer chain's margination tendencies in shear flow. We address this issue of the chain's lateral migration via hybrid LBMD (Lattice-Boltzmann-Molecular Dynamics) simulations. We study the margination tendencies of single polymer chains of length N in Couette flow over a range of shear rates $\dot{\gamma}$ and in particular investigate the effect of monomer size, a on the chain's overall migration. We observe that polymer chains with smaller monomers show poor migration tendencies as compared to their larger counterpart. Furthermore unlike Poiseuille flows, the shear rate is constant throughout the entire channel in Couette flows indicating no real benefit for single monomers to marginate cross-stream [148]. Based on these, we believe our observations in this work are therefore primarily a chain effect rather effects at a single monomer level.

We present our results in the next couple sections starting with our simulation model using LAMMPS in section (3.0.1). Following this section we elaborate on our procedure on calibrating the fluid particle coupling constant necessary to enforce the *no-slip* boundary condition between the two. In the same section we also report our results on the effects of improper calibration and see how it effects the thermalization of particles immersed within the fluid. In the subsequent sections (3.0.3 - 3.0.5) we present the results of our work along with discussions pertaining to our observations.

3.0.1 Simulation Model

In this work, using hybrid LBMD simulations we investigated the margination properties of individual polymer chains in Couette flow. Moreover we studied the effect of monomer size, a on the margination tendencies of the chains in flow. All our simulations were carried out using LAMMPS [130, 176] and we used a D3Q15 Lattice-Boltzmann (LB) model to accurately incorporate hydrodynamic interactions (particle/particle, particle/no-slip surface) in our system. We use nano-units in LAMMPS, where distances are in nm, time in ns, and mass in ag. In our simulations the LB fluid mediates the hydrodynamic interactions as well as acts as a heat bath for the particles immersed in it. Implementing thermal fluctuations in the LB fluid so that it reproduces the fluctuation-dissipation

correctly has been described in detail in [1]. Details pertaining to our implementation of this framework can be found in earlier chapters as well in [117, 120]. This model and implementation are now well-tested in many examples [4,98,116,181], including polymers in solution [117–119].

We used a lattice spacing of $dx = 0.5\,\mathrm{nm}$ and updated the entire fluid lattice every time step. Depending on the chain length i.e. $N = 16, 32$ the simulation box dimensions were set to $(32, 60, 32), (60, 100, 32), \mathrm{nm}$ respectively and a time step of $\Delta t = 30\,\mathrm{fs}$ was used. Every simulation carried out was at least a minimum of 300 ns in duration. Following Ollila et al. [117,118], in order to speed up the diffusive dynamics, the density of our fluid was set to 1/60 that of water at $T = 300\mathrm{K}$ and we scaled its kinematic viscosity by a factor of 1.4. To study the effect of monomer size we considered two different radii values, $a = 0.7$ and $1.4\,\mathrm{nm}$ and kept the same radii for all monomers in a given chain. All the monomers were taken to be neutrally buoyant in the LB fluid. In LB simulations mesh effects can be a major source of error if not accounted for properly. Following [120], in our simulations each monomer was comprised of two types of MD atoms (a) a central atom and (b) a spherical shell of N_v nodes. This configuration of atoms in a monomer is depicted in figure (3.1).

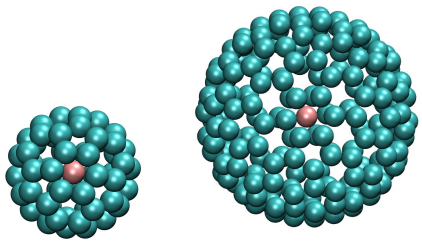

Figure 3.1: (left) Composite monomer of radius $a = 0.7\,\mathrm{nm}$ with $N_v = 60$ (right) Composite monomer of radius $a = 1.4\,\mathrm{nm}$ with $N_v = 180$.

The benefit of using such an approach is that it gives each monomer a hydrodynamic size independent of the fluid lattice spacing. All bonded/non-bonded interactions are mediated by the central atoms whereas the spherical shell nodes interact only with the LB fluid and mediate the hydrodynamic interactions. In our simulations every monomer was treated as a rigid body during integration. We choose the number of surface nodes, N_v such that the surface area per node for a monomer of radius a is always smaller than dx^2 i.e. $4\pi a^2/N_v < dx^2$. This rule of thumb ensures that the surface is sufficiently discretized and there are no big gaps in the monomer. Lastly monomers are connected using the FENE bond style,

$$U_b = -\frac{1}{2}\,K\,R_0^2\,\log\left(1 - \frac{r^2}{R_0^2}\right) + 4\epsilon\left(\left(\frac{\sigma}{r}\right)^{12} - \left(\frac{\sigma}{r}\right)^{6} + 1\right), \tag{3.1}$$

with parameters $K = 60\,\mathrm{ag/nm^2}$, $\epsilon = k_B T$, $\sigma_b = 1.5\,\mathrm{nm}\,(a = 0.7\,\mathrm{nm}), 2.67\,\mathrm{nm}\,(a = 1.4\,\mathrm{nm})$ and $R_0 = 1.5\,\sigma_\mathrm{b}$. We used periodic boundary conditions in the x and y directions

and fixed boundary conditions in the z direction. In all cases the system size is more than 2.5 times the equilibrium radius of gyration R_g of the chain so the chain is not compressed due to the slit geometry of the system. To mimic interactions with an impenetrable atomic surface we placed two layers of atoms in the tightly packed FCC 111 geometry with a lattice spacing of 1.0 nm at the $z = 0$ boundary of the simulation domain as depicted in figure (3.2) We implemented a $12-6$ Lennard-Jones (LJ) potential

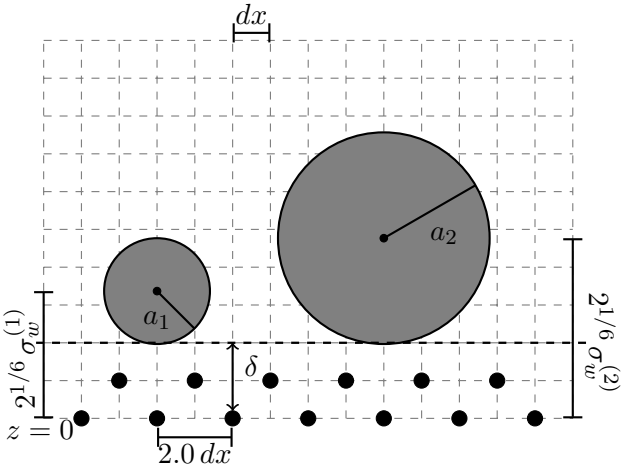

Figure 3.2: Schematic of the wall atom geometry used in our simulations along with the LB lattice and surface interaction length scales. Here a_1 and a_2 are the radii of the spheres respectively. δ is spacing between the bottom of the sphere and the $z = 0$ simulation domain boundary. σ_w is the surface potential interaction length scale.

of strength ϵ_w with interaction length scale σ_w between the central and wall atoms in our simulations. The monomer shell atoms and the fluid lattice sites were coupled via the method outlined in [120] to establish interactions between the two. Following [118] and requiring that the gap size δ remains the same for different sized monomers when they are at the LJ surface potential minimum i.e. a distance of $2^{1/6}\sigma_w$ from the bottom surface ($z = 0$) we set our LJ interaction length scale to $\sigma = 1.5$ nm for the $a = 0.7$ nm case and $\sigma_w = 2.12$ nm for the $a = 1.4$ nm case. Making the gap size, δ the same for both monomers meant that the lubrication forces between the wall and the particles depended only on the monomer radius and not on the differences between the distance from the wall, which in principle would be the same in absence of hydrodynamics. Given the FCC geometry of the surface and the different interaction length scales σ_w in our simulations, an individual monomer can interact with a different number of surface atoms depending on its size. To ensure we are comparing otherwise equivalent systems, the surface potential interaction strength ϵ_w was tuned so that the adsorption tendencies of the $a = 0.7$ and 1.4 nm chains were similar in equilibrium. Setting the surface interaction strength ϵ_w to 0.24 in the 0.7 nm case and $\epsilon_w = 0.15$ in the 1.4 nm case resulted in good agreement in the respective equilibrium adsorption tendencies, as demonstrated below. The surface interaction cutoff was placed at $r_c = 2.5\,\sigma_w$ for the both cases. To verify

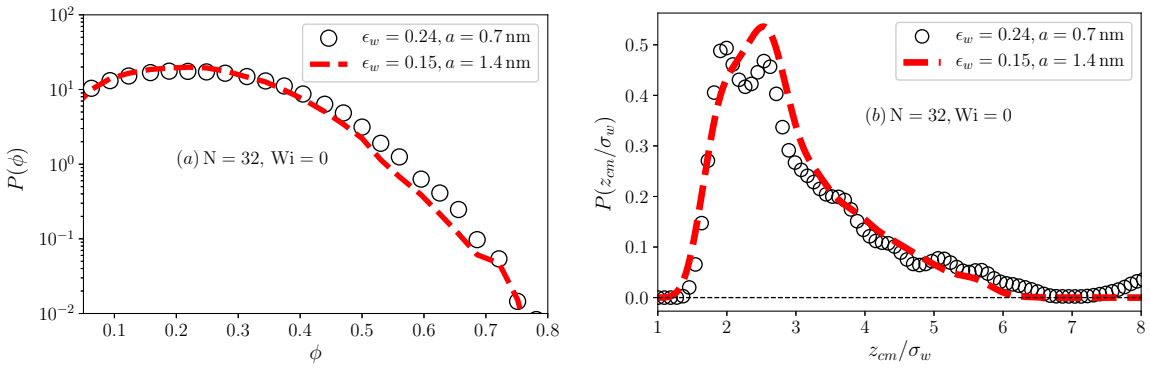

Figure 3.3: (a) Probability distribution of the average number of monomers within a distance of $d_c = (26/7)^{1/6}\,\sigma_w$ from the surface, ϕ for Wi = 0. (b) Probability distribution of the chain's center of mass normal to the surface z_c scaled by the interaction length scale, σ_w. The fluctuations in the curves are due to statistical errors in the measurements.

the equivalence of the interaction with the wall, in figure (3.3) we plot the distribution of two parameters that characterize the equilibrium adsorption tendencies of a single $N = 32$ monomer long chain. In figure (3.3a) we consider the distribution of ϕ which simply measures the fraction of monomers within a distance d_c from the surface. We chose the inflection point of the LJ potential as a suitable distance for this measure i.e. $d_c = (26/7)^{1/6}\,\sigma_w$. For the aforementioned values of the interaction potential strength ϵ_w from this figure we can note that the agreement between the two ϕ distributions is very good. As a second measure of adsorption in equilibrium, in figure (3.3b) we plot the probability distribution of the chain's center of mass normal to the surface scaled by the respective interaction length scale, σ_w. Even though the data is a bit noisy in this figure we can see that the agreement between the two distributions is very good and the adsorption behavior for the chains in equilibrium is essentially identical.

We carried out simulations over a range of shear rates, $\dot{\gamma}(\mathrm{ns}^{-1}) = 0, 0.2, 1.0, 2.0$. As a dimensionless measure of the shear rate, we scaled these values to their respective **Weissenberg Number**, Wi by simply multiplying them by the relaxation time of the principal Rouse mode of the chains. In the Zimm model, this is expected to follow [131]

$$\tau_1 \sim \frac{\zeta\, N^{z\nu}\, b^2}{3\,\pi^2\, k_B T}. \tag{3.2}$$

Here ζ is the frictional coefficient for a single monomer in the solvent i.e. $6\pi\eta\, a$, N is the number of monomers comprising the chain, b is the average bond length between the monomers, and $z\nu \approx 1.74$ [117]. For better ensemble averaging we did at least five independent runs at each value of Wi. A Couette flow profile was generated by translating the top wall of our simulation domain parallel to the bottom surface in the positive y direction. This generated, on average a uniform shear flow profile in the channel. Lastly in all the runs the polymers started off near the bottom surface however all the results discussed in the following sections were computed after an equilibration period of at least 10^6 steps. A sample starting configuration of a chain is depicted in figure 3.4

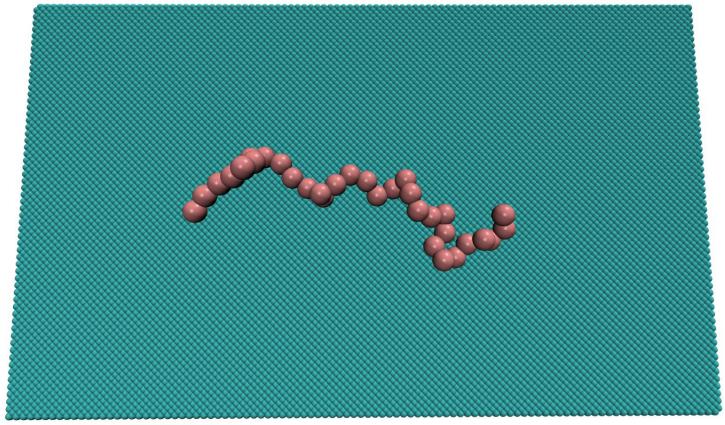

Figure 3.4: Sample of an initial conformation of the polymer on the surface. Note that for better depiction of the chain's conformation without overlapping of atoms we omit drawing the spherical shell surrounding each monomer.

3.0.2 Monomer/Fluid coupling

As the monomers move through the fluid an interaction between the two must occur. Stokes law dictates that the fluid drag force acting on a sphere is proportional to its velocity through the medium. In our LB algorithm we exploit this fact to couple the fluid and particles together by making the fluid drag force acting on a particle node proportional to its velocity relative to that of the fluid velocity interpolated to its location i.e.

$$\mathbf{F}_i = -\gamma \left(\mathbf{v}_i - \mathbf{v}_f \right). \tag{3.3}$$

However its important to note that proportionality constant, γ in (3.3) is not the Stokes drag coefficient $6\pi\eta a$ in general and has to be calibrated properly to ensure proper dynamics, thermalization and consistency between different measures of the hydrodynamic radii. The calibration procedure for the coupling parameter, γ is discussed in great detail in [120] and we follow it in this work to consistently set a value for γ. In figure 3.5 we show the results from our γ calibration runs and agreement between the different hydrodynamic radii measurements.

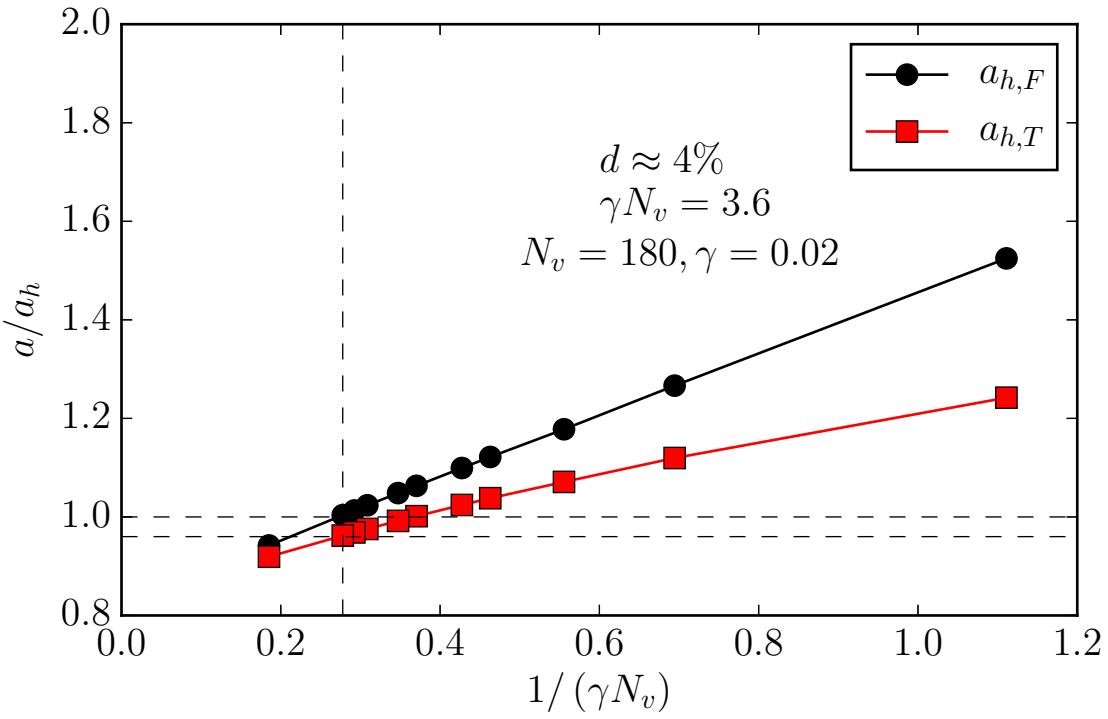

Figure 3.5: Hydrodynamic radius of a sphere with nodes placed at radius, $a = 1.4\,\text{nm}$ obtained from drag force, $a_{h,F}$ and torque, $a_{h,T}$ simulations

In principle the value of γ should be infinite in order to ensure a no-slip boundary condition on the particle's surface, however since equation (3.3) represents a stiff term, large values of γ will likely render the numerical integration of the system unstable. Thus γ must be large enough so that the hydrodynamic radius of the sphere obtained by say measuring the drag force acting on it under uniform translation through the fluid, $a_{h,F}$ or by computing the torque acting on it when held stationary in shear flow, $a_{h,T}$ must be in good agreement with each other. In our work we saw good agreement between $a_{h,F}$ and $a_{h,T}$ for $\gamma > 0.02$ in both cases i.e. $a = 0.7, 1.4\,\text{nm}$. During the calibration runs we noted that setting the value of $\gamma > 0.11$ resulted in numerically unstable runs in the $a = 0.7\,\text{nm}$ case, however we were able to push γ to 0.15 in the $a = 1.4\,\text{nm}$ case. Both of these values are sufficiently larger than the lower bound of 0.02 and over these ranges good agreement between the different measures of the hydrodynamic radii was observed. Calibrating the coupling parameter γ this way also ensured that the MD particles feel the right fluid temperature and are thermostatted properly during simulations.

3.0.2.1 Single monomer thermalization

To address the importance of proper γ calibration, we carried out several simulations of a single monomer $a = 1.4$ nm in our fluid near the surface. We carry out all these simulations in the absence of any shear flow i.e. $\text{Wi} = 0$ and start the sphere out close to

the surface in all cases. Since we are primarily interested in the equilibrium adsorption behavior of a single monomer, we run the simulations with exactly the same parameters as described earlier for an appropriate duration. Moreover, in order to illustrate the effects of improper γ calibration, for these runs we initially used a value far smaller than $\gamma < 0.02$. As per figure 3.5, we can see that over this range, the agreement between the different measures of the hydrodynamic radius is quite poor. Thus in principle, one would expect the *no-slip* boundary condition on the monomer's surface to be poorly implemented and improper fluid temperature reproduction. Now, in order to assess the accuracy of the results from our LB runs, we carry out Langevin (LNGV) simulations of the exact same system near the surface. Given that all simulations are being done in equilibrium, the results from both are expected to be the same given a properly calibrated γ. In both thermostats a fluid temperature of $300K$ was set in all simulations. In Langevin simulations, the heat bath is artificial in the sense that the particle is kicked around due to the addition of random, delta correlated forces that obey the *fluctuation-dissipation* theorem. There is not hydrodynamic interactions present in Langevin simulations but in equilibrium i.e. $\dot{\gamma} = 0$ those interactions should in principle have no effect on the particle's distribution. To ensure that we have properly calibrated γ for our LB simulations, we compare the results we obtain for a single monomer near the surface in a LB thermostat to the ones obtained via a purely Langevin simulation. A good agreement between the two would give us confidence in our calibration and also go to show that the monomer is feeling the correct fluid temperature as set in the simulation.

We begin by looking at the probability distributions of the monomer's separation from the surface potential minimum i.e. $\Delta z = z - z_m$ where $z_m \approx= 2.55\,\text{nm}$ for the different interaction strengths ϵ_w in both the thermostats i.e. LB/LNGV. From figures in 3.6 we note that, in the LB case the sphere tends to remain more localized over smaller values of Δz. This, in principle, means that the diffusion of the monomer is effectively reduced in the z direction in comparison to the Langevin thermostat. In figure (3.6 f), we plot the mean height above the surface potential minimum the monomer attains over the course of the simulation as a function of the surface interaction strength ϵ_w. We note that difference in the mean height and z_m in both cases diminishes with increasing ϵ_w. This behaviour can simply be attributed to the fact that as the interaction strength increases, regardless of the thermostat and γ calibration, the monomer becomes increasing confined in the surface potential and remains fairly close to the potential minimum for the duration of the simulation in both cases.

The differences in the monomer height distributions is rather large for weaker interaction strengths ϵ_w. These figures go to show that in equilibrium i.e. in the absence of any shear flow, the sphere tends to remain more localized in the surface potential well in comparison to the Langevin case. This apparent ambiguity points to less than normal diffusion of the monomer in the LB thermostat and smaller diffusion coefficient. In order to quantify this further, in figure 3.7 we plot the average time over the course of a simulation the monomer spends confined within the surface potential. We record the value of this quantity ϕ as a boolean and set it to one each time the monomer's center of mass is between the potential minimum and potential cutoff. In figure 3.7, we plot the average ϕ as a function of the surface interaction strength in case of both thermostats and clearly note that for smaller values of the ϵ_w the difference in adsorption is greater

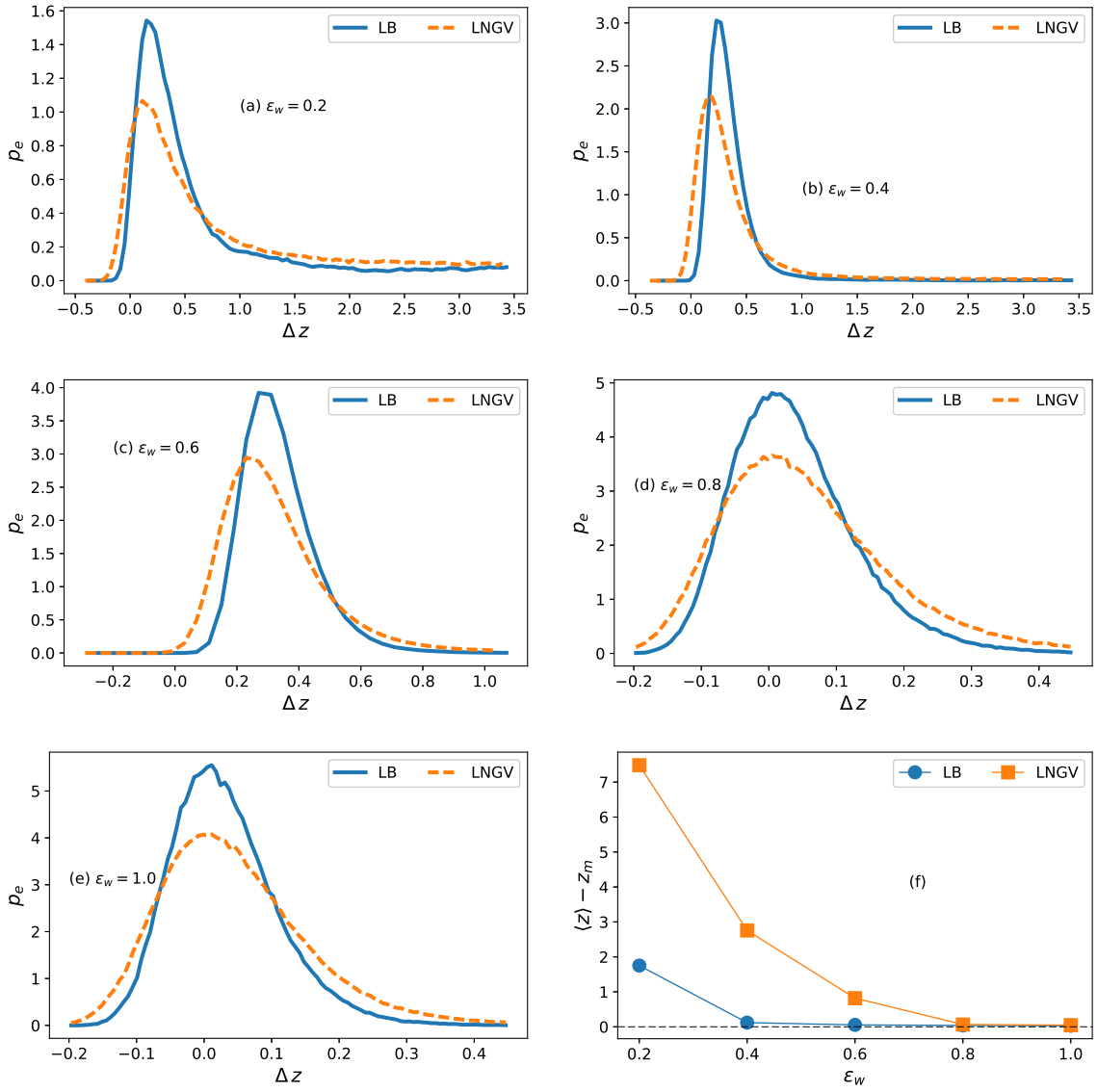

Figure 3.6: (a-e) Probability distribution of the monomer's elevation relative to the surface potential minimum, z_m for different interaction strengths, ϵ_w. (f) Mean elevation, $\langle \Delta z \rangle$ above the surface potential minimum as a function of the interaction strength ϵ_w. (blue) Lattice-Boltzmann thermostat (LB), (orange, dashed) Langevin (LNGV). For these runs γ was set to 0.01 which is below the value $\gamma = 0.02$ at which we begin to see good agreement between the different measures of the hydrodynamic radius of the monomer. $\gamma = 0.15$ gave us excellent agreement between the LB and LNGV runs and also resulted in stable numerical simulations.

between the two thermostats. This measure also indicates that the monomer tends to spend longer in the potential well i.e. near the surface and diffuses much less when the LB fluid thermostat is used with γ that is improperly calibrated.

As shown in [120], if γ is not calibrated properly, the diffusion coefficient of a sphere will not be as dictated by the Einstein's relation and indirectly results in the effective temperature of the fluid will being a lot lower than the target temperature. In some of our runs with poorly calibrated γ, we noticed that the fluid was around 20 K cooler than the desired target temperature of 300 K. The discrepancy between the actual fluid temperature and the target temperature can be described as a function of γ and the values can be computed from extensive LB simulations.

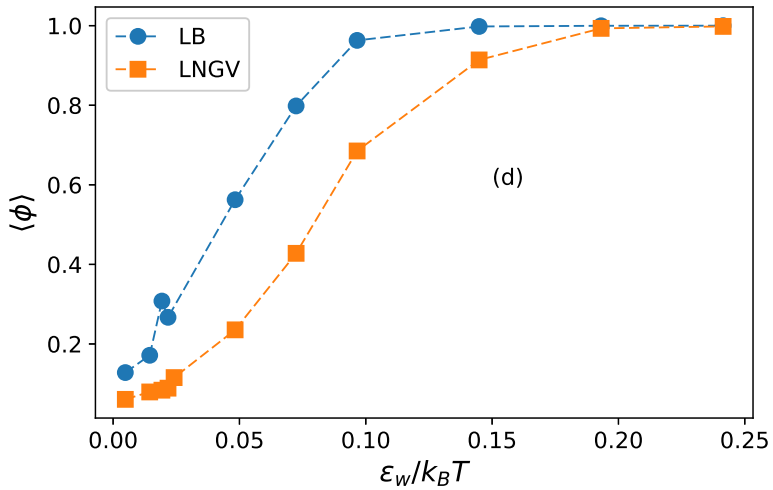

Figure 3.7: Fraction of net run time a sphere spends in the potential well, $\langle\phi\rangle$ for different interaction strengths, ϵ_w. (red circles) LB thermostat, (blue squares) Langevin thermostat

3.0.2.2 Boltzmann Distribution: Effective potential, U_e and Force, $\mathbf{F_z^e}$

Apart from looking at the distributions of the displacement of the monomer from the surface potential minimum and the mean surface adsorption $\langle\phi\rangle$, in this section we look at another way to quantify the effects of improper γ calibration by looking at the effective potential felt by the monomer as it moves around the fluid near the surface due to the effect of the different thermostats (LB/Langevin). Given that all the simulations here are carried out in the absence of any shear flow i.e. Wi = 0, one would expect the monomer's position in equilibrium be the same as postulated by the Boltzmann distribution i.e.

$$p_e(z) = A \exp\left(-\frac{U_e(z)}{k_BT}\right) \tag{3.4}$$

Following [25, 41, 153, 187] where the authors studied the effective forces acting on a sphere near a surface using Total Internal Reflection Microscopy (TIRM), we compute the

effective potential, U_e and forces acting on the sphere from the probability distributions of its elevations above the surface. We eliminate the normalization constant by dividing both sides of equation 3.4 by the probability of finding the sphere at some reference elevation, z'. From the resulting expression the effective potential can easily be identified as

$$U_e(z) - U_e(z') = k_B T \log\left(\frac{p_e(z')}{p_e(z)}\right) \tag{3.5}$$

It is to be noted that for sufficiently large number of position samples one can compute the potential by simply using the raw histogram counts since the probability density, $p_e(z)$ will be directly proportional to it. We choose the minimum of the surface potential, z_m as the reference height with respect to which $U_e(z)$ is evaluated. In terms of the raw histogram this simply entails that we use the counts in the bin that contains z_m.

In figure 3.8, we again plot the probability density of the sphere's elevation relative to the surface potential minimum i.e. $\Delta z = z_m \approx 2.55\,\text{nm}$ for different values of ϵ_w. It can be seen that regardless of the thermostat used (LB/Langevin (LNGV)) the distribution remains more or less uniform for weak interaction strengths ($\epsilon_w = 0.02, 0.08$), but peaks near $\Delta z = 0$ are more prominent in the LB thermostat case indicating longer than average confinement of the sphere near the surface. In figures (3.8 b, d), we plot the distributions for much higher values of ϵ_w in order to quantify any differences in the thermostats if the cases of strong monomer confinement near the surface. In the LB case, if properly calibrated γ was used and the simulations are run for sufficiently long duration, the difference between the LB and Langevin distributions should be negligible as both of them should reproduce equilibrium Boltzmann dynamics properly.

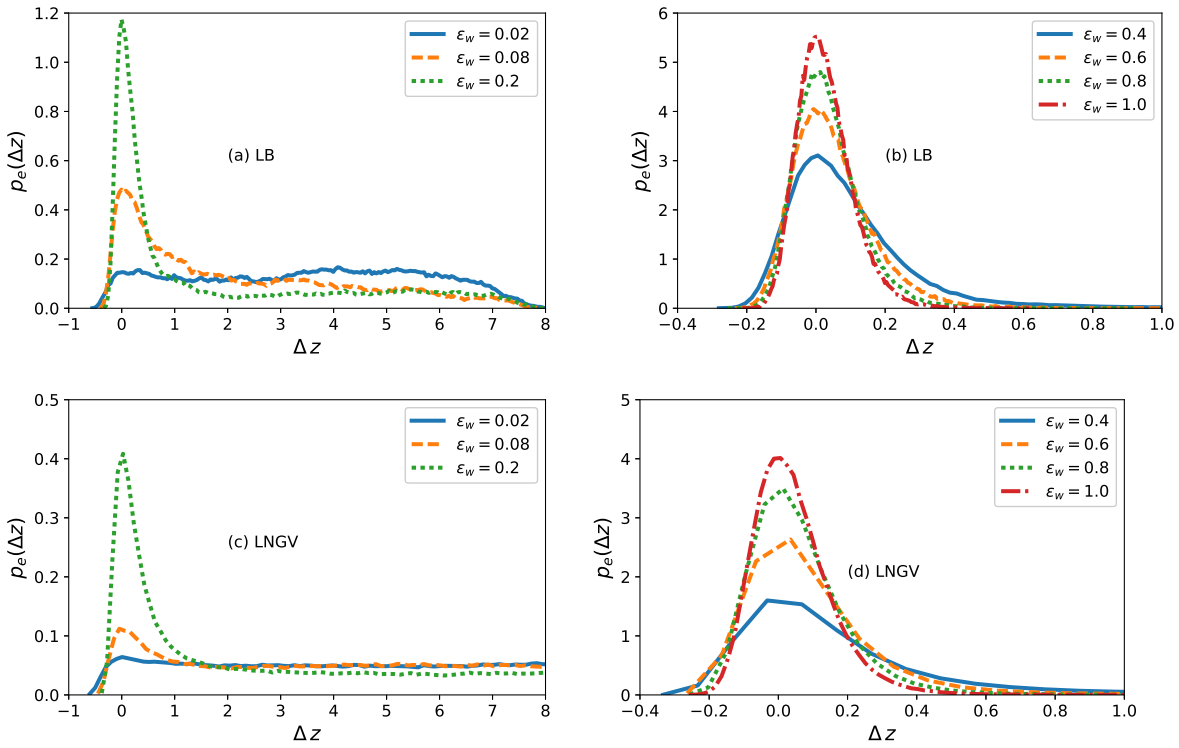

Figure 3.8: Probability densities of the sphere's elevation relative to the surface potential minimum, $z_m \approx 2.55\,\text{nm}$ in the different thermostats, (a,b) LB, (c,d) Langevin (LNGV). In figures (b) and (d) we plot the same metric but for a much stronger interactions strength i.e. $\epsilon_w = 0.4, 0.6, 0.8, 1.0$. Due to this in both cases we see range of Δz to be severely restricted since in both cases the monomer remains strongly confined within the surface potential

From figure 3.8, we note that there are significant differences between the LB and LNGV distributions even for the strong confinement cases i.e. $\epsilon_w = 0.4, 0.6, 0.8, 1.0$. Even though the monomer spends most of the simulation duration near the surface confined in the potential, from the distributions it is apparent that the confinement is much stronger when the LB thermostat is used. This result again goes to show the importance of properly calibrating γ when using the LB fluid as a heat bath for particles, since the fluid temperature cannot be properly reproduced when the *no-slip* boundary condition between the fluid and monomer surface is not properly implemented.

From the distributions we now derive the effective potential energy of the monomer as a function of its elevation from the surface in either of the thermostats. In the Langevin case since there is no explicit fluid the potential energy of the sphere is solely due to its interaction with the surface, thus the surface Lennard-Jones potential and the computed effective potential, U_e should be identical. In the LB fluid case however, due to improper γ calibration an additional nonphysical contribution from the fluid is to be expected.

In figure (3.9-3.13) we plot the effective potential derived from the monomer's elevation distribution show in figure 3.8 for the surface interaction strength $\epsilon_w = 0.2, 0.4, 0.6, 0.8, 1.0$ respectively. Here the red curves, U_e are the plots of the potential derived from the dis-

tributions via equation (3.5). The blue dashed curve is simply the 12-6 Lennard Jones potential evaluated at elevations from the surface. We shift this potential by subtracting its value at minimum i.e. $z = 2^{(1/6)}\sigma_w$ so that the potential becomes zero exactly at the minimum. Lastly the green dashed curve is the apparent difference between the effective potential computed by inverting the position distribution of the monomer and the true shifted 12-6 Lennard-Jones potential.

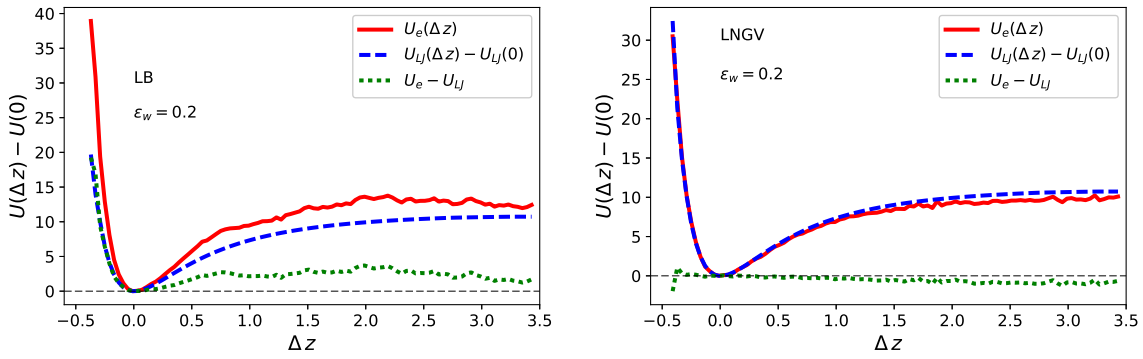

Figure 3.9: Effective potential derived from the probability distributions of the elevation of the monomer from the $z = 0$ surface for $\epsilon_w = 0.2$. (left) Effective potentials, U_e derived in the case of the LB thermostat (right) Potentials derived for the Langevin thermostat

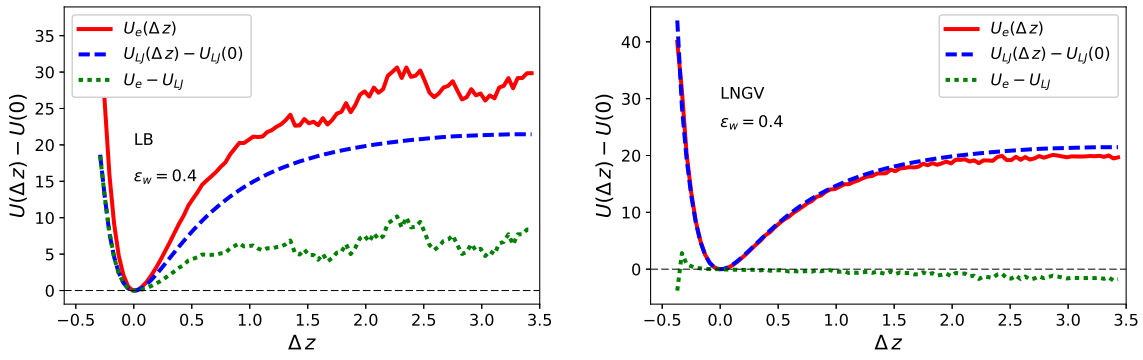

Figure 3.10: Effective potential derived from the probability distributions of the elevation of the monomer from $z = 0$ surface for $\epsilon_w = 0.4$. (left) LB thermostat (right) Langevin thermostat

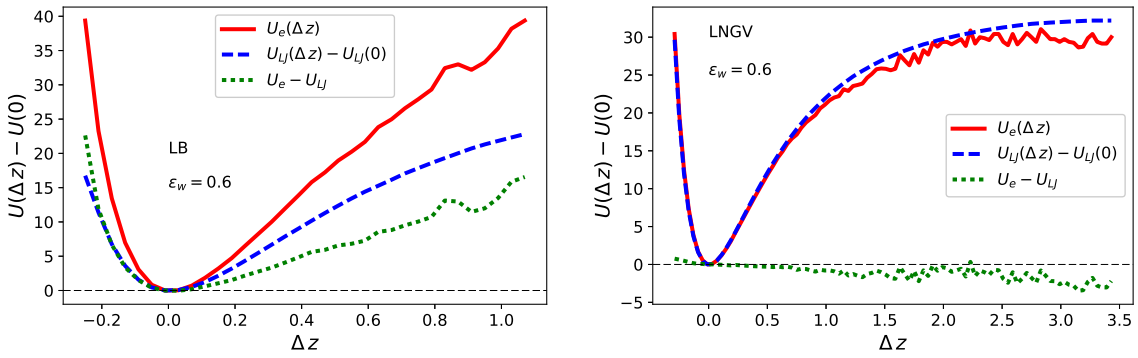

Figure 3.11: Effective potential derived from the probability distributions of the elevation of the monomer from $z = 0$ surface for $\epsilon_w = 0.6$. (left) LB thermostat (right) Langevin thermostat

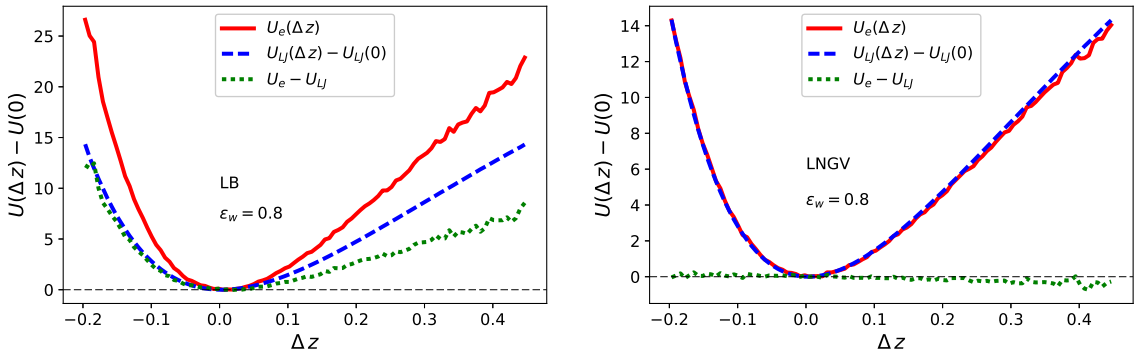

Figure 3.12: Effective potential derived from the probability distributions of the elevation of the monomer from $z = 0$ surface for $\epsilon_w = 0.8$. (left) LB thermostat (right) Langevin thermostat

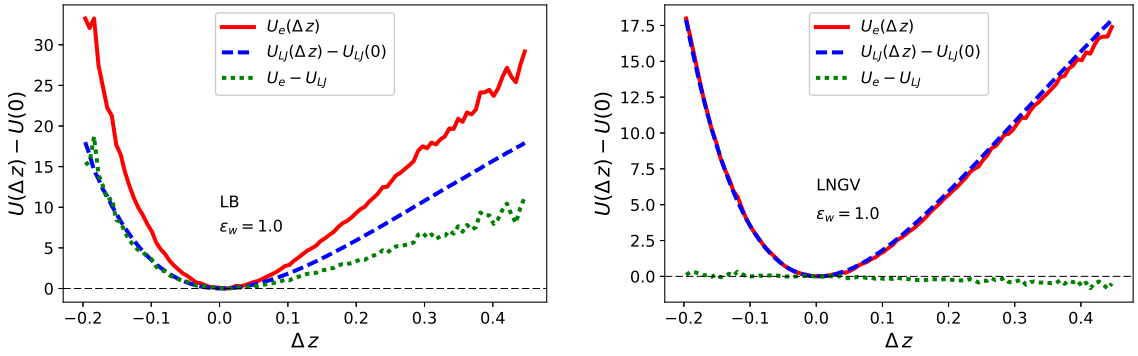

Figure 3.13: Effective potential derived from the probability distributions of the elevation of the monomer from $z = 0$ surface for $\epsilon_w = 1.0$. (left) LB thermostat (right) Langevin thermostat

From these figures, it is quite apparent that the derived potential in the LB case matches extremely poorly with the true Lennard-Jones surface potential when γ is not properly calibrated. In the Langevin thermostat case however the agreement between the two is quite good and both can be considered exact up to roundoff errors. Moreover, as pointed out earlier the discrepancy between the derived potential and true Lennard-Jones in the LB case persists even when the interaction strength is really strong i.e. $\epsilon_w = 1.0$. This means that despite the particle being strongly confined in the surface potential well its diffusive tendencies are reproduced extremely poorly and the heat bath fails to generate the correct fluid temperature.

In light of the above figures, we extend our analysis by deriving effective force felt by the monomer in the LB fluid that is poorly calibrated. To this end, we simply numerically differentiate the derived effective potential in the direction normal to the surface and plot the obtained values in figure 3.14. From the force profiles, we can clearly see that due to incorrect γ calibration, a *pseudo* residual force, ΔF_z appears to act on the monomer near the surface. Ideally, in the case when the calibration is done properly, the derived effective force, F_z^e and the Lennard-Jones force must be identical and the residual must vanish for all values of ϵ_w.

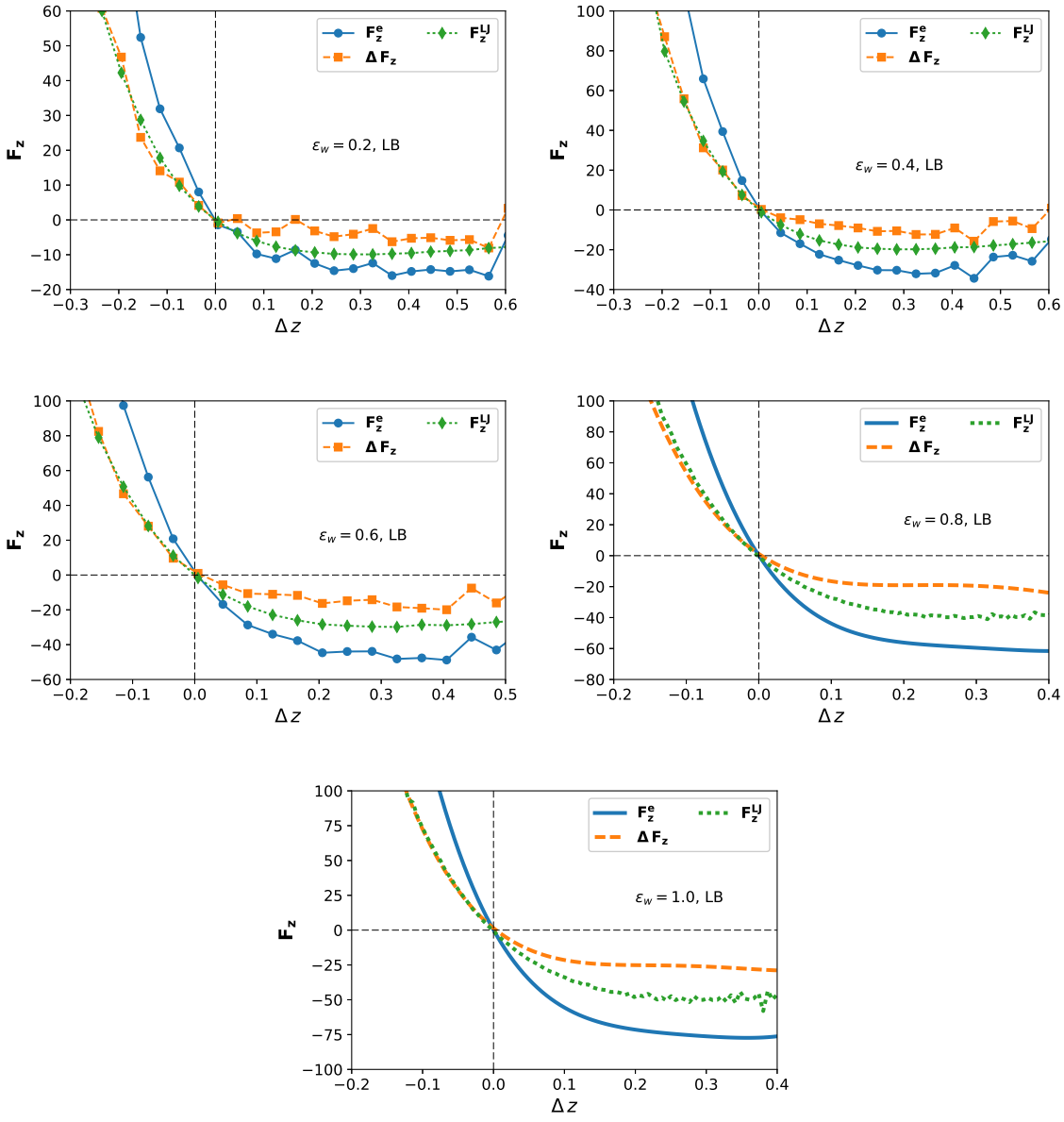

Figure 3.14: Effective force felt by the monomer normal to the surface in the LB thermostat for $\epsilon_w = 0.2, 0.4, 0.6 0.8, 1.0$. (blue) Effective force derived from U_e, (green) Standard Lennard-Jones force acting on the monomer normal to the surface (orange) Residual (pseudo) force acting on the monomer, computed as a difference between the Lennard-Jones force and the effective derived force.

3.0.2.3 Proper calibration

So far, in the above sections we thoroughly investigated the effects that one might see in the case when the LB fluid and particle coupling constant, γ is not calibrated properly. But as shown in [120], if one follows the proposed recipe of picking a γ large enough so that there is consistency between the different measures of the hydrodynamic radius of

a particle, then the LB fluid can be expected to act as a good heat bath for the particles immersed within it and the no-slip boundary condition on the particle's surface will also be well respected. To quantify the effects of a properly calibrated coupling constant i.e. γ we begin plot plotting the distribution of the monomer's elevation above the surface at $z = 0$ in figure 3.15. In all these simulations, we set $\gamma = 0.15$ to be far greater than the lower limit 0.02 as shown in figure 3.5. As mentioned in [120], we push to be the largest possible value, $\gamma = 0.15$ in our case, until our simulations become numerically unstable. From figure 3.15 we can clearly see the excellent agreement between the distributions obtained from the different thermostats i.e. LB and Langevin. Similar to figures 3.9 -

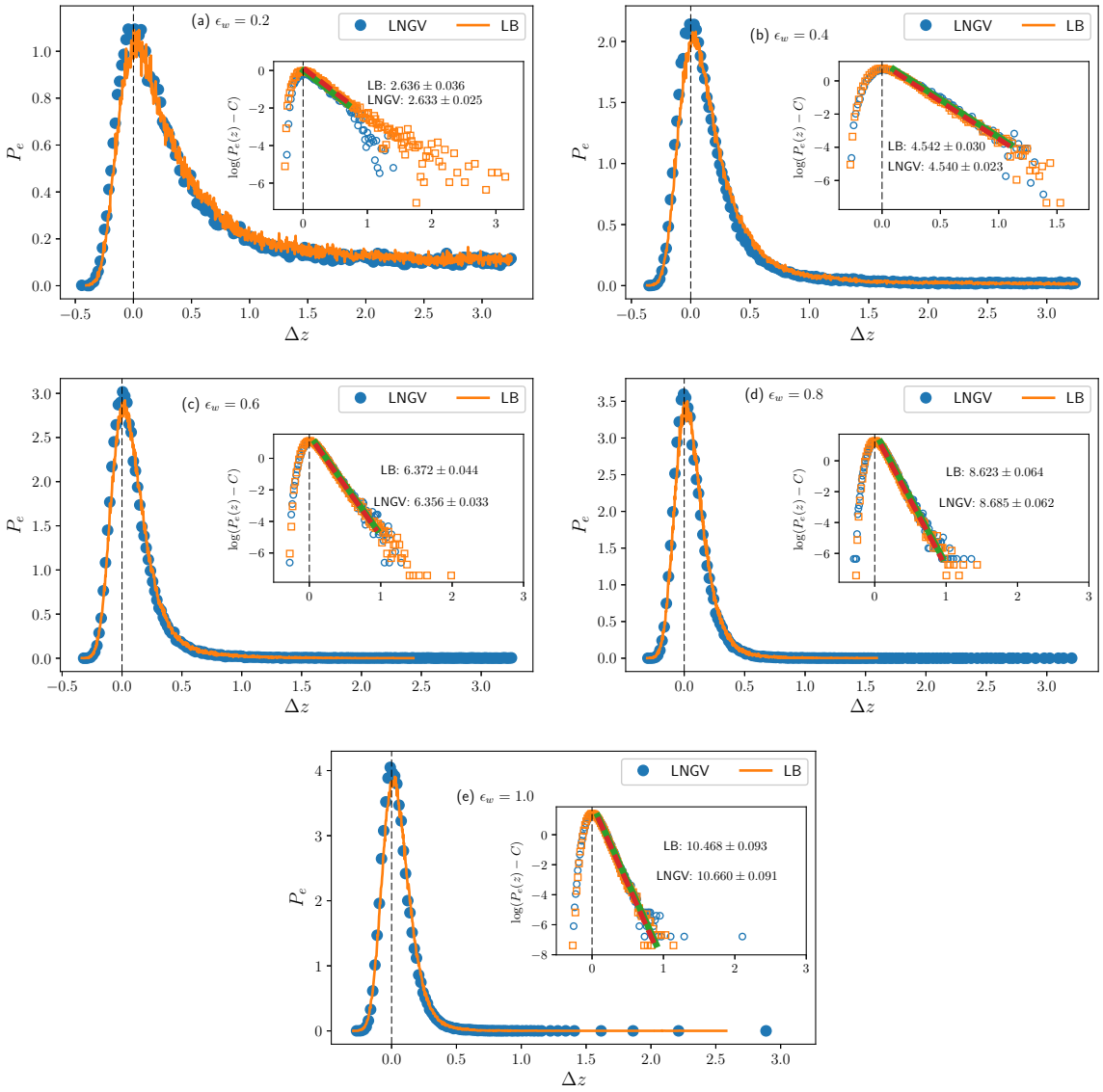

Figure 3.15: Probability distribution of the monomer's elevation from the surface at $z = 0$ for $\epsilon_w = 0.2, 0.4, 0.6, 0.8, 1.0$. The inset figures in each shows linear fits on the tails of the distribution on a log scale to match the results obtained from both thermostats. Lattice-Boltzmann thermostat (LB), Langevin thermostat (LNGV)

3.13, we again compute the effective potential from the monomer's elevation distributions using equation 3.5 and plot the results in (3.16). This time, unlike the earlier figures we again get excellent agreement between the potentials from both thermostats for the monomer across all ϵ_w values. The curves become noisy for larger values of Δz for

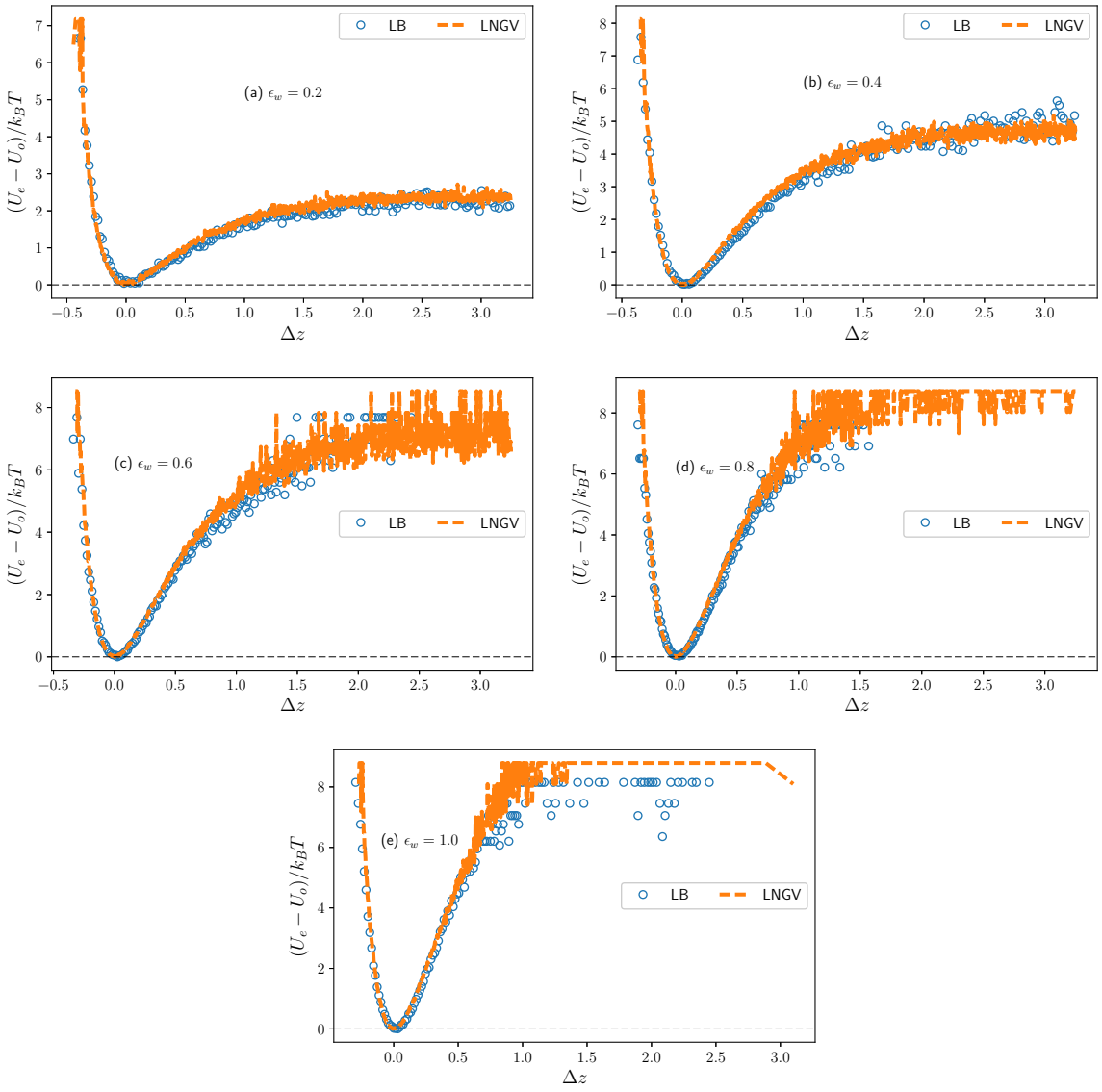

Figure 3.16: Normalized effective potentials, U_e derived from the monomer's elevation distributions for $\epsilon_w = 0.2, 0.4, 0.6, 0.8, 1.0$. (blue circles) Lattice-Boltzmann (LB), (orange, dashed curve) Langevin (LNGV)

$\epsilon_w = 0.6, 0.8, 1.0$ since in these cases the monomer is quite strongly confined within the surface potential well and over the course of the simulation its deviation from the minimum to larger values is quite rare. Given the finite duration of the simulation, the monomer just did not sample those points in its phase space sufficiently enough, resulting in noiser distributions and effective potential curves. But regardless of these finite size

effects, all the curves (distributions and effective potentials) are in really good agreement with each other. These figures, illustrate very well that properly calibrating the coupling constant, γ in the LB fluid results in accurate fluid temperature reproduction and proper implementation of the *no-slip* boundary condition on the monomer's surface as shown in [120].

3.0.3 A single monomer

We first examine the effect of simple shear flow on a single monomer. We have already examined the equilibrium behavior of monomers in figure (3.16) and in figure (3.17a) we plot the effective potential obtained for the same monomer in shear, $\dot{\gamma} = 1.0$ and observe almost no difference in the derived effective potential. Although the Boltzmann' probability for a particle is an equilibrium property, performing the same analysis in shear with essentially identical results demonstrates that the ambient fluid flow has very little influence on the likelihood of a finding a single monomer close to the surface. The same result is obtained for the 1.4 nm case in figure (3.17b).

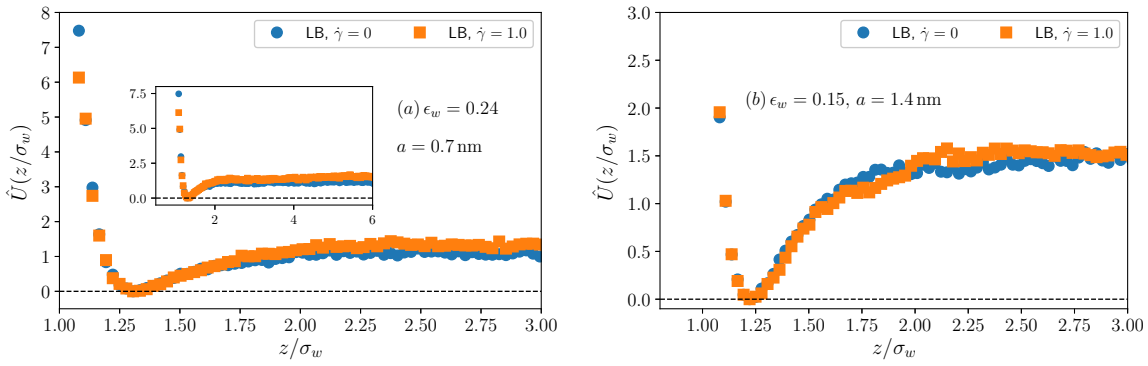

Figure 3.17: (a) Comparing the pseudo potential derived from the position distribution of a single 0.7 nm monomer in shear flow, $\dot{\gamma} = 1.0$ to its equilibrium counterpart. (b) Effective/pseudo potential(s) derived from the position distribution of a single $a = 1.4\,\mathrm{nm}$ monomer in equilibrium and in shear $\dot{\gamma} = 1.0$. The surface interaction strength, ϵ_w in this case was set to 0.15 and the interaction length scale, σ_w was set to 2.12 nm

This result is not really a surprise as a single sphere in a simple shear flow, in the absence of noise and any potential interactions with the wall, will typically simply follow a streamline [49]. In the presence of walls, there is a small hydrodynamic force that, without noise, will eventually cause the sphere to move to the center of the channel [84]. However, in our simulations we have noise which means the sphere moves from the streamline it starts on due to diffusion. As we saw in figure (3.16) this allows the sphere to explore the full energy landscape in equilibrium. In shear, the results in figure (3.17) demonstrate that the presence of shear does not significantly affect this result. It should also be noted that, based on [84], any hydrodynamic force on a single monomer would be expected to move it away from the wall towards the center of the channel and that

this tendency would be greater for the larger sphere. For nanometer sized particles, this effect is tiny and is overwhelmed by the thermal noise.

3.0.4 Max monomer height & Center of mass

To quantify the margination of our chains multiple parameters based on the monomer positions in the direction normal to the surface at $z = 0$ can be calculated. In all our simulations every 120 steps we saved the chain's conformations to disk and carried out our analysis using those trajectories. One of the ways we characterized the chain's margination was by analyzing the distribution of the maximum height attained by a single monomer, z_m for each sample configuration over the course of a simulation. In

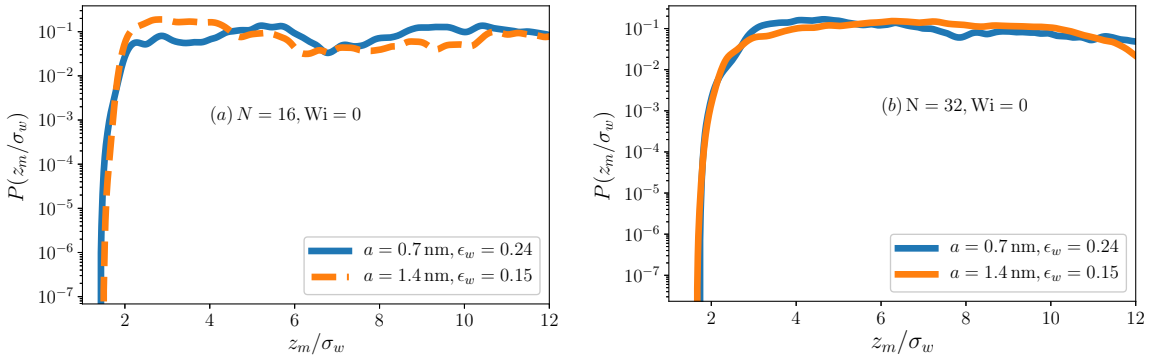

Figure 3.18: Probability density of the maximum height of a single monomer above the surface in equilibrium, Wi = 0 (a) N = 16 (b) N = 32

figure (3.18), we plot the probability distribution of z_m scaled by the surface interaction length scale, σ_w for both the different chain lengths, $N = 16, 32$ in equilibrium (Wi = 0). From these plots we can see that in both cases the distributions are mostly uniform across the entire channel width. This result indicates that the chains, regardless of the monomer sizes, display similar behavior in equilibrium. Moreover it should also be clear from these distributions that in absence of any flow the polymers do not show a strong tendency to adsorb onto the wall for any substantial period of time.

Now in order to address the effect of shear flow on the chain's margination, in figure (3.19) we plot the residual distribution, $\Delta P_{\mathrm{Wi}} = P_{\mathrm{Wi}} - P_0$ versus z_m/σ_w which is basically the difference between the in-shear and equilibrium distributions. From figure (3.19) to begin with, we can note that in all cases the residuals distributions show a leftward shifting trend that indicates an apparent increase in the probability for z_m being within $z_m = 2$ to $4\sigma_w$ from the surface. Secondly the trend is also such that the peak heights increase with increasing Weissenberg number. Apart from these overall trends a closer look at the curves makes it apparent that monomer size has a noticeable impact on the residual distributions. By analyzing plots (3.19a,c) versus (3.19b,d) we can notice that in comparison to the $a = 0.7\,\mathrm{nm}$ case, the shift in probability density towards lower values of z_m is stronger and clearer in the $a = 1.4\,\mathrm{nm}$ case for both chain lengths, $N = 16, 32$. Even at the lowest non-zero shear rate the $a = 1.4\,\mathrm{nm}$ monomer radii chain

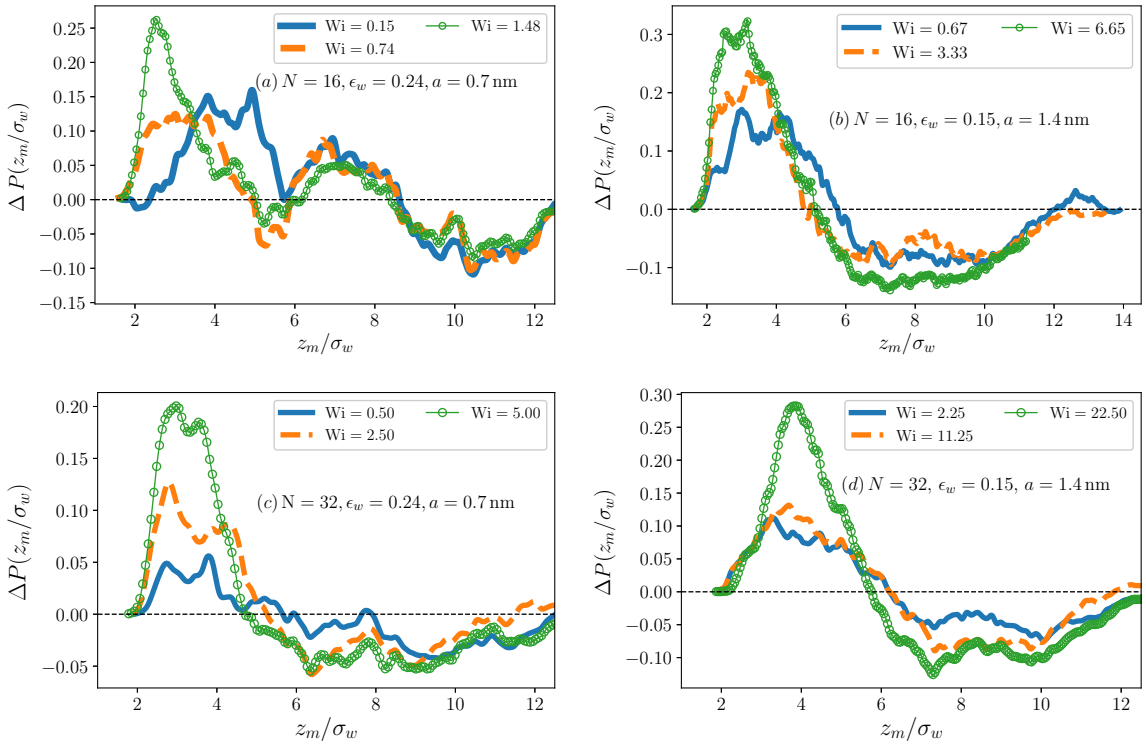

Figure 3.19: Residual distributions, $\Delta P(z_m/\sigma_w) = P_{\mathrm{Wi}}(z_m/\sigma_w) - P_0(z_m/\sigma_w)$ of the maximum height attained by a single monomer away from the no-slip surface at $z = 0$ in shear. The four different plots are for the cases (a) $N = 16, a = 0.7\,\mathrm{nm}$ (b) $N = 16, a = 1.4\,\mathrm{nm}$ (c) $N = 32, a = 0.7\,\mathrm{nm}$ (d) $N = 32, a = 1.4\,\mathrm{nm}$ respectively. The statistical error in the measurement of the probability distribution for the equilibrium case is about 0.05 which sets a lower bound for the statistical error in the residuals plotted here.

shows a significantly higher probability concentration in the $z_m = 2$ to $4\sigma_w$ range from the surface in comparison to its $a = 0.7\,\text{nm}$ counterpart (where the trend is barely visible above the statistical fluctuations). This trend can also be seen to hold true for higher shear rates and the larger monomer chains display a higher propensity for margination in shear. From the latter two figures, i.e. (3.19c,d) we can again see evidence for stronger margination in shear for the larger monomer chain as well as for the longer chains.

Since we are measuring distributions of the maximum height attained by a single monomer such a trend illustrates that shear tends to compress the chain's normal extent into the bulk and causes them to attain flatter conformations on the surface. We also quantified the chain's lateral size by measuring its radius of gyration in the normal direction to the surface and observed similar trends. Results and discussion pertaining to the chain's size is carried out in a later section. Since the relaxation timescale of the principal Rouse mode, τ_1 scales with the monomer size due to its dependence on the drag coefficient, $\zeta = 6\pi\eta a$, and the bond length b, the apparent increase in the margination tendency of the larger monomer sized chains may be explained in the light of longer relaxation times. As the chains assume flatter and elongated conformations on the surface, despite being of the same length and under the influence of the same surface potential, larger monomers couple more with the background fluid flow, which eventually causes the chain to maintain its elongated state for longer durations. Such elongated conformational states result in a severe entropic losses which cause the chains to marginate more towards the surfaces as under such circumstances, it becomes energetically favorable for the chains. In an effort to see if this is the case we looked at the residual distributions all scaled individually by their respective Wi numbers but we were unable achieve a reasonable collapse of the data suggesting there may be more to the effect than can be explained by scaling with the relaxation time of the polymer in equilibrium and in bulk.

Another related parameter to assess the chain's margination in shear is its center of mass normal to the surface, z_{cm}. In figure (3.20) we plot the residual distributions of the same scaled by the surface interaction strength, σ_w and observe trends very similar to the ones depicted in figure (3.19). In these figures, we only plot the $a = 1.4\,\text{nm}$ monomer case to illustrate the behavior. The strongest peaks observed in these distributions in

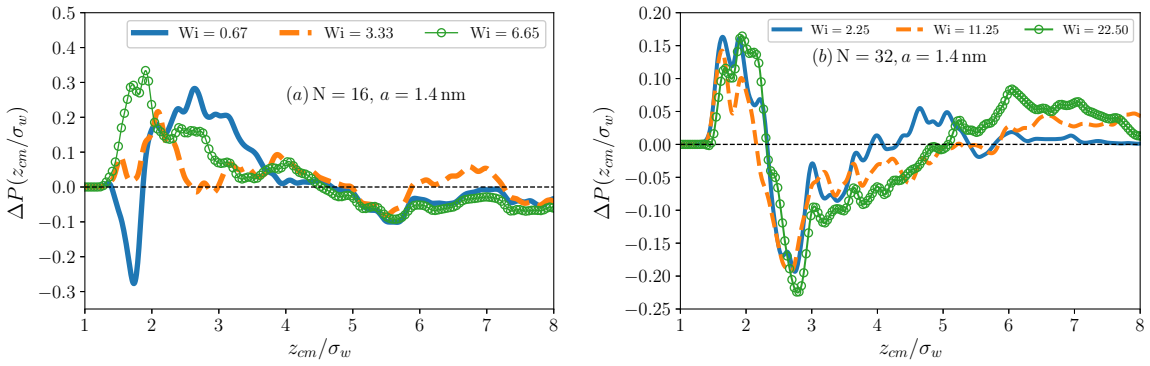

Figure 3.20: Chain's normal center of mass residual distribution, $\Delta P_{\text{Wi}}(z_{cm}/\sigma_w) = P_{\text{Wi}}(z_{cm}/\sigma_w) - P_0(z_{cm})$. The two different plots are for the cases (a) $N = 16, a = 1.4\,\text{nm}$ (b) $N = 32, a = 1.4\,\text{nm}$ respectively

figure (3.20) all seem to peak over the interval $(1.5, 3.0)\,\sigma_w$ and this is somewhat to be expected since the minimum of the surface interaction potential lies well within that interval. From all the observations discussed in this and the previous subsections, it is reasonable to conclude that longer chains and chains with the larger monomers are more likely to remain within the vicinity of the surface in shear and tend to marginate better in comparison to the shorter and smaller radii monomer chains.

3.0.5 Radius of Gyration

In the previous sections, we saw larger monomer and longer chains had enhanced margination. To see why it is helpful to examine the chain's conformational behavior in shear. In shear and elongational flows, polymers undergo severe conformational changes as they stretch and relax along the shear direction and tumble end-to-end incessantly [6, 7, 34, 108, 147, 158, 182]. On thermodynamic grounds, such dramatic conformational changes result in severe conformational entropy losses for the polymer as the flow prevents it from retaining the equilibrium conformations of a three-dimensional self-avoiding walk which is the entropy maximum [117]) for a free polymer. In pressure driven flows this causes a tendency for net migration of the chain away from the surface towards areas of low shear rate where this effect is diminished i.e. towards the channel center line. In a Couette flow, however due to the uniform shear rate across the channel, migrating away from the no-slip surface is not entropically helpful for the chains.

In this section, by looking the radius of gyration of the chains we investigate their unfolding in shear flow near the surface and demonstrate that relative to the $a = 0.7\,\text{nm}$ case, chains with $a = 1.4\,\text{nm}$ sized monomers are somewhat more likely to be in the elongated conformations. Based on the earlier observations of relatively stronger margination tendencies of the $a = 1.4\,\text{nm}$ chains in shear such elongated and compressed conformations imply more monomers being adsorbed on the surface making the situation energetically favorable for them, thus compensating somewhat for the entropic losses.

For quantifying the chain's conformation changes we computed its radius of gyration in the principal directions i.e. R_x, R_y, R_z by simply computing the average extent of all the monomers relative to the chain's center of mass in either of the directions.

$$R_\alpha = \sqrt{\frac{1}{N}\sum_{i=1}^{N}\left(R_{i,\alpha} - R_{c,\alpha}\right)^2} \tag{3.6}$$

where $\alpha = x, y, z$, $R_{i,\alpha}$ is the i^{th} monomer's coordinate in direction α and $R_{c,\alpha}$ is chain's center of mass coordinate along the same (recall that the y-direction is along the flow and z is the direction normal to the wall). In our analysis we scaled all the gyration measurements in the x, y direction by the bulk gyration value $N^\nu\, a$ where $\nu \approx 0.588$ and used the surface interaction potential length scale σ_w to scale the gyration measure of the chain normal to the surface, R_z. To study the effect of shear we again compute the residual distributions, $\Delta P_\alpha = P_{\text{Wi}}\left(R_\alpha\right) - P_0\left(R_\alpha\right)$ for all the gyration measures. We plot the residual distributions of R_y and R_z in figures (3.21, 3.22). We omit the gyration results from the $\dot{\gamma} = 0.2$ shear rate case as no significant differences from the equilibrium case were observed.

In figure (3.21 a, c) we plot the residual distributions for the R_y and R_z gyration measures for the $N = 16, 32$ chains. We notice that the residuals are positive at larger values of R_y in both cases indicating the elongation of the chains along the shear direction. The corresponding negative residuals of ΔP_y at smaller values of R_y clearly indicate that the chains are less likely to be in compact configuration in this case. Furthermore, it is also interesting to note that the R_y residuals are always higher in probability at larger values of the R_y in the $a = 1.4\,\text{nm}$ case. From figure (3.21 b,d), the residual distributions for R_z show an opposite trend as the peaks move leftward towards smaller values of R_z. This indicates that the chains on average in shear are much more likely to be in conformations which are rather elongated along the shear direction and compressed laterally. Plotting

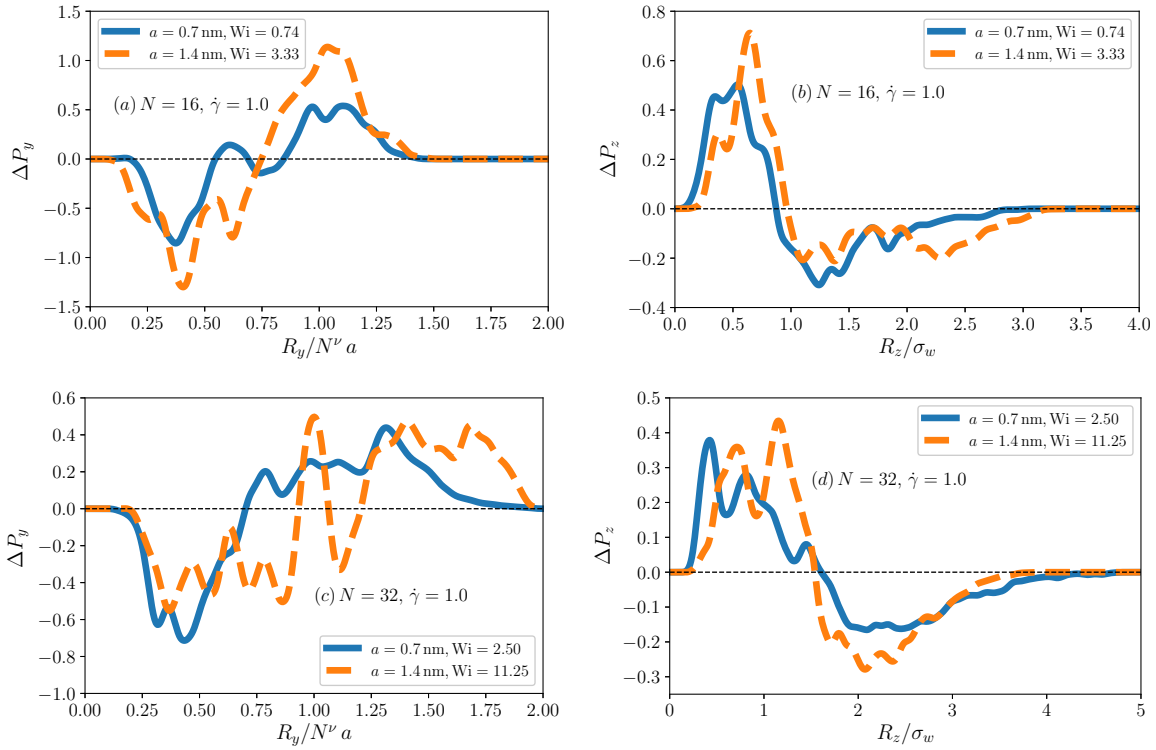

Figure 3.21: Residual distributions of the radius of gyration of the $N = 16, 32$ chains in the direction parallel to the shear flow, R_y and normal to the surface. Blue line represent the $a = 0.7\,\text{nm}$ case whereas the dashed line represents the distributions obtained in the $a = 1.4\,\text{nm}$ case. Figure (a,c) Residual distribution for R_y for the $N = 16, 32$ chains in $\dot{\gamma} = 1.0$ respectively. Figure (b, d) Residual distribution for R_z for the $N = 16, 32$ chains in $\dot{\gamma} = 1.0$

the same distributions for the shear rate $\dot{\gamma} = 2.0$ in figure (3.22) we notice the same trends as before but more pronounced in nature.

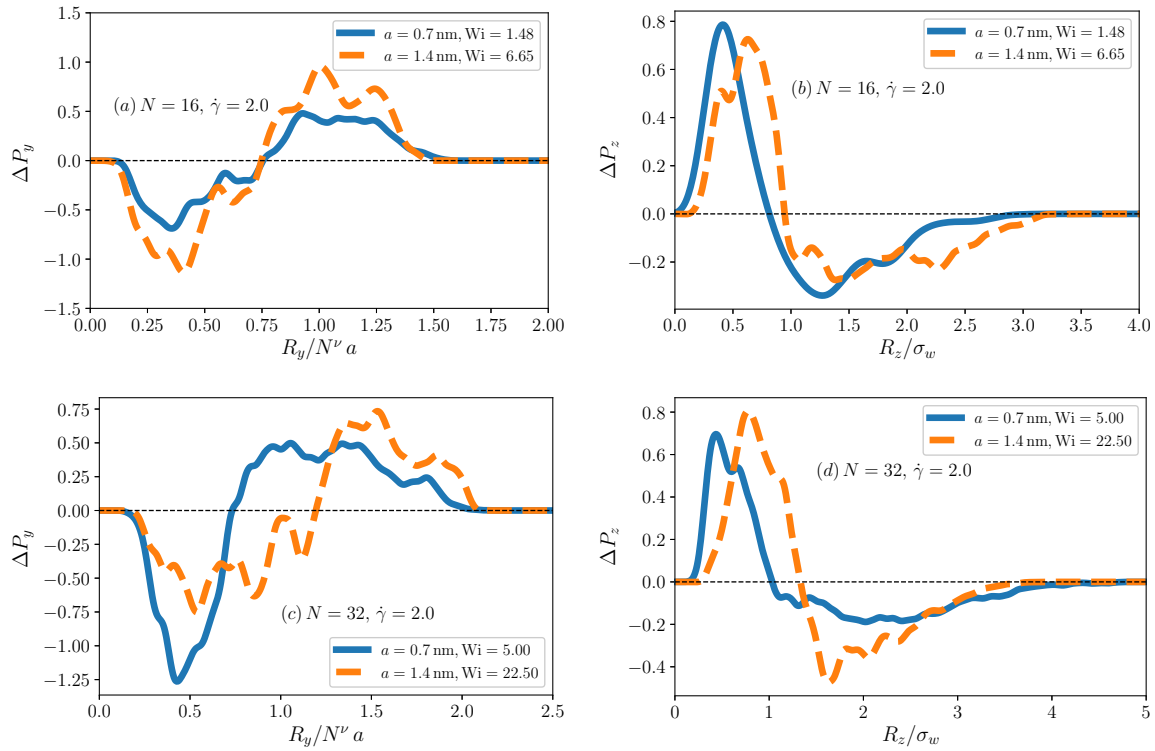

Figure 3.22: Residual distributions for the radius of gyration of the $N = 16, 32$ chains in shear flow, $\dot{\gamma} = 2.0$. Blue line represent the $a = 0.7\,\text{nm}$ case whereas the dashed line represents the distributions obtained in the $a = 1.4\,\text{nm}$ case. Figure (a,c) Residual distribution for R_y for the $N = 16, 32$ chains in $\dot{\gamma} = 2.0$ respectively. Figure (b, d) Residual distribution for R_z for the $N = 16, 32$ chains in $\dot{\gamma} = 2.0$

Furthermore to ensure that the chains in shear were not in any *log-rolling*, states i.e. extended mainly along the x direction, in figure (3.23) we plot the residual distributions of chain's the radius of gyration in the x direction i.e. R_x for all the shear rates. First, it can be noted that the distributions for the $a = 1.4\,\text{nm}$ radii monomers are more pronounced in comparison to the $a = 0.7\,\text{nm}$ case indicating that larger monomers chains are affected by the shear flow more strongly. We also note that the distribution peak over smaller values of R_x indicating that in shear flow, the chain's extent in this direction becomes restricted as the chains tend to align more in the direction of the shear flow.

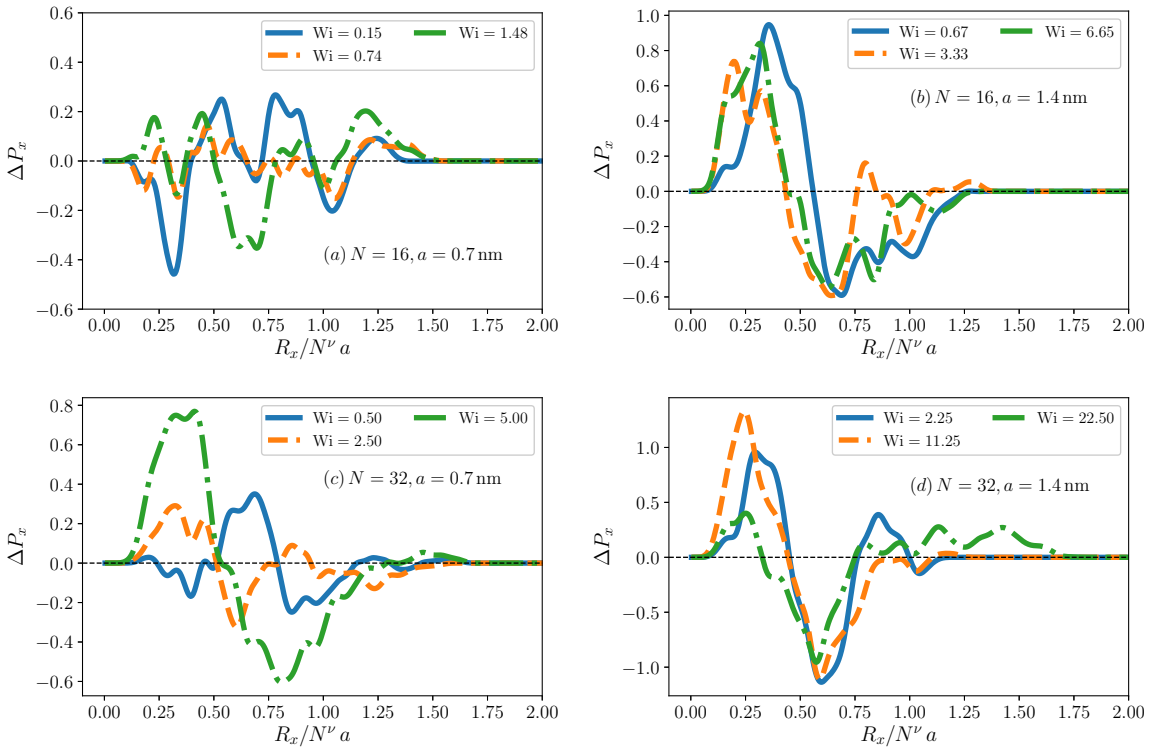

Figure 3.23: Residual distributions for the radius of gyration of the chains in the x direction, R_x for all the non-zero shear rates. (a) $N = 16, a = 0.7\,\text{nm}$ (b) $N = 16, a = 1.4\,\text{nm}$ (c) $N = 32, a = 0.7\,\text{nm}$ (d) $N = 32, a = 1.4\,\text{nm}$. We omit plotting the equilibrium distribution of R_x since the effects of shear flows is best illustrated by considering the residual distributions as plotted here. The actual form of the equilibrium distribution of R_x is a Gaussian at $\text{Wi} = 0$

From the residual distributions of R_z plotted in figures (3.21) and (3.22) we can note that the lateral extent of the chains is comparable to each other in both cases i.e. $a = 0.7, 1.4\,\text{nm}$ as they all peak roughly over the same range of values for R_z and attain similar heights, whereas the distributions for R_y and R_x are more clearly different for the polymer with larger monomers. Overall, the results is that larger monomer and longer chains experience a greater loss of entropy in shear (i.e. the distribution of conformations is farther from the equilibrium distribution).

There a number of competing effects at play in this system. The first is the energy from the wall-monomer potential which favors adsorbtion onto the wall. However, to gain from this energy the polymer must first adopt a 2-dimensional configuration which obviously has reduced entropy compared to the typical 3-dimensional self-avoiding random walk the polymer prefers in equilibrium. Secondly, the shear exerts a hydrodynamic force on the monomers. This force is greater for larger particles as the hydrodynamic drag force is proportional to the particle size. There is also a hydrodynamic force between monomers. This effect is similar to particle entrainment in a fluid stream where larger particles have a much higher tendency to become entrained than smaller particles [128]. These forces act to elongate the polymer along the flow direction and are larger for the

larger monomers. Finally, there is the relaxation time of the polymer relative the shear rate, as typically captured by the Weissenberg number, Wi. When Wi is small, the polymer should have time to relax towards it equilibrium configuration and should therefore be less elongated compared to when Wi is high. For the same shear rate, the relaxation time of a polymer with larger monomers is expected to be larger, as described in Eq.(3.2) thus leading to a larger Weissenberg number. Note that this is distinct from the second point above which relates to the force felt by a monomer as opposed to how long it takes to respond to this force.

Once the polymer is elongated in shear and assumes something closer to a two (or one) dimensional structure, it may as well take advantage of the energetic effects that favor adsorption onto the wall. The caveat is that this is an equilibrium argument that is not guaranteed to hold in the out-of-equilibrium situation studied here. In particular, if the polymer is rapidly rearranging its configuration it may not have time to take advantage of the adsorbtion energy before it changes to a configuration where adsorbtion is less beneficial. Even if the deadsorbed state is short lived it could have a significant impact on the overall likelihood of adsorbtion. Again, in this case the slower response time of the larger monomers favors their adsorbtion over the smaller monomer chains.

Chapter 4

Nanorods dispersion in polymer melts

In this chapter we present the results from our work on polymer nanocomposites studied using coarse-grained MD simulations through LAMMPS [130, 176]. The dispersion patterns of nanorods in a pool of attracting polymer chains is a less explored field and is the primary focus of our work. We simulated a polymer-nanorod composite where all interactions were repulsive except for the polymer-rod. We looked at the effect of such interactions on the dispersion of the nanorods within the melt as well as on their orientations. We also looked at the effects of the nanorods on the conformations of the interfacial polymer chains i.e. the chains in close proximity to the rods. In section (4.0.1), we provide the details our simulation model and the parameters used to run the simulations in LAMMPS. Following that in section (4.0.2), we present the results from our work on the dispersion of the nanorods in the melt for different concentrations. We do so by providing snapshots from our simulations as well as several quantitative measures such as the average distance between nanorods once the melt is sufficiently equilibrated. In the final results section i.e. (4.0.3) we present the results from our work on the orientation of the nanorods in our melt at different concentrations. We also show results of the conformational changes of interfacial polymers by looking at their radius of gyrations and comparing them with the values obtained for the chains in the bulk.

4.0.1 Simulation Model

In this work, we adopt a coarse-grained approach to model the polymer-nanorod composite. The melt is comprised of a mix of polymer chains and rigid nanorods. Each polymer molecule is composed of $n_p = 32$ consecutive beads (monomers) connected via Finitely Extensible Non-linear Elastic (FENE) bonds (cf. Fig. 4.1a). The Kremer-Grest FENE potential

$$U_b = -\frac{1}{2}KR_0^2 \ln\left[1-\left(\frac{r}{R_0}\right)^2\right] + 4\epsilon_b\left[\left(\frac{\sigma}{r}\right)^{12}-\left(\frac{\sigma}{r}\right)^{6}+\frac{1}{4}\right]H\left(2^{\frac{1}{6}}\sigma\right) \quad (4.1)$$

is used to implement all the bonded interactions necessary for the monomer interconnectivity within the polymer chains [78]. The first term on the RHS is attractive

in nature with $K = 30\epsilon_b\sigma^{-2}$ being the effective elastic constant where $\epsilon_b = k_BT$, k_B is Boltzmann constant, and T is Temperature. $R_0 = 1.5\sigma$ is the maximum bond extension in any direction and σ is the Lennard-Jones (LJ) length scale. On the other hand, the second term on the RHS represents the repulsive portion of the potential with the cut-off length $r_c = 2^{1/6}\sigma$ enforced through the Heaviside function $H(x)$. This form of potential also eliminates nonphysical bond crossings [78]. Excluded volume of the polymer chains are implemented through a repulsive $12-6$ Lennard Jones (LJ) potential similar to the one used for the FENE bonds. Interactions between the polymers and the rods are also of a $12-6$ LJ potential form. However, the cutoff length for these interactions is set to $r_c = 2.5\sigma$ creating attraction between the polymer chains and the nanorods.

The rigid rods in our system consist of four individual threads (sub-rods) which are assembled in a helical pattern as shown in Fig.4.1b. Each thread has $n_r = 16$ monomers and are interconnected along the backbone via the FENE bonds described in Eq. 4.1 and rigidity of the rods is ensured by a harmonic angle potential U_h for every monomer *triad*

$$U_h = k\left(\theta - \theta_0\right)^2 \tag{4.2}$$

where $k = 1000$ (LJ units) is the spring constant, θ is the angle formed by a triad at any given time during the simulation and θ_0 is its equilibrium value. A rigid conformation is obtained by penalizing any bending of the rods by setting $\theta_0 = 180^\circ$ during the energy minimization step. However, at equilibration and production stages, each rod is treated as a rigid body to reduce computational cost of the simulation without compromising the physics. The diameter and length of the rods are respectively $D \approx 2.35\sigma$ and $L \approx 13.35\sigma$ giving them an aspect ratio of about 5.5. The multiple subrods give the nanorods a realistic thickness, surface roughness, and eliminates commensurability between the rods and polymers. This is different from most of previous studies where single thread nanorods [44, 45, 95, 104, 122, 124, 125, 140, 151, 178, 179], hollow nanotubes [71, 72], or smooth (sphero)cylinders were used [20, 180, 189]. All the simulations are done using the open source package LAMMPS [177]. The initial atom coordinates and LAMMPS data files were generated using the *moltemplate* package [64].

One of the main objectives of the present work is to investigate the effect of nanorod inclusion on the conformation of the polymer chains in the melt, especially the chains at the interface of the nanorods. As a measure of the shape and size of the polymers, we calculated the radius of gyration tensor $\boldsymbol{R}_g$ of a chain from the particle coordinates as

$$R^2_{g_{\alpha\beta}} = \frac{1}{M^2}\left[\sum_{i=1}^{n_p} m_i(r_{i,\alpha} - r_{com,\alpha})(r_{i,\beta} - r_{com,\beta})\right] \tag{4.3}$$

where $R^2_{g_{\alpha\beta}}$ is the element of the tensor $\boldsymbol{R}^2_g$ on the αth row and βth column, M is the total mass of the chain, n_p is the number of beads in the chain, and m_i is the mass of the ith bead. The $r_{i,\alpha}$ represents the position of the ith bead in $\alpha = x, y, z$ direction and similarly, the $r_{i,\beta}$ is the position of the ith bead in $\beta = x, y, z$ direction. The r_{com} is the position of the centre of mass of the polymer chain. Then the $|R_g|$ was found by

$$|R_g| = \sqrt{\lambda_1^2 + \lambda_2^2 + \lambda_3^2} \tag{4.4}$$

where λ_i is the ith eigenvalue of the gyration tensor. A set of 10 realizations of a pure melt is run and the average radius of gyration of the polymer is measured to be $R_0 \approx 3\sigma$. This value is used as a reference throughout the paper.

A fixed number of polymer chains $N_p = 1000$ is used across realizations whereas the total number of rigid rods N_r in the melt is varied in order to achieve different concentrations of nanofillers. We quantify the concentration of the rods ϕ_c by simply taking the ratio of the total number of rod monomers to the total number of polymer monomers

$$\phi_c = \frac{\text{number of rod beads}}{\text{total number of beads}} = \frac{(4 \cdot N_r)n_r}{N_p n_p + (4 \cdot N_r)n_r} \tag{4.5}$$

where $n_p = 32$, $n_r = 16$, $N_p = 1000$, $60 \leq N_r \leq 500$, and $0.1 \leq \phi_c \leq 0.5$.

The simulation is started from a random initial configuration and equilibration is conducted carefully to ensure that the system does not get stuck in a kinetically favourable glassy configuration. The thermodynamic variables of the system were monitored to ensure this. Moreover, the direct visualization of the system shows that the polymer chains move reasonable distances and the configuration of the system changes significantly during equilibration as shown in Fig. 4.3. All suggesting that the system has been equilibrated (Fig: 4.3(a)-(c)). All realizations were carried out under an NPT ensemble [9]. The polymers were thermostated using a Langevin thermostat with a damping parameter $t_d = 100\tau$, τ being the LJ time unit, and dimensionless temperature of $T = 1.0$. A Berendsen barostat with the damping factor 5τ was used to maintain the pressure of the system at $P = 1.0$. We used a timestep of $\Delta t = 0.005$ and carried out all our simulations up to a maximum duration of 10^7 MD steps, 9 million steps of equilibration and 1 million steps for production.

Lastly, to improve results statistically, for each value of ϕ_c, a total of ten independent realizations were carried out and the results were averaged over these realizations. All quantities are presented in dimensionless LJ units unless mentioned otherwise.

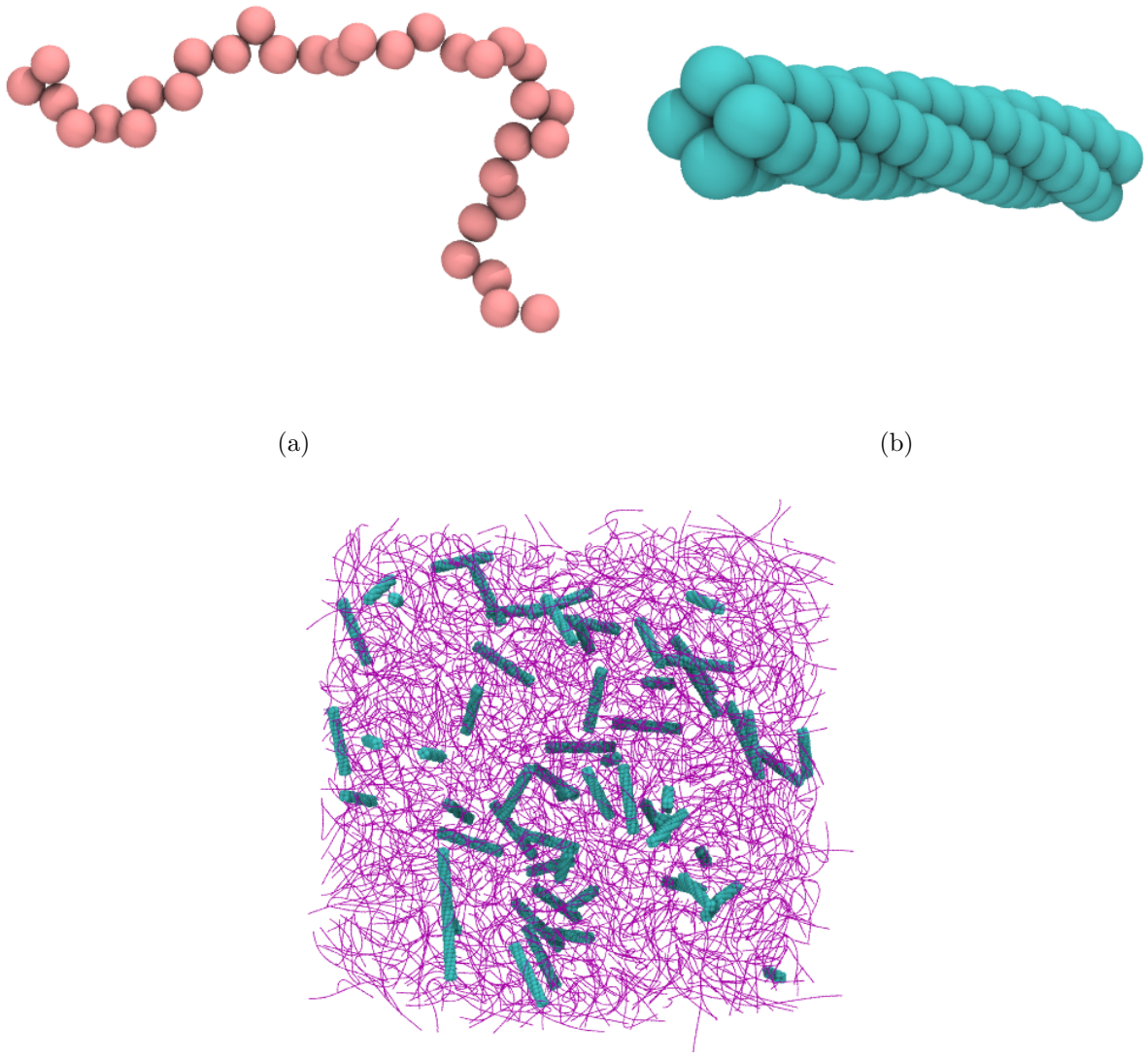

(a) (b)

(c)

Figure 4.1: An example of polymer chain is shown in (a) while (b) shows a lateral view of a nanorod. A random initial configuration, shown in (c), is generated using moltemplate package for each realization. The nanorods are shown in cyan(green) and the polymer chains are shown as purple lines. The VMD software was used for this visualizations [61].

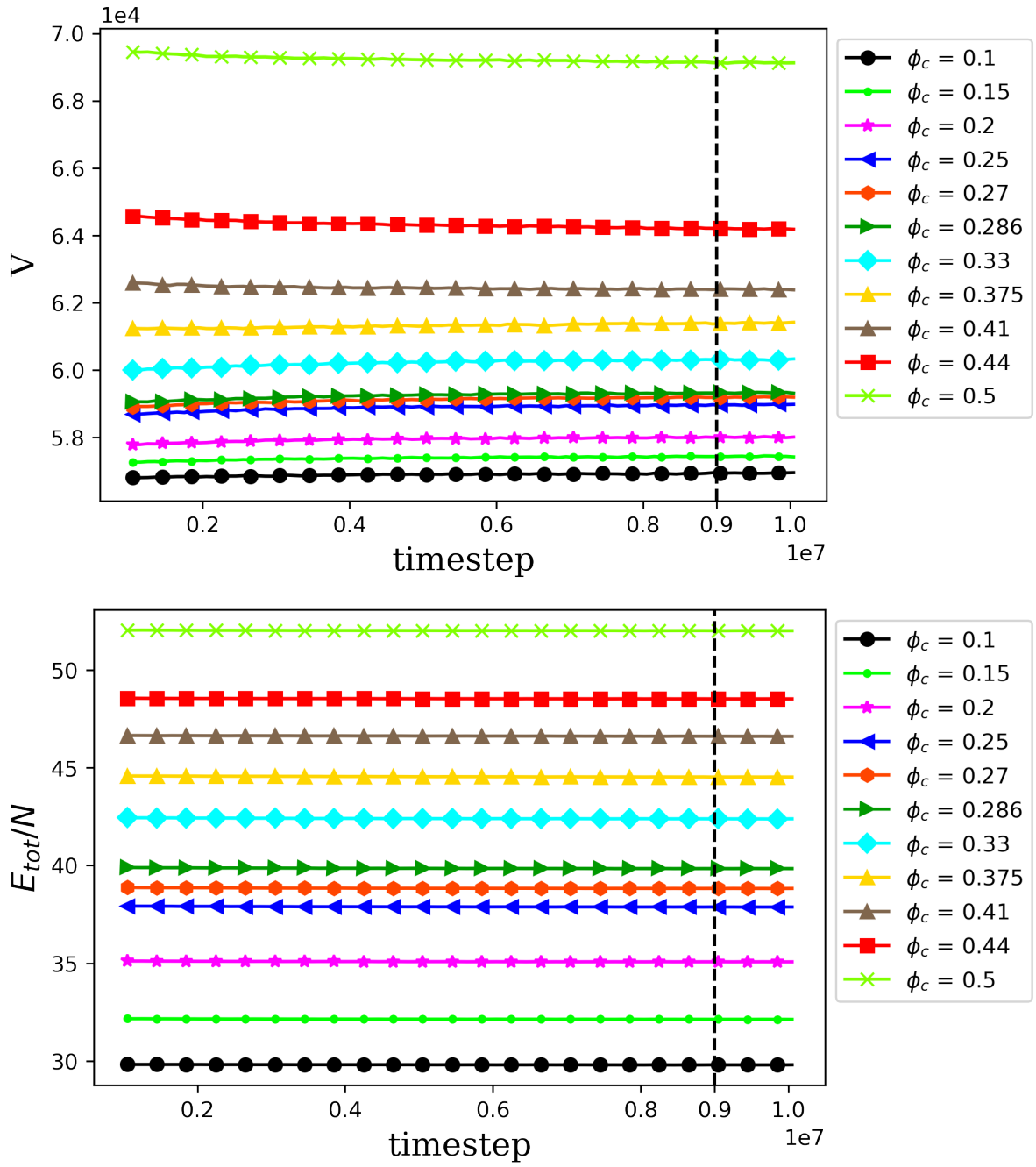

Figure 4.2: The volume and total energy of the system for all concentrations are shown. The dashed vertical lines separate the equilibration (to the left) and production (to the right) stages. Initially, a change in the volume and energy is observed but it levels off and stays constant during production (the last one million steps). The total energy is normalized by the total number of atoms in the system N.

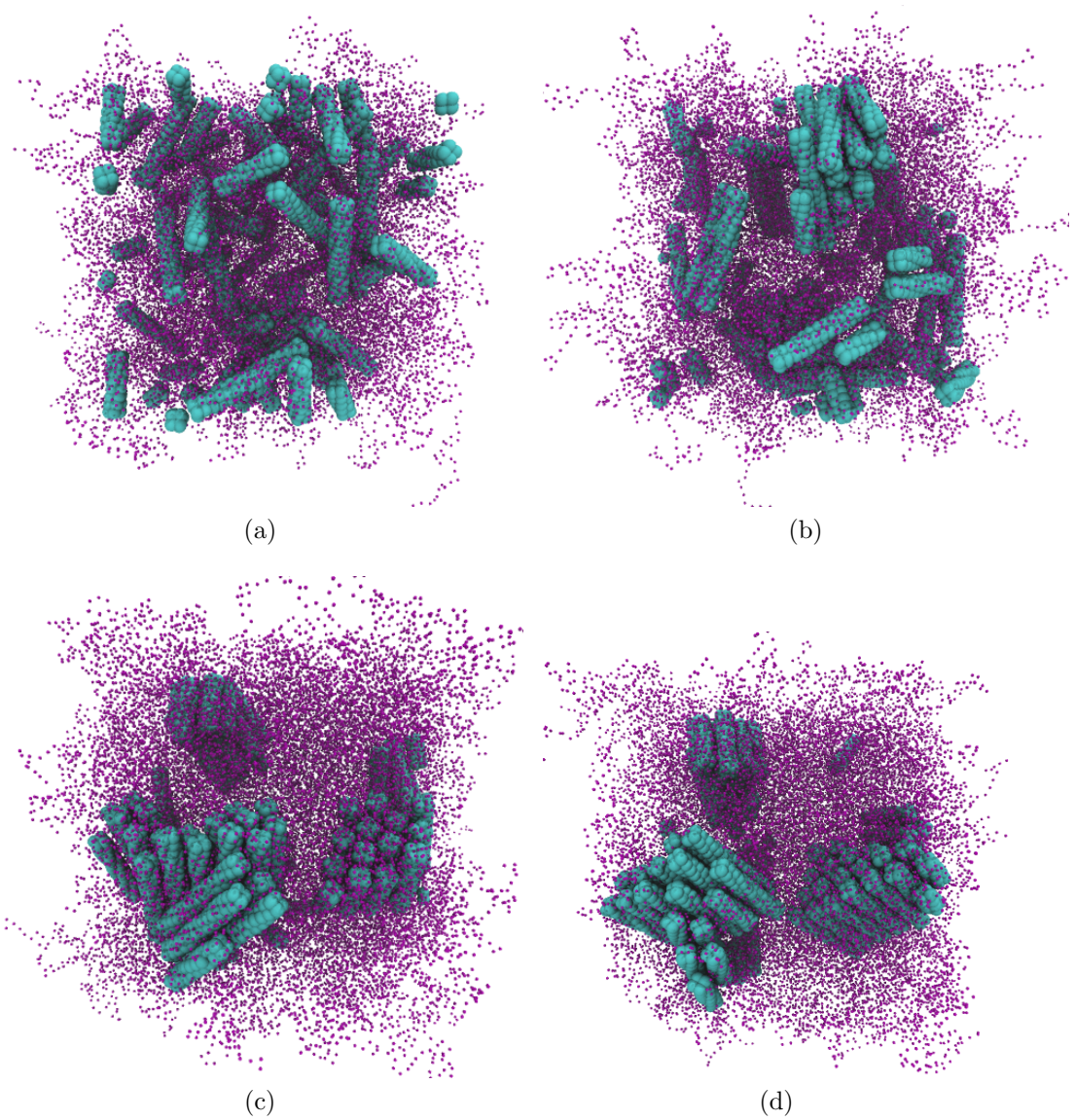

Figure 4.3: A nanorod-polymer melt with nanorod concentration $\phi = 0.1$ and nanorod-polymer Lennard-Jones interaction strength $\epsilon = 1$. As the system evolves, the initial random configurations (a) progress to phase separate and form distinct rod droplets after equilibration (c). (b) shows an intermediate stage. The considerable change in the system configuration is an evidence of full equilibration of the system. (d) shows the final configuration of the system after 9×10^6 equilibration steps and 10^6 production steps resulting in approximately three hours of simulation runtime. The matrix polymer chains are shown as purple dots for illustration purposes.

4.0.2 Dispersion and phase Separation

Rigid rods and nano particles have long been known to have poor dispersion in polymer melts. However achieving optimal dispersion of the rods throughout the melt is extremely important when considering the mechanical and structural properties of the resulting

material. As mentioned earlier, chemically treating the surfaces of the rigid rods has shown to improve dispersion as it boosts their interactions with the polymer matrix [37, 56, 96, 203]. Therefore, due to their practical relevance, we focus on a system of nanorod-polymer composite in which the polymer-rod interactions are attractive while all other interactions are hard-core repulsive.

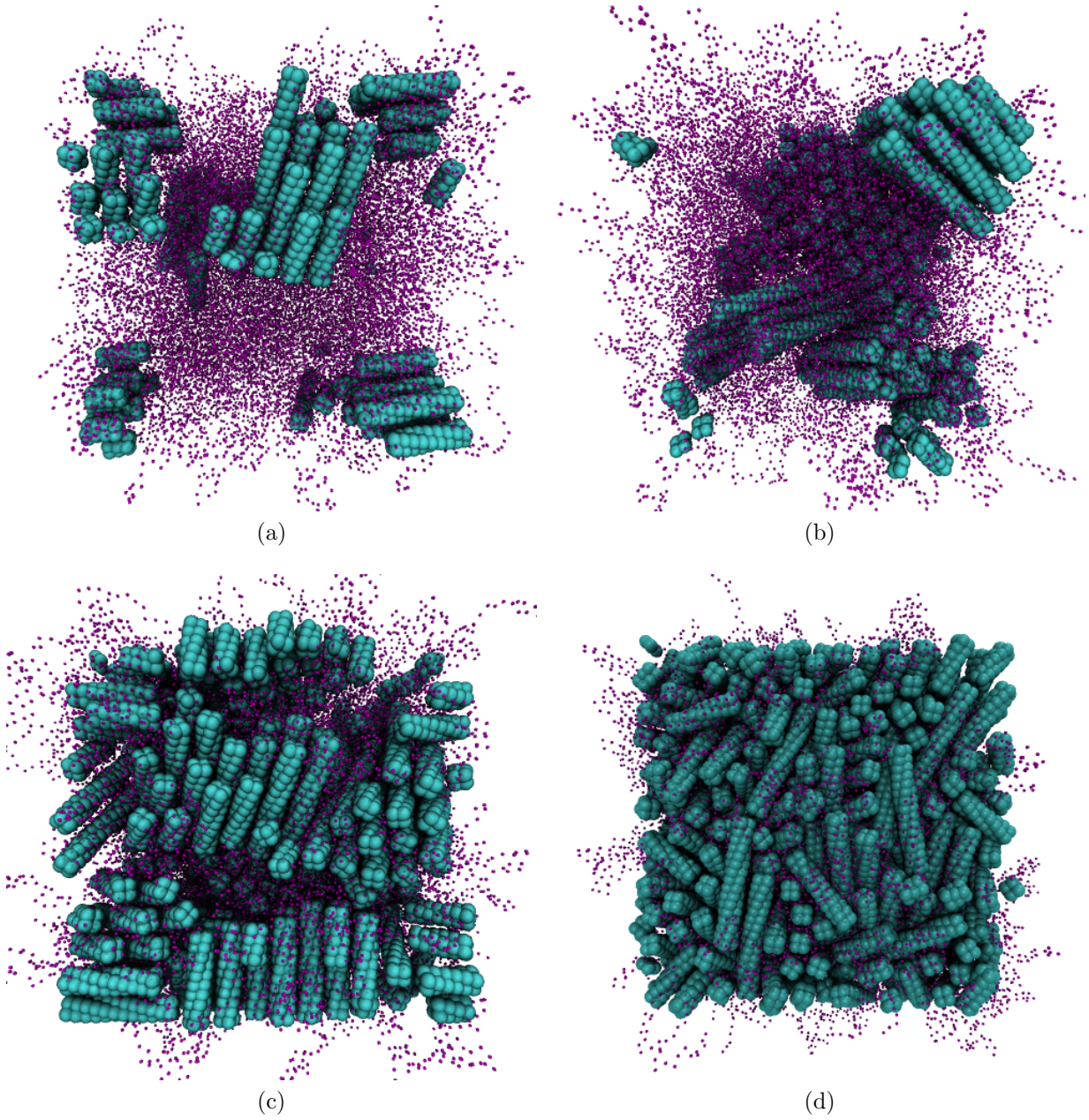

Figure 4.4: Snapshots of the rod-polymer system at concentrations (a) $\phi_c = 0.1$, (b) $\phi_c = 0.2$, (c) $\phi_c = 0.33$, and (d)$\phi_c = 0.5$ are shown. Initially, increasing the concentration of the rods results in the growth of the size of the clusters, but further increase breaks the clusters up and makes the system more isotropic. This is attributed to the interplay of entropic and enthalpic effects.

In figure 4.3, we present snapshots of our system at the lowest concentration i.e. $\phi_c = 0.1$ for polymer-rod interaction strength $\epsilon = 1.0$ as it equilibrates. Figure 4.3a shows the system at an initial stage. As can be seen, the rods start out in a fairly random configuration and are well dispersed throughout the melt. However, as the simulation

progresses, the rods are seen to phase separate. The early stages of this agglomeration is illustrated in figure 4.3b where a few clusters of rods appear. This phase separation continues and distinct droplets of nanorods form at equilibrium, leaving some regions completely filled with only polymers (for lower concentrations). This phase separation has been observed in experiments [59, 183] as well. In most previous computational studies where formation of such clusters were studied, an attractive interaction between rods were at play [95, 179]. However, the formation of such clusters in a system with rod-rod repulsive forces suggests the significance of entropic effects in this phenomenon. At lower rod concentrations, the enthalpic energy gains for the polymers by interacting with the rods is low, thus the chains tend to prefer conformations that increase their conformational entropy. This entails that the polymers tend to phase separate the rods out in order to maximize their conformational entropy. However, since the interaction between the rods and polymers is attractive, the rods do not end up phase separating entirely resulting in distinct clusters.

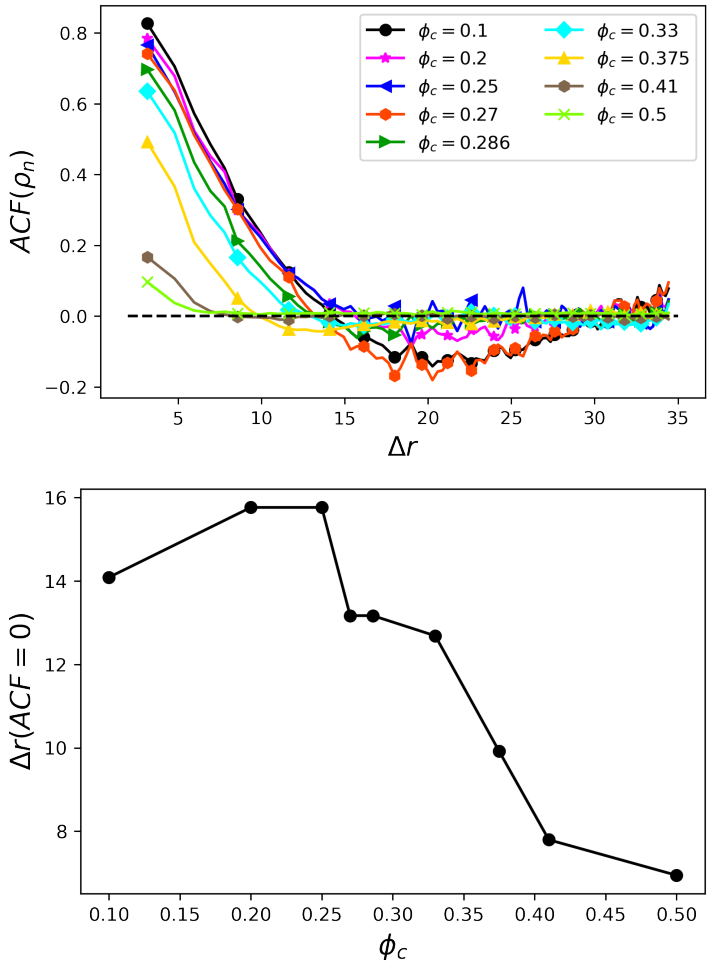

Figure 4.5: (a) shows the auto-correlation function of the number density ρ_n as a function of radial distance from the origin for selected concentrations while (b) shows the intercept of the auto-correlation function with $ACF(\rho_n) = 0$ axis as a function of concentration.

To quantitatively investigate the phase separation visually observed in the simulations, we divide the system into voxels and in each voxel we compute a number density defined as

$$\rho_n = \frac{p_n - r_n}{p_n + r_n}, \tag{4.6}$$

where p_n is the number of polymer monomers and r_n the number of rod monomers in the voxel. The auto-correlation function of this number density characterizes the distribution of particles inside the simulation box. The auto-correlation function for ρ_n is

$$C_{\rho\rho}(r_\rho) = \frac{\langle \rho_n(0) \cdot \rho_n(r_\rho) \rangle - \langle \rho_n \rangle^2}{\langle \rho_n^2 \rangle} \tag{4.7}$$

and found using Fast Fourier Transform, and Wiener-Khinchin theorem [99]. Figure 4.5(a) shows the $C_{\rho\rho}(r_\rho)$ as a function of radial distance from the reference point ($r = 0$). Since we have a periodic boundary condition, we only plot the function for one octant of the simulation box. The 3D distribution obtained from the calculations is mapped onto the radial distance by averaging all the discrete values of the $C_{\rho\rho}(r_\rho)$ within distance r_ρ and $r_\rho + \delta r_\rho$, where $\delta r_\rho = 2.5\sigma$, and assigning the mean value to the point at r_ρ.

In figure 4.5(b), a characteristic length r_{ρ_0} corresponding to the zero-crossing of the auto-correlation function as a function of the concentration is illustrated. We observe a slight increase at the beginning followed by a decay for higher concentrations. The initial increase corresponds to a slight increase in the size of rod clusters seen in simulation snapshots 4.4. From the definition of ρ_n, the decrease at higher concentrations shows that the correlation between the composition of voxels decreases as function of concentration which implies that the polymers and the rods are becoming better mixed.

Another important indicator of the structure of the system is the distance of nanorods from each other in the melt. In figure 4.6(a), we show the probability of finding the centre of mass of the nanorods at a distance Δr from each other. By increasing this shell radius to include larger distances, the number of rods within the shell increases just due to the larger volume. Therefore, we normalize the probability by the volume of the shell. Similar to typical pair correlation function graphs ($g(r)$), peaks in the rod-rod distance plot show spatial order in the system. As can be seen, the graphs show a first peak around 3.25σ at all concentrations which corresponds to the distance between rods within a cluster. The area under the first peak is a measure of the number of rods in a cluster and is plotted as a function of concentration in the inset of figure 4.6(a). At the beginning, the area increases as the concentration increases corresponding to the growth in the size of the droplets, but it reaches a maximum at $\phi_c = 0.33$ and declines after reflecting droplet shrinkage.

Moreover, in figure 4.6(a), the peaks slowly diminish as the concentration goes up which implies that the system at higher concentrations is not as ordered. The system becoming more isotropic is also manifested in the average volume of the system. In figure 4.6(b), we see the average volume versus concentration. The volume initially grows linearly, but beyond $\phi_c = 0.33$, as the system becomes less ordered (particularly the rods), the rate of growth increases. The orientation of rods and the order of the system will be discussed in greater depth in the next section.

To provide a better picture of the processes responsible for the above results, we compare the result of our system with rod-polymer attractive interactions with a system with all repulsive interactions.

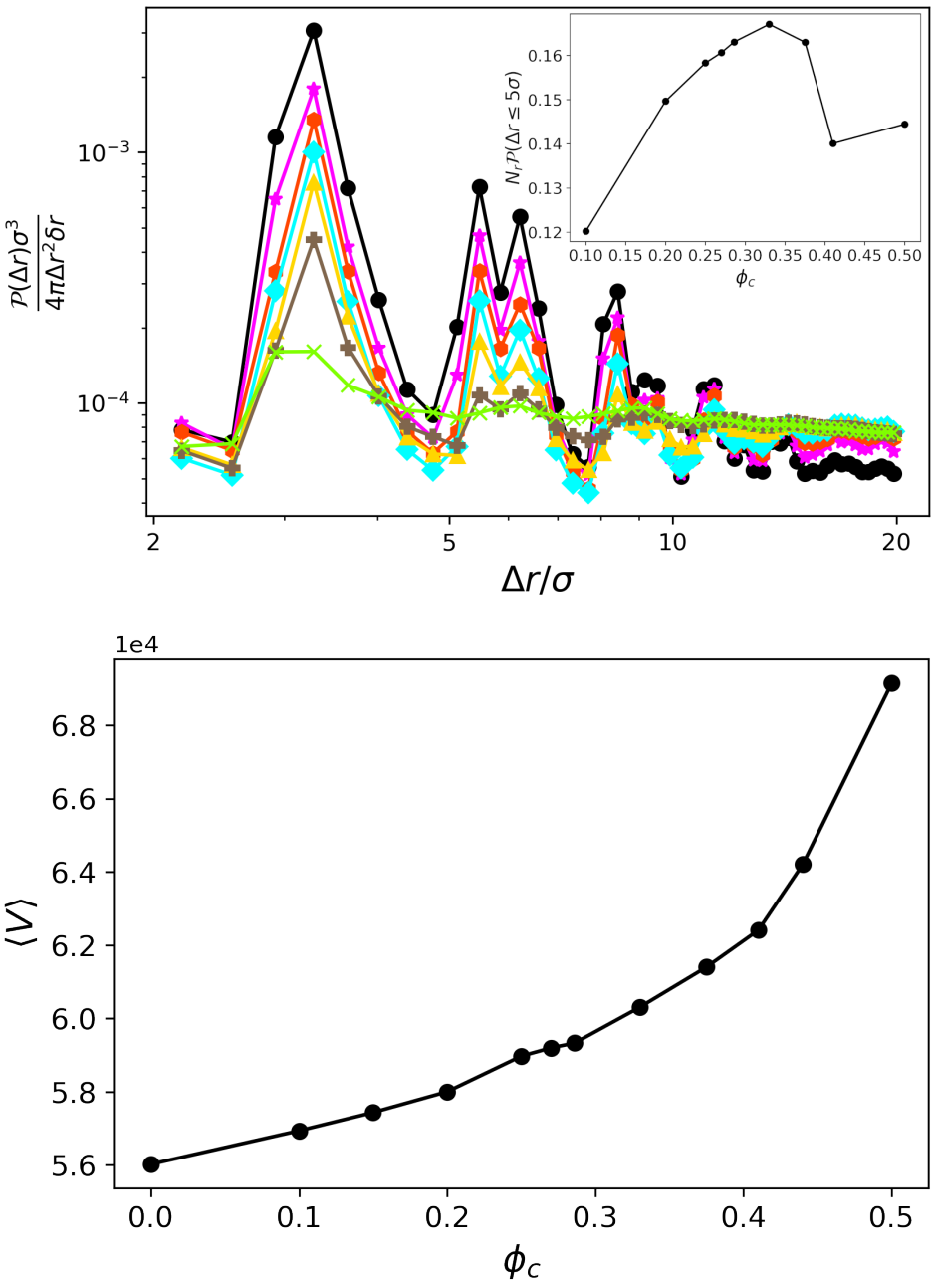

Figure 4.6: In (a), probability density function is shown for the pairwise distance between the centre of mass of the rigid rods in the melt. $\phi_c = 0.1$ (black), $\phi_c = 0.2$ (magenta), $\phi_c = 0.27$ (red), $\phi_c = 0.33$ (sky blue), $\phi_c = 0.375$ (yellow), $\phi_c = 0.41$ (brown), $\phi_c = 0.5$ (green). The inset shows the area under the first peak of the probability density functions versus concentration. (b) shows the average volume of the system as a function of the concentration. The patterns in (a), and (b) suggest that the melt becomes more isotropic and less ordered at concentrations higher than $\phi_c \approx 0.3$.

Figure 4.7(a) shows the $C_{\rho\rho}(r_\rho)$ for a system with repulsive forces between all components. Compared to figure 4.5(a), the graphs reach the $C_{\rho\rho}(r_\rho) = 0$ at larger distances

and we do not observe significant decrease in the zero-crossing as the concentration increases. This shows that the neighbouring voxels contain similar type of atoms. In other words, the rods and polymers are fully phase separated.

The difference in the behaviour of $C_{\rho\rho}(r_\rho)$ of the fully repulsive system and attractive system can be described as follows. The phase separation of the polymers and the rods in the repulsive system is an entropic process and since there is no other processes to compete with, increasing the number of rods does not alter the behaviour of the system significantly. However, in the presence of the rod-polymer attractive interactions, the enthalpic effect that tries to increase the contact surface of rods and polymers competes with the entropic effect pushing the system away from phase separation, and formation of clusters. As a result, increasing the number of rods steers the attractive system towards a more isotropic configuration as it boosts the energetic interactions.

In order to increase their contact surface with the rods, the polymers break up the large clusters of rods into smaller ones as well as penetrate into the space between rods within the clusters. This becomes more evident if we compare the rod-rod centre of mass results for the repulsive and attractive cases. Similar to figure 4.6, figure 4.7(b) shows the probability density of rod-rod centre of mass distance. The maximum probability happens at a distance close to the diameter of the rods $\Delta r \approx 2.35\sigma$ which means the rods directly touch within a cluster while for the system with rod-polymer attractions, the first peak happens at a larger distance which suggests that polymers are present between the rods within a cluster.

This is also observed from direct visualizations of the systems. figure 4.8 shows snapshots of the system for an all-repulsive system. As can be seen, the all-repulsive system shows a full phase separation while the rods are mixed with the polymers in the attractive system shown in figure 4.4(d). One might interpret this as polymers gluing the rods together and therefore determine formation of cluster to be energetically driven [45, 54, 140]. However, as shown by the $C_{\rho\rho}(r_\rho)$ graphs, introducing the attractive forces not only does not bring the rods together but it splits the larger clusters into smaller ones. This implies the phase separation for the system with all purely repulsive forces is entirely driven by entropic effects similar to depletion forces seen in systems of spherical colloids of two different sizes [12, 143]. This type of depletion-induced phase separation is observed in nanorod-polymer solutions before [60]

Another interesting result illustrated in figure 4.3c is the orientation of rods within the droplets. As can be seen, the rods within a cluster align laterally and in parallel. In other words, they form a nematic phase within each droplet. The formation of nematic phase of nanorods in solutions of polymers has been mentioned in the literature [87, 188] and is the topic of the next section.

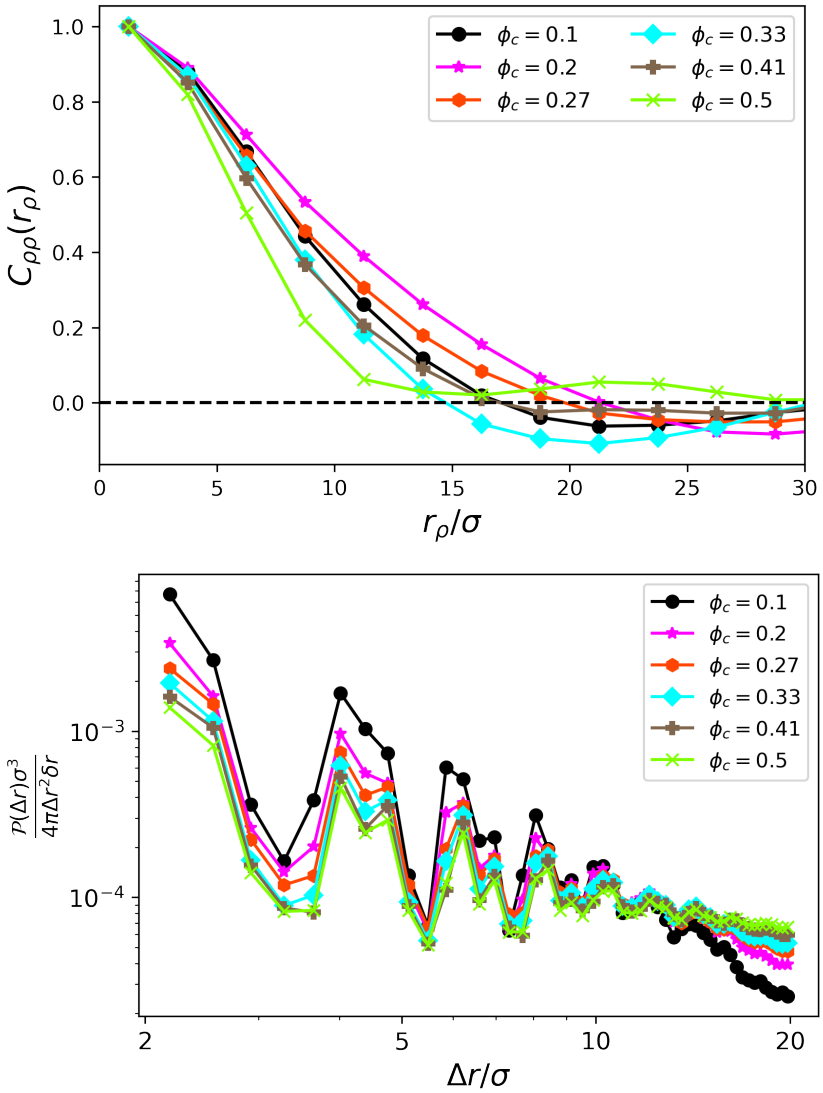

Figure 4.7: The auto-correlation function of the number density (a), and the rod-rod centre of mass distance (b) for a system with all-repulsive interactions are illustrated.

4.0.3 Orientation and Order

4.0.3.1 Rod droplets

In the previous section, we observed that the nanorods tend to phase separate into clusters that visually seem to have nematic order. In this section, we further investigate this possible ordering and phase transition. The best place to start would be to look at the orientational order of the rods as a function of their position. We introduce an orientational correlation C_{rr} as

$$C_{rr}\left(|\Delta \boldsymbol{r}|\right) = \left\langle |\hat{\boldsymbol{e}}_i^r(\boldsymbol{r}) \cdot \hat{\boldsymbol{e}}_j^r(\boldsymbol{r} + \Delta \boldsymbol{r})| \right\rangle \tag{4.8}$$

where $\hat{\boldsymbol{e}}_i^r$ and $\hat{\boldsymbol{e}}_i^r$ are the end-to-end vectors of the ith and jth nanorods and $\Delta r = |\Delta \boldsymbol{r}|$ is the distance between the centre of mass of the nanorods. The value of C_{rr} is 1 for

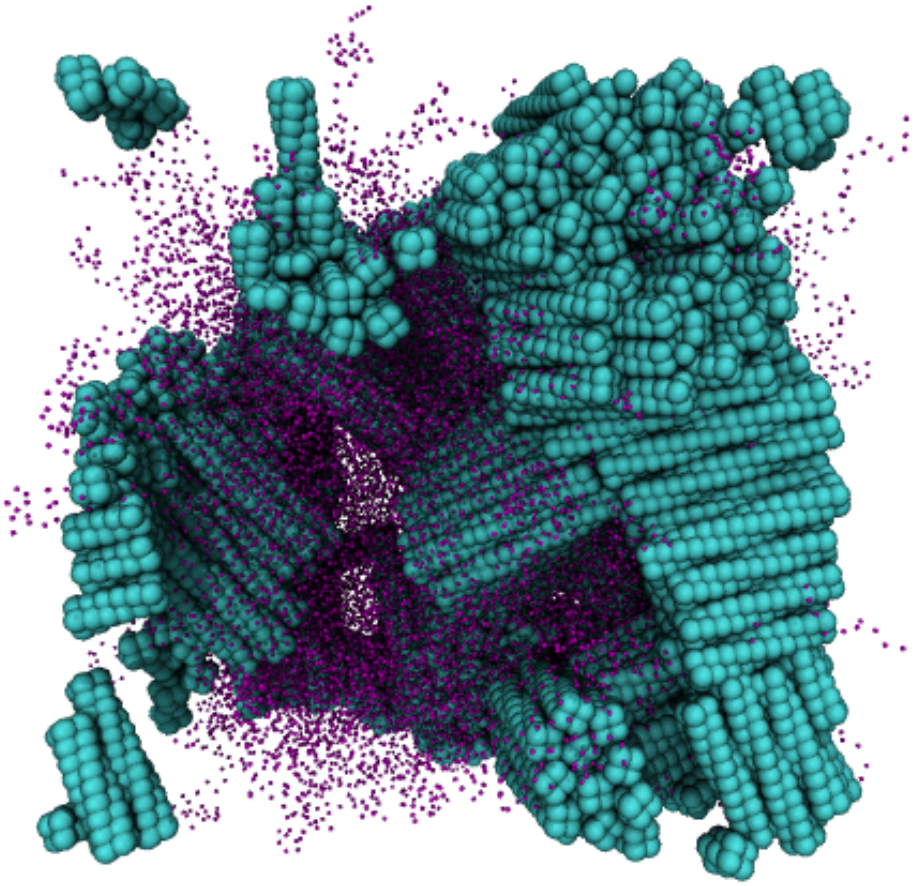

Figure 4.8: A system with repulsive interactions between all components is shown for $\phi_c = 0.5$. The polymers are shown as purple dots for illustration purposes. The rods are fully phase separated in the absence of the attractive forces but they are dispersed isotropically and show no orientational order in the system with attractive forces (see 4.4(d)).

a fully ordered state and 0.5 for an isotropic state. Figure 4.9 shows this value as a function of Δr for a range of concentrations. As can be seen, the neighbouring rods at short distances are very correlated and C_{rr} takes near one values. However, moving away from a reference rod, the orientational correlation between the rod and other rods fades away and C_{rr} decreases. Moreover, we can see a shift towards smaller C_{rr} values as the concentration of the system increases. This is on par with what we have already seen in figure 4.6: the order of the nanocomposite diminishes as the concentration of the rods increases.

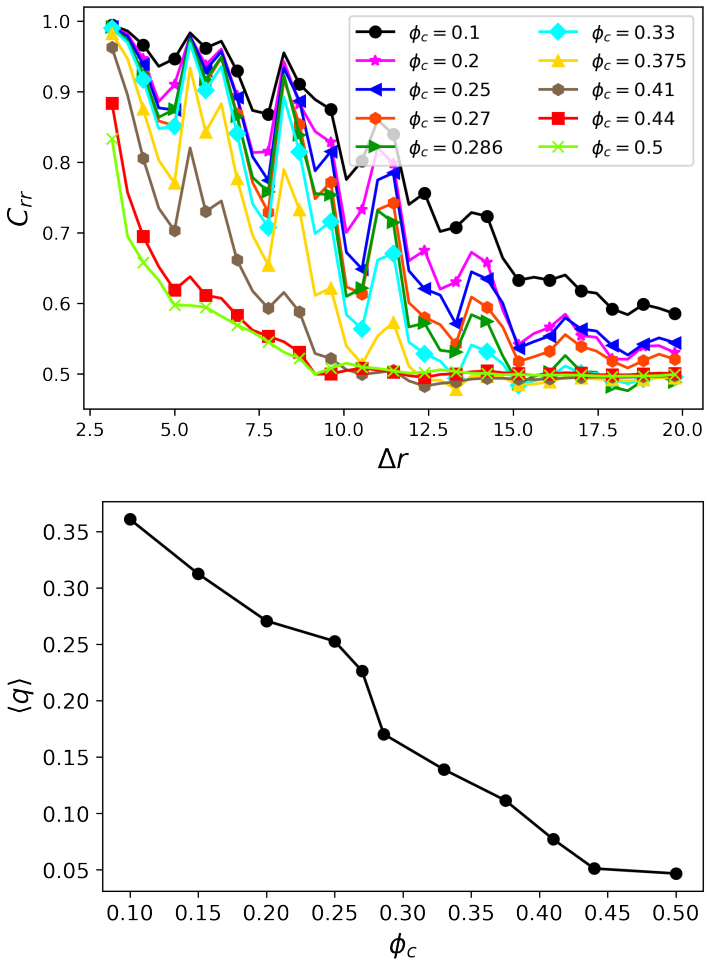

Figure 4.9: Orientational correlation between different rigid rod directors. The nearby rods align in the same direction which results in values close to 1 in low Δr and this value decreases as Δr increases. The nematic ordering of the rods weakens as the concentration of rods increases.

In addition to orientational correlation between the rods, we look at an order parameter q similar to the one in liquid crystals literature [27]. The q is defined as the largest eigenvalue of the traceless order parameter tensor

$$Q_{\alpha\beta} = \left\langle \hat{e}_\alpha \hat{e}_\beta - \frac{1}{3}\delta_{\alpha\beta} \right\rangle \tag{4.9}$$

where $\hat{e}$ is the unit vector (along the length) of a rod, $\alpha, \beta = x, y, z$, and the angle brackets denote the expectation value over all rods. The average of this value over 10 different realization is plotted as a function of concentration in figure 4.9(b). One more time, we see that the overall order of the nanocomposite decreases as a function of concentration. However, the slight bump between $\phi_c = 0.2$ and $\phi_c = 0.3$ suggests competition between the two present effects. At concentrations below $\phi_c = 0.2$, the enthaplic effects are weak and clusters form. Since rods prefer to align with their neighbours due to excluded volume effects [121] the clusters that form are highly ordered. Initially, packing more rods into the melt results in larger nematic droplets of rods. However, beyond $\phi_c = 0.3$, the enthalpic effects are strong enough to prevent phase separation. Besides, the entropic cost of extending and aligning polymer chains with ordered clusters is more than the entropic gain of the cluster formation. Therefore, we see a decrease in the size of the ordered clusters as well as the order parameter $\langle q \rangle$.

4.0.3.2 Interfacial polymers

The phase separation of rods, and nematic ordering within the aggregates, has important ramifications for the nanocomposite's mechanical properties. However, another factor that plays a determining role in understanding the mechanics of fracture of polymer-nanorod composites is the behaviour of polymer chains at the polymer-nanorod interface. Unlike nanorod dispersion patterns, the interfacial behaviour has not been studied significantly in the literature which is the motivation for the work in this section.

In their recent article, Lu et al. found that the polymer chains near nanorod surfaces take on more extended conformations while the chains far away behave like chains in a pure melt [95]. Our simulations tell a similar story. We measure the radius of gyration of the polymer chains within (near) and beyond (far) a distance of 5σ from surface of rods. The probability density of radius of gyration for far away chains is shown for all concentrations in figure 4.10(a). As can be seen, the graph is roughly normally distributed about peak of about $R_G = R_0$ which implies that bulk chains (non-interfacial) typically have a pure melt conformation. To see the difference between interfacial and bulk chains, we also plot the difference between the probability densities for polymers near and far from rods in figure 4.10(b). For concentrations up to $\phi_c \approx 0.3$, we consistently observe a dip for values below R_0 and a peak for values above R_0. The peak also moves to the right and expands to higher R_G's as the concentration increases. This is due to increase in the number of rods and in turn, more rods for the polymers to align with. For higher concentrations ($\phi_c > 0.3$), due to the abundance of rod surfaces, we see elongation in the bulk chains as well which results in a smaller difference between the far-away and near behaviour.

The presence of the rods in the melt results in stretching of polymer chains but we have not yet addressed the direction in which the polymers stretch. The chains can extend along the length of the rods or perpendicular to the direction of clusters. Therefore it is interesting to see if there is also some kind of orientational correlation between the rods and polymers. To measure this, we defined a rod-polymer correlation parameter such that

$$C_{rp}\left(|\Delta \boldsymbol{r}|\right) = \left\langle |\hat{\boldsymbol{e}}_i^r(\boldsymbol{r}) \cdot \hat{\boldsymbol{e}}_j^p(\boldsymbol{r} + \Delta \boldsymbol{r})| \right\rangle \tag{4.10}$$

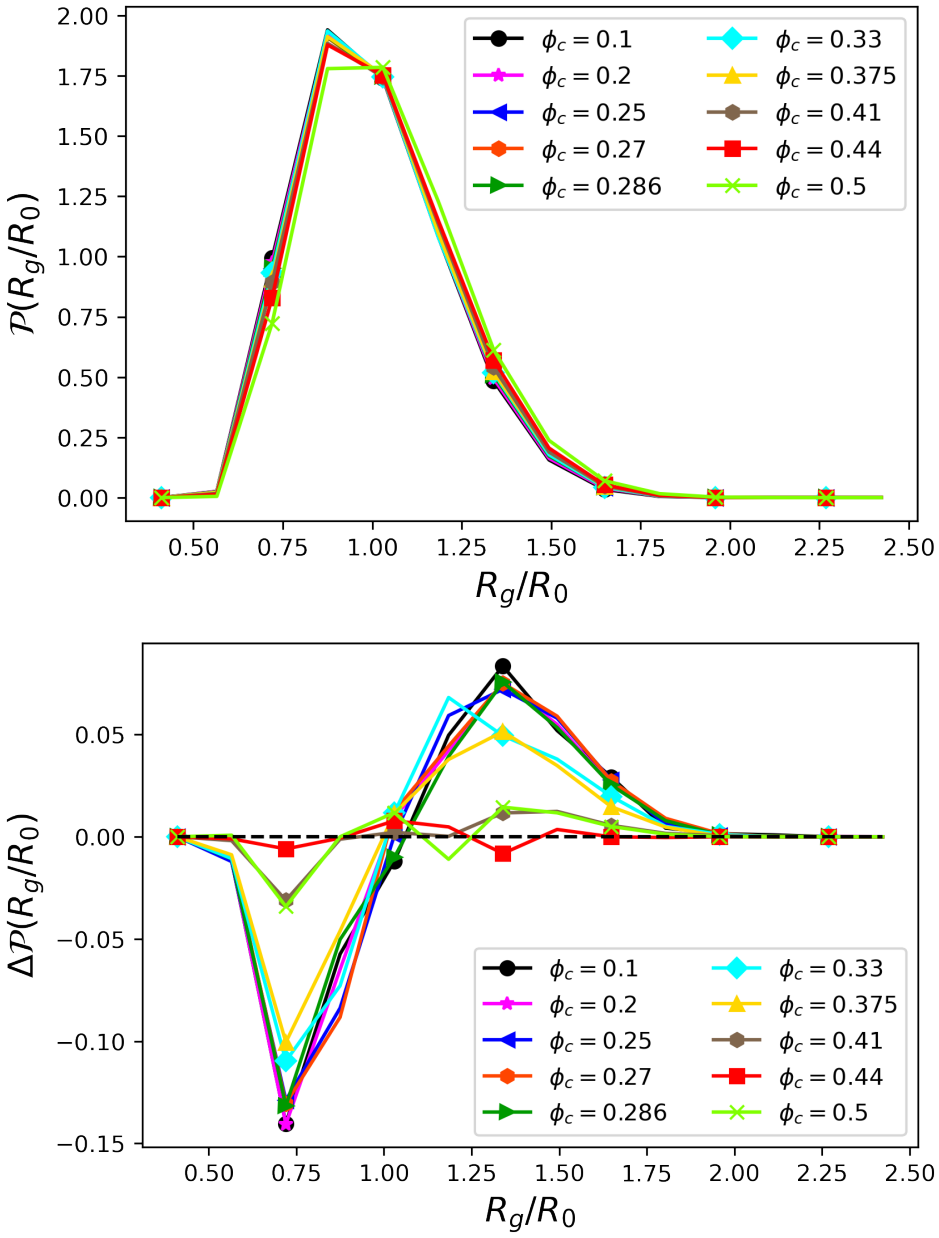

Figure 4.10: (a) depicts probability density of the normalized radius of gyration of polymer chains for selected concentrations while (b) shows the difference between the probability density of the near and far chains.

where $\hat{\boldsymbol{e}}_i^r$ and $\hat{\boldsymbol{e}}_j^p$ are the director of the ith rod and the end-to-end vector of jth polymer and $\Delta r = |\Delta \boldsymbol{r}|$ is the distance between the centre of mass of the rod and polymer. Figure 4.11 shows the values of this correlation parameter for selected concentrations. As can be seen, for all concentrations, polymers near rods are most elongated along the rod and the correlation decays as the distance increases. An interesting feature of this plot is the behaviour of C_{rp} as a function of concentration. The overall correlation goes up as the concentration increases up to $\phi_c \approx 0.3$ and then declines. By fitting an exponential, we have defined a length scale ℓ_{rp} which is plotted in figure 4.11(b) as a function of concentration. The ℓ_{rp} inclines at the beginning which corresponds to growth of cluster size and reaches a peak around $\phi_c = 0.3$. This agrees with what we have already seen in the previous sections. The initial rise in the number of rods results in larger ordered clusters where polymers sneak in between the rods and stretch along the director of the cluster. However, further increase in the number of rods leads to a less ordered system, particularly in the rod orientations, with an abundance of rod surfaces for the polymers to interact with. Therefore, the polymer chains do not show any preference to align with any specific rod.

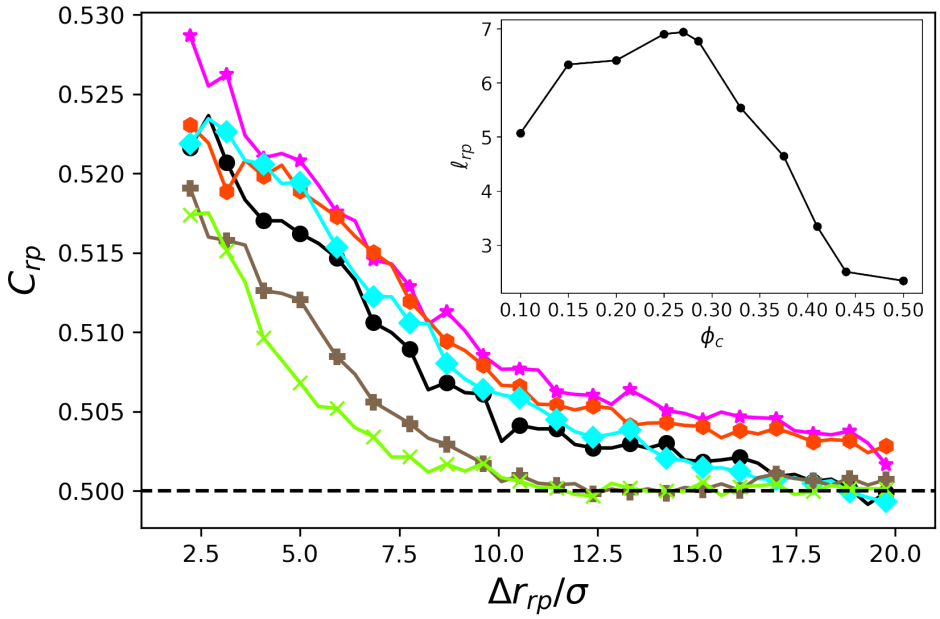

Figure 4.11: Orientational correlation C_{rp} between director of rods and polymers' end-to-end vector. The inset shows the length scale ℓ_{rp} as a function of concentration.

Lastly in this section, we look at the orientation of polymers with respect to each other by introducing a polymer-polymer correlation function like the ones defined for rod-rod and rod-polymer

$$C_{pp}\left(|\Delta \boldsymbol{r}|\right) = \left\langle |\hat{\boldsymbol{e}}_i^p(\boldsymbol{r}) \cdot \hat{\boldsymbol{e}}_j^p(\boldsymbol{r} + \Delta \boldsymbol{r})| \right\rangle \tag{4.11}$$

where e_i and e_j are the end-to-end vectors of the ith and jth polymer chains and $\Delta r = |\Delta \boldsymbol{r}|$ is the distance between the centre of mass of the polymers. In figure 4.12, the

relative orienational correlation, $\Delta C_{pp} = C_{pp} - C_{pp_{melt}}$, for selected concentrations is shown.

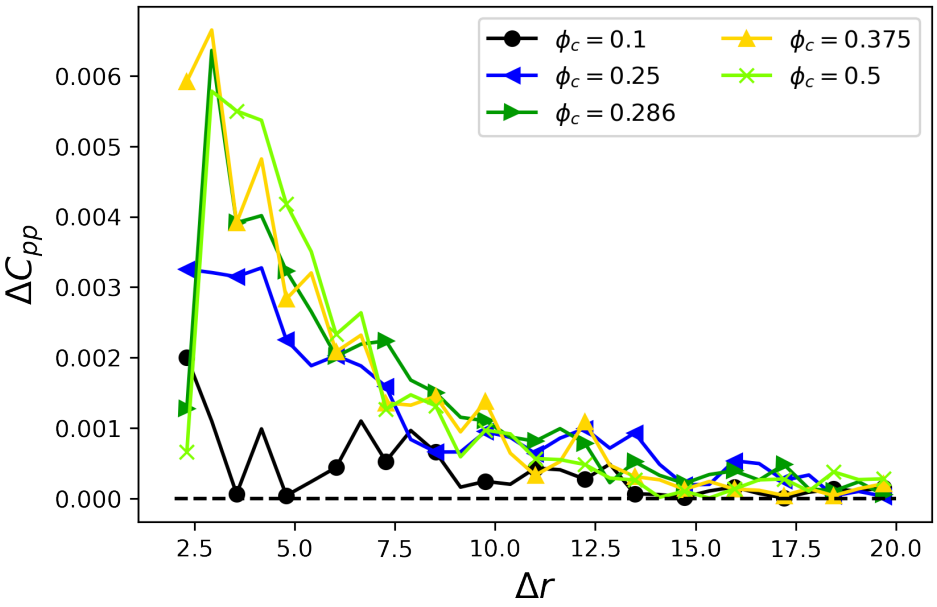

Figure 4.12: The relative Orientational correlation parameter $\Delta C_{pp} = C_{pp} - C_{pp_{melt}}$ as a function of pairwise distance

ΔC_{pp} takes higher values for lower distances at all concentrations as expected. The chains that align with a specific rod are as a result aligned with each other. With increase in the number of rods, more chains are exposed to rods and ΔC_{pp} increases. The long distance correlations become present as the size of the clusters grows. However, beyond the $\phi_c \approx 0.3$, the long range correlations become less significant again as the rod dispersion and orientation becomes more isotropic (see figure 4.8). Nevertheless, since the system is crowded with rods, the polymers stretch out in the space between them which is the reason for higher overall ΔC_{pp} at higher concentrations.

Chapter 5

Conclusions

Polymers and polymeric materials have proven to extremely useful in numerous industrial settings as well as in our day to day lives. Apart from being used extensively in industrial applications, the use of polymers in biomedical applications as well as in the development and design of smart materials has had a significant positive influence in our lives ([160]). Responsive and smart materials are actively being used to develop smart sensors and actuators due to their novel ability to quickly respond to external stimuli [26]. Due to their novel properties, smart polymeric materials have also sparked extensive experimental and computational research in this field ([52, 100, 112, 152, 205]).

Apart from the novel industrial applications, the biomedical applications and the importance of polymer based materials in the healthcare field cannot be overstated. Polymer based materials are being used in several crucial medical procedures such as heart implants and dental implants. Since polymeric materials tend to have fewer issues when incorporated in such medical procedures while also being cheap and easier to manufacture, their adoption in the healthcare industry has increased tremendously. As pointed out in the review works ([14, 93, 111]), the similarities between natural tissues, proteins and synthetic polymers due to their long chain architecture make polymeric materials suitable for use in procedures involving natural tissues. Due to similarities in structure and properties, a wide array of materials have been developed that are actively used in medical devices and procedures. Examples include acrylic cements for orthopedy, facial prostheses, joint surgeries, blood pushes, catheters, cardiac valves, pumps and so on. The biodegradable nature of certain polymeric materials have also proved important in the development of certain therapeutic devices such as temporary prostheses, bone implants, porous scaffolds for tissue regeneration as well as in nano sized drug transport vehicles ([40, 74, 92, 103, 129, 194]).

Polymers/proteins also play a crucial role in several biological and physiological processes. DNA which essentially is the blueprint of the human genome is the mostly commonly known biopolymer found in all living cells. Another protein that is commonly found in our circulatory system is the *von Willebrand factor* (vWF) and plays a crucial role in hemostasis. Our first research work is heavily influenced by vWF's novel margination tendency exhibited in high shear flows. In this work through extensive LBMD simulations, we have addressed the issue of polymer margination in Couette shear flows and have observed that monomer size plays a decisive role in the overall mi-

gration of the chains, either away or towards the channel walls. We have shown that the polymer chains comprised of larger radii monomers show a greater tendency to marginate in comparison to chains of same length however with smaller radii monomers. By measuring the probability distributions of the max extent of the chain into the channel bulk we were able to note that although the general trend of increase in probability over lower values of z_m with increasing shear rate was present in all cases, the difference in the distributions were more significant and more highly peaked for the larger monomer radii cases and the longer chains. We also looked studied the effect of scaling all the z_m residual distributions with their respective Weissenberg number but we did not see a good collapse of the resulting data. It seems likely that such a scaling may still be possible but would require defining the Weisenberg number with a relaxation time other than that of the equilibrium polymer in bulk. We mention again that the effects observed in this work appear to be a *chain effect* since in Couette flows due to the constant shear rate across the channel, individual monomers do not benefit from any cross-stream migration that would take them towards the walls.

By studying the chain's conformations through its radius of gyration in the x, y, z directions we also observed that in the vicinity of the surface, regardless the size of the monomer, every chain's lateral extent into the channel bulk was roughly the same however, the larger monomer sized chains showed higher probability to retain their elongated states along the shear direction compared to their smaller counterpart. Since larger sized monomers couple more with the shear flow as they experience a larger shear gradient across their entire surface, experience greater hydrodynamic stresses and also due to the anisotropic nature of the monomer's mobility near the surface, motion of the chains get significantly retarded near the surface causing it to relax more slowly. This in turn causes the chains to remain in their elongated conformations for longer causing more monomers to become adsorbed onto the surface. Our observed results can potentially be used to provide a functional reason for the exceptionally large size of vWF monomers (each monomer is typically made up of 2050 amino acids) and long length ($\sim 20,000$ kDa) of vWF multimers which play a crucial role in the initial stages of hemostasis [138].

Apart from the novel properties and dynamics exhibited by single chains in flows, polymeric solutions and melts exhibited far richer dynamics and properties under different situations. Polymer melts have a multitude of applications by themselves, but since the discovery of carbon nanotubes (CNTs) research interest in novel polymer nanocomposites (PNC) has grown tremendously. CNTs have displayed excellent mechanical strength, electrical conductivity and magnetic properties and their potential to be used in technological applications cannot be overstated. Due to such desirable traits, CNTs have been used quite extensively in the development of nanocomposites ([2, 10, 62, 94, 106, 107, 123, 139, 167, 205]). Apart from their intrinsic properties of the nanofillers/nanotubes used in the creation of the PNC, their distribution, orientation and dispersion throughout the melt has also shown to play a crucial role in the overall performance of the nanocomposite material ([3, 31, 80, 126]). Larger aspect ratio of the nanofillers/tubes are known to increase the efficiency of the polymer nanocomposite ([31, 126]) and previous computational works have studied the effect of nanorod length ([142,178]). In our second work we addressed the issue of nanorod diffusion throughout a melt of attractive polymer chains. We found that the dispersion and orientation patterns

of nanorods in polymer melts with rod-polymer attractive interactions can be explained by the competition between entropic and enthalpic effects. The entropic effects drive phase separation and are responsible for formation of nematic clusters of rods whereas the enthalpic effects bring the polymers and rods together and improve dispersion.

Since the strength of the enthalpic effects is proportional to the number of rods in the system, the dispersion patterns show direct correlation with the rod concentration. At lower concentrations, entropic processes are dominant and ordered clusters of nanorods are created. However, due to the presence of the attractive forces, the rods do not completely phase separate and polymers insert between the rods of a cluster. At higher concentrations, the energetic effects become significant and the dispersion of the rods improves. The structure and order of the system is also affected by the concentration. The system is more ordered at lower concentrations as a result of the formation of the ordered clusters, but as the concentration increases, the dispersion of the rods improves and excluded volume effects of the rods is screened. Therefore, the system becomes more isotropic.

5.1 Future Work

A simple next step to our work on polymer margination in uniform shear flows, further simulations of the same can be carried out in a Poiseuille flow to study the margination tendencies of chains further. Since its a pressure driven flow, the shear rate will be non-uniform throughout the channel and its effects on the chain's elongation, surface adsorption and margination as a function of the monomer size can be investigated further. Other interesting research questions could to use longer chains in much bigger channels to reduce finite size effects and also to consider a distribution of monomer sizes/types along a single chain. This would model some realistic differences between monomers within a single chain and the effect of the chain's margination can then be again studied. In our work, the surface was fully uniform and homogeneous. Although more computationally expensive, surfaces grafted with polymer brushes can also be considered in order model cell wall collagen linings and adsorption and margination of the chains under such conditions can be studied further.

With regards to the polymer melts, nanorods with polymer side brushes at different concentrations can be modelled and simulated. The dispersion of such rods can then be studied as a function of the polymer side brush concentrations. Nanorods of different lengths and sizes i.e. large aspect ratios can also be studied quite easily and their effects on the neighbouring chains can then be studied using similar approaches. Longer polymer chains can also be considered to better understand and differentiate between the entropic and enthalpic effects as observed in our current work. Moreover, also using coarse grained simulations, mechanical and elastic properties of the resulting PNC can be studied by suitably deforming the material and recording its stress strain curves. The mechanical strength and elastic results can then be correlated with the nanorod aspect ratio, dispersion and side brush grafting densities. All these ideas could be considered as viable next steps in order to better understand the properties of the systems studied in our work.

Bibliography

[1] R. Adhikari, M. E. Cates, K. Stratford, and A. J. Wagner, *Fluctuating lattice Boltzmann*, EPL (Europhysics Letters), 473 (2004), p. 7.

[2] P. M. Ajayan, O. Stephan, C. Colliex, and D. Trauth, *Aligned carbon nanotube arrays formed by cutting a polymer resin-nanotube composite*, Science, 265 (1994), pp. 1212–1214.

[3] M. H. Al-Saleh and U. Sundararaj, *Review of the mechanical properties of carbon nanofiber/polymer composites*, in Composites Part A: Applied Science and Manufacturing, vol. 42, Elsevier, Dec 2011, pp. 2126–2142.

[4] M. M. T. Alcanzare, V. Thakore, S. T. T. Ollila, M. Karttunen, and T. Ala-Nissila, *Controlled propulsion and separation of helical particles at the nanoscale*, Soft Matter, 13 (2017), pp. 2148–2154.

[5] a. Alexander-Katz and R. R. Netz, *Surface-enhanced unfolding of collapsed polymers in shear flow*, Europhysics Letters (EPL), 80 (2007), p. 18001.

[6] A. Alexander-Katz and R. R. Netz, *Dynamics and instabilities of collapsed polymers in shear flow*, Macromolecules, 41 (2008), pp. 3363–3374.

[7] A. Alexander-Katz, M. F. Schneider, S. W. Schneider, a. Wixforth, and R. R. Netz, *Shear-flow-induced unfolding of polymeric globules*, Physical Review Letters, 97 (2006), pp. 1–4.

[8] M. Al–Ghoul, J. P. Boon, P. V. Coveney, C. Denniston, D. Marenduzzo, E. Orlandini, and J. M. Yeomans, *Lattice boltzmann algorithm for three dimensional liquid crystal hydrodynamics*, Philosophical Transactions of the Royal Society of London. Series A: Mathematical, Physical and Engineering Sciences, 362 (2004), pp. 1745–1754.

[9] H. C. Andersen, *Molecular dynamics simulations at constant pressure and/or temperature*, The Journal of Chemical Physics, 72 (1980), pp. 2384–2393.

[10] B. Arash, Q. Wang, and V. K. Varadan, *Mechanical properties of carbon nanotube/polymer composites*, Scientific Reports, 4 (2014), p. 6479.

[11] G. B. Arfken and H. J. Weber, *Mathematical methods for physicists*, vol. 4th edition, Elsevier Academic Press, 30 Corporate Drive, Suite 400, Burlington, MA 01803, USA, 1995.

[12] S. Asakura and F. Oosawa, *On interaction between two bodies immersed in a solution of macromolecules*, The Journal of Chemical Physics, 22 (1954), pp. 1255–1256.

[13] D. Aztatzi-Pluma, E. O. Castrejón-González, A. Almendarez-Camarillo, J. F. Alvarado, and Y. Durán-Morales, *Study of the Molecular Interactions between Functionalized Carbon Nanotubes and Chitosan*, Journal of Physical Chemistry C, 120 (2016), pp. 2371–2378.

[14] P. Balakrishnan, V. Geethamma, M. S. Sreekala, and S. Thomas, *1 - polymeric biomaterials: State-of-the-art and new challenges*, in Fundamental Biomaterials: Polymers, S. Thomas, P. Balakrishnan, and M. Sreekala, eds., Woodhead Publishing Series in Biomaterials, Woodhead Publishing, 2018, pp. 1–20.

[15] G. K. Batchelor, *An Introduction to Fluid Dynamics*, Cambridge Mathematical Library, Cambridge University Press, 2000.

[16] R. Baughman, R. Chance, and M. J. Cohen, *A theoretical investigation of the solid-state synthesis of (sn)*, The Journal of Chemical Physics, 64 (1976), pp. 1869–1876.

[17] H. J. C. Berendsen, J. P. M. Postma, W. F. van Gunsteren, A. DiNola, and J. R. Haak, *Molecular dynamics with coupling to an external bath*, The Journal of Chemical Physics, 81 (1998), p. 3684.

[18] P. L. Bhatnagar, E. P. Gross, and M. Krook, *A model for collision processes in gases. i. small amplitude processes in charged and neutral one-component systems*, Phys. Rev., 94 (1954), pp. 511–525.

[19] C. Birdsall and A. Langdon, *Plasma Physics via Computer Simulation*, Series in Plasma Physics and Fluid Dynamics, Taylor & Francis, 2004.

[20] P. G. Bolhuis, A. Stroobants, D. Frenkel, and H. N. Lekkerkerker, *Numerical study of the phase behavior of rodlike colloids with attractive interactions*, Journal of Chemical Physics, 107 (1997), pp. 1551–1564.

[21] D. Braga and G. Horowitz, *High-performance organic field-effect transistors*, Advanced materials, 21 (2009), pp. 1473–1486.

[22] D. W. Brenner, *Tersoff-type potentials for carbon, hydrogen and oxygen*, MRS Proceedings, 141 (1988), p. 59.

[23] D. W. Brenner, *Empirical potential for hydrocarbons for use in simulating the chemical vapor deposition of diamond films*, Phys. Rev. B, 42 (1990), pp. 9458–9471.

[24] D. W. Brenner, O. A. Shenderova, J. A. Harrison, S. J. Stuart, B. Ni, and S. B. Sinnott, *A second-generation reactive empirical bond order (REBO) potential energy expression for hydrocarbons*, Journal of Physics: Condensed Matter, 14 (2002), pp. 783–802.

[25] T. Brettschneider, G. Volpe, L. Helden, J. Wehr, and C. Bechinger, *Force measurement in the presence of Brownian noise: Equilibrium- distribution method versus drift method*, Physical Review E - Statistical, Nonlinear, and Soft Matter Physics, 83 (2011), pp. 1–9.

[26] R. Brighenti, Y. Li, and F. J. Vernerey, *Smart polymers for advanced applications: A mechanical perspective review*, Frontiers in Materials, 7 (2020).

[27] S. Changizrezaei and C. Denniston, *Photonic band structure of diamond colloidal crystals in a cholesteric liquid crystal*, Physical Review E, 96 (2017), p. 32702.

[28] S. Chapman and T. G. Cowling, *The Mathematical Theory of Non-uniform Gases*.

[29] H. Chen, M. A. Fallah, V. Huck, J. I. Angerer, A. J. Reininger, S. W. Schneider, M. F. Schneider, and A. Alexander-Katz, *Blood-clotting-inspired reversible polymer-colloid composite assembly in flow.*, Nature Communications, 4 (2013), p. 1333.

[30] B. Chun and A. J. C. Ladd, *Interpolated boundary condition for Lattice-Boltzmann simulations of flows in narrow gaps*, Phys. Rev. E, 75 (2007), p. 066705.

[31] J. Coleman, U. Khan, and Y. Gun'ko, *Mechanical reinforcement of polymers using carbon nanotubes*, Advanced Materials, 18 (2006), pp. 689–706.

[32] J. N. Coleman, U. Khan, W. J. Blau, and Y. K. Gun'ko, *Small but strong: A review of the mechanical properties of carbon nanotube-polymer composites*, 2006.

[33] W. D. Cornell, P. Cieplak, C. I. Bayly, I. R. Gould, K. M. Merz, D. M. Ferguson, D. C. Spellmeyer, T. Fox, J. W. Caldwell, and P. A. Kollman, *A second generation force field for the simulation of proteins, nucleic acids, and organic molecules*, Journal of the American Chemical Society, 117 (1995), pp. 5179–5197.

[34] S. Danioko and M. Laradji, *Tumbling, stretching and cross-stream migration of polymers in rectilinear shear flow from dissipative particle dynamics simulations*, Physica A Statistical Mechanics and its Applications, 391 (2012), pp. 3379–3391.

[35] P. J. Dellar, *Bulk and shear viscosities in lattice-Boltzmann equations*, Phys. Rev. E, 64 (2001), p. 031203.

[36] F. Denorme, K. Vanhoorelbeke, and S. F. De Meyer, *von-Willebrand Factor and Platelet Glycoprotein Ib: A Thromboinflammatory Axis in Stroke*, Frontiers in Immunology, 10 (2019), p. 2884.

[37] F. Du, J. E. Fischer, and K. I. Winey, *Coagulation method for preparing single-walled carbon nanotube/poly(methyl methacrylate) composites and their modulus, electrical conductivity, and thermal stability*, Journal of Polymer Science, Part B: Polymer Physics, 41 (2003), pp. 3333–3338.

[38] A. Einstein et al., *On the motion of small particles suspended in liquids at rest required by the molecular-kinetic theory of heat*, Annalen der physik, 17 (1905), p. 208.

[39] Falck, E., Lahtinen, J. M., Vattulainen, I., and Ala-Nissila, T., *Influence of hydrodynamics on many-particle diffusion in 2d colloidal suspensions*, Eur. Phys. J. E, 13 (2004), pp. 267–275.

[40] E. Farng and O. Sherman, *Meniscal repair devices: a clinical and biomechanical literature review*, Arthroscopy: The Journal of Arthroscopic & Related Surgery, 20 (2004), pp. 273–286.

[41] N. A. Frej and D. C. Prieve, *Hindered Diffusion of a Single Sphere Very near a Wall in a Nonuniform Force-Field*, Journal of Chemical Physics, 98 (1993), pp. 7552–7564.

[42] U. Frisch, B. Hasslacher, and Y. Pomeau, *Lattice-Gas Automata for the Navier-Stokes Equation*, Phys. Rev. Lett., 56 (1986), pp. 1505–1508.

[43] M. Furlan, *Von Willebrand factor: Molecular size and functional activity*, Annals of Hematology, 72 (1996), pp. 341–348.

[44] Y. Gao, D. Cao, J. Liu, J. Shen, Y. Wu, and L. Zhang, *Molecular dynamics simulation of the conductivity mechanism of nanorod filled polymer nanocomposites*, Physical Chemistry Chemical Physics, 17 (2015), pp. 22959–22968.

[45] Y. Gao, J. Liu, J. Shen, L. Zhang, and D. Cao, *Molecular dynamics simulation of dispersion and aggregation kinetics of nanorods in polymer nanocomposites*, Polymer, 55 (2014), pp. 1273–1281.

[46] I. Ginzbourg and P. Adler, *Boundary condition analysis for the three dimensional lattice-Boltzmann model*, J. Phys. II France, 4 (1991), p. 191.

[47] I. Ginzburg, *Truncation Errors, Exact And Heuristic Stability Analysis Of Two-Relaxation-Times lattice-Boltzmann Schemes For Anisotropic Advection-Diffusion Equation*, Communications in Computational Physics, 11 (2012), p. 1439–1502.

[48] I. Ginzburg and D. d'Humières, *Multireflection boundary conditions for lattice Boltzmann models*, Phys. Rev. E, 68 (2003), p. 066614.

[49] A. Goldman, R. Cox, and H. Brenner, *Slow viscous motion of a sphere parallel to a plane wall—II Couette flow*, Chemical Engineering Science, 22 (1967), pp. 653–660.

[50] T. I. Gombosi, *Gaskinetic Theory*, Cambridge Atmospheric and Space Science Series, Cambridge University Press, 1994.

[51] N. Grossiord, J. Loos, O. Regev, and C. E. Koning, *Toolbox for dispersing carbon nanotubes into polymers to get conductive nanocomposites*, Chemistry of Materials, 18 (2006), pp. 1089–1099.

[52] T. Gruhn and H. Emmerich, *Simulation of stimuli-responsive polymer networks*, Chemosensors, 1 (2013), pp. 43–67.

[53] T. A. Halgren, *Merck molecular force field: Basis, form, scope, parameterization, and performance of MMFF94*, Journal of Computational Chemistry, 17 (1996), pp. 490–519.

[54] L. M. Hall and K. S. Schweizer, *Structure, scattering patterns and phase behavior of polymer nanocomposites with nonspherical fillers*, Soft Matter, 6 (2010), pp. 1015–1025.

[55] I. Halliday, L. A. Hammond, and C. M. Care, *Enhanced closure scheme for lattice-Boltzmann equation hydrodynamics*, Journal of Physics A: Mathematical and General, 35 (2002), pp. L157–L166.

[56] A. Hirsch, *Functionalization of single-walled carbon nanotubes*, Angewandte Chemie - International Edition, 41 (2002), pp. 1853–1859.

[57] M. Hoore, K. Rack, D. A. Fedosov, and G. Gompper, *Flow-induced adhesion of shear-activated polymers to a substrate*, Journal of Physics Condensed Matter, 30 (2018), p. 064001.

[58] W. G. Hoover, *Canonical dynamics: Equilibrium phase-space distributions*, Phys. Rev. A, 31 (1985), pp. 1695–1697.

[59] M. J. A. Hore and R. J. Composto, *Functional Polymer Nanocomposites Enhanced by Nanorods*, Macromolecules, 47 (2014), pp. 875–887.

[60] S. W. Hu, Y. J. Sheng, and H. K. Tsao, *Depletion-induced size fractionation of nanorod dispersions*, Soft Matter, 9 (2013), pp. 7261–7266.

[61] W. Humphrey, A. Dalke, and K. Schulten, *VMD: Visual molecular dynamics*, Journal of Molecular Graphics, 14 (1996), pp. 33–38.

[62] S. Iijima, *Helical microtubules of graphitic carbon*, Nature, 354 (1991), pp. 56–58.

[63] Y.-R. Jeng, P.-C. Tsai, and T.-H. Fang, *Molecular-dynamics studies of bending mechanical properties of empty and c60-filled carbon nanotubes under nanoindentation*, The Journal of Chemical Physics, 122 (2005), p. 224713.

[64] A. I. Jewett, D. Stelter, J. Lambert, S. M. Saladi, O. M. Roscioni, M. Ricci, L. Autin, M. Maritan, S. M. Bashusqeh, T. Keyes, R. T. Dame, J.-E. Shea, G. J. Jensen, and D. S. Goodsell, *Moltemplate: A Tool for Coarse-Grained Modeling of Complex Biological Matter and Soft Condensed Matter Physics*, Journal of Molecular Biology, 433 (2021), p. 166841. Computation Resources for Molecular Biology.

[65] W. L. Jorgensen, J. D. Madura, and C. J. Swenson, *Optimized intermolecular potential functions for liquid hydrocarbons*, Journal of the American Chemical Society, 106 (1984), pp. 6638–6646.

[66] W. L. Jorgensen, D. S. Maxwell, and J. Tirado-Rives, *Development and testing of the opls all-atom force field on conformational energetics and properties of organic liquids*, Journal of the American Chemical Society, 118 (1996), pp. 11225–11236.

[67] V. Kalra, F. Escobedo, and Y. L. Joo, *Effect of shear on nanoparticle dispersion in polymer melts: A coarse-grained molecular dynamics study*, Journal of Chemical Physics, 132 (2010).

[68] H. Kamberaj, *Faster protein folding using enhanced conformational sampling of molecular dynamics simulation*, Journal of Molecular Graphics and Modelling, 81 (2018), pp. 32–49.

[69] B. Kang, W. H. Lee, and K. Cho, *Recent advances in organic transistor printing processes*, ACS applied materials & interfaces, 5 (2013), pp. 2302–2315.

[70] I. Kang, H.-J. Yun, D. S. Chung, S.-K. Kwon, and Y.-H. Kim, *Record high hole mobility in polymer semiconductors via side-chain engineering*, Journal of the American Chemical Society, 135 (2013), pp. 14896–14899.

[71] A. Karatrantos, N. Clarke, and M. Kröger, *Modeling of polymer structure and conformations in polymer nanocomposites from atomistic to mesoscale: A review*, in Polymer Reviews, vol. 56, Taylor and Francis Inc., 2016, pp. 385–428.

[72] A. Karatrantos, R. J. Composto, K. I. Winey, and N. Clarke, *Structure and conformations of polymer/SWCNT nanocomposites*, Macromolecules, 44 (2011), pp. 9830–9838.

[73] J. Karger-Kocsis, H. Mahmood, and A. Pegoretti, *Recent advances in fiber/matrix interphase engineering for polymer composites*, in Progress in Materials Science, vol. 73, Elsevier Ltd, 2015, pp. 1–43.

[74] D. S. Katti, S. Lakshmi, R. Langer, and C. Laurencin, *Toxicity, biodegradation and elimination of polyanhydrides*, Advanced drug delivery reviews, 54 (2002), pp. 933–961.

[75] S. H. Khan, A. Prakash, P. Pandey, A. M. Lynn, A. Islam, M. I. Hassan, and F. Ahmad, *Protein folding: Molecular dynamics simulations and in vitro studies for probing mechanism of urea- and guanidinium chloride-induced unfolding of horse cytochrome-c*, International Journal of Biological Macromolecules, 122 (2019), pp. 695–704.

[76] S. H. Kim and H. Pitsch, *A generalized periodic boundary condition for lattice Boltzmann method simulation of a pressure driven flow in a periodic geometry*, Physics of Fluids, 19 (2007), p. 108101.

[77] H. Klauk, *Organic thin-film transistors*, Chemical Society Reviews, 39 (2010), pp. 2643–2666.

[78] K. Kremer and G. S. Grest, *Dynamics of entangled linear polymer melts: A molecular-dynamics simulation*, The Journal of Chemical Physics, 92 (1990), pp. 5057–5086.

[79] T. Krueger, H. Kusumaatmaja, A. Kuzmin, O. Shardt, G. Silva, and E. Viggen, *The Lattice Boltzmann Method: Principles and Practice*, Graduate Texts in Physics, Springer, 2016.

[80] S. Kumar, H. Doshi, M. Srinivasarao, J. O. Park, and D. A. Schiraldi, *Fibers from polypropylene/nano carbon fiber composites*, Polymer, 43 (2002), pp. 1701–1703.

[81] A. J. C. Ladd, *Numerical simulations of particulate suspensions via a discretized Boltzmann equation. Part 1. Theoretical foundation*, Journal of Fluid Mechanics, 271 (1994), p. 285–309.

[82] L. D. Landau and E. M. Lifshitz, *Fluid Mechanics, Second Edition: Volume 6 (Course of Theoretical Physics)*, Course of theoretical physics / by L. D. Landau and E. M. Lifshitz, Vol. 6, Butterworth-Heinemann, 2 ed., Jan. 1987.

[83] J. Latt, B. Chopard, O. Malaspinas, M. Deville, and A. Michler, *Straight velocity boundaries in the lattice Boltzmann method*, Phys. Rev. E, 77 (2008), p. 056703.

[84] L. G. Leal, *Inertial migration of rigid spheres in two-dimensional unidirectional flows*, 65 (1974).

[85] T. R. Lee, M. Choi, A. M. Kopacz, S. H. Yun, W. K. Liu, and P. Decuzzi, *On the near-wall accumulation of injectable particles in the microcirculation: Smaller is not better*, Scientific Reports, 3 (2013), pp. 1–8.

[86] W. H. Lee and Y. D. Park, *Organic semiconductor/insulator polymer blends for high-performance organic transistors*, Polymers, 6 (2014), pp. 1057–1073.

[87] H. N. Lekkerkerker and A. Stroobants, *Phase behaviour of rod-like colloid+flexible polymer mixtures*, Il Nuovo Cimento D, 16 (1994), pp. 949–962.

[88] J. Li, Y. Zhao, H. S. Tan, Y. Guo, C.-A. Di, G. Yu, Y. Liu, M. Lin, S. H. Lim, Y. Zhou, et al., *A stable solution-processed polymer semiconductor with record high-mobility for printed transistors*, Scientific Reports, 2 (2012), pp. 1–9.

[89] Y. Li, B. C. Abberton, M. Kröger, and W. K. Liu, *Challenges in multiscale modeling of polymer dynamics*, Polymers, 5 (2013), pp. 751–832.

[90] K. Liao and S. Li, *Interfacial characteristics of a carbon nanotube-polystyrene composite system*, Applied Physics Letters, 79 (2001), pp. 4225–4227.

[91] Q. Liu, L. Zhang, Y. Li, and B. Jiang, *Ring Polymer Molecular Dynamics in Gas–Surface Reactions: Inclusion of Quantum Effects Made Simple*, The Journal of Physical Chemistry Letters, 10 (2019), pp. 7475–7481.

[92] A. W. Lloyd, *Interfacial bioengineering to enhance surface biocompatibility.*, Medical Device Technology, 13 (2002), pp. 18–21.

[93] B. Love, *Chapter 9 - Polymeric Biomaterials*, in Biomaterials, B. Love, ed., Academic Press, 2017, pp. 205–238.

[94] K. Lozano and E. V. Barrera, *Nanofiber-reinforced thermoplastic composites. I. Thermoanalytical and mechanical analyses*, 79 (2001), pp. 125–133.

[95] S. Lu, Z. Wu, and A. Jayaraman, *Molecular Modeling and Simulation of Polymer Nanocomposites with Nanorod Fillers*, Journal of Physical Chemistry B, (2021).

[96] P. C. Ma, N. A. Siddiqui, G. Marom, and J. K. Kim, *Dispersion and functionalization of carbon nanotubes for polymer-based nanocomposites: A review*, Composites Part A: Applied Science and Manufacturing, 41 (2010), pp. 1345–1367.

[97] F. Mackay, S. Ollila, and C. Denniston, *Hydrodynamic forces implemented into LAMMPS through a lattice-Boltzmann fluid*, Computer Physics Communications, 184 (2013), pp. 2021–2031.

[98] F. E. Mackay, K. Pastor, M. Karttunen, and C. Denniston, *Modeling the behavior of confined colloidal particles under shear flow*, Soft Matter, 10 (2014), pp. 8724–8730.

[99] R. Mahnke, J. Kaupuzs, and I. Lubashevsky, *Physics of Stochastic Processes: How Randomness Acts in Time*, Physics textbook, Wiley, 2009.

[100] K. Matyjaszewski, *Atom transfer radical polymerization (atrp): Current status and future perspectives*, Macromolecules, 45 (2012), pp. 4015–4039.

[101] R. Mei, W. Shyy, D. Yu, and L.-S. Luo, *Lattice Boltzmann Method for 3-D Flows with Curved Boundary*, Journal of Computational Physics, 161 (2000), pp. 680–699.

[102] M. Menéndez, P. G. Jambrina, A. Zanchet, E. Verdasco, Y. V. Suleimanov, and F. J. Aoiz, *New stress test for ring polymer molecular dynamics: Rate coefficients of the o(3p) + hcl reaction and comparison with quantum mechanical and quasiclassical trajectory results*, The Journal of Physical Chemistry A, 123 (2019), pp. 7920–7931.

[103] J. C. Middleton and A. J. Tipton, *Synthetic biodegradable polymers as orthopedic devices*, Biomaterials, 21 (2000), pp. 2335–2346.

[104] A. Milchev, S. A. Egorov, J. Midya, K. Binder, and A. Nikoubashman, *Entropic Unmixing in Nematic Blends of Semiflexible Polymers*, ACS Macro Letters, 9 (2020), pp. 1779–1784.

[105] R. Mittal and G. Iaccarino, *Immersed Boundary Methods*, Annual Review of Fluid Mechanics, 37 (2005), pp. 239–261.

[106] M. Moniruzzaman and K. I. Winey, *Polymer nanocomposites containing carbon nanotubes*, Macromolecules, 39 (2006), pp. 5194–5205.

[107] V. Z. Mordkovich, *Carbon nanofibers: A new ultrahigh-strength material for chemical technology*, Theoretical Foundations of Chemical Engineering, 37 (2003), pp. 429–438.

[108] K. Müller, D. A. Fedosov, and G. Gompper, *Behaviour of the von Willebrand Factor in Blood Flow*, 4th Micro and Nano Flows Conference, (2014), pp. 7–10.

[109] K. Müller, D. A. Fedosov, and G. Gompper, *Margination of micro- and nano-particles in blood flow and its effect on drug delivery*, Scientific Reports, 4 (2014), pp. 1–8.

[110] M. Müser, G. Sutmann, and R. G. Winkler, eds., *Hybrid Particle-Continuum Methods in Computational Materials Physics*, vol. 46 of NIC Series, John von Neumann Institute for Computing (NIC), Jülich, Mar 2013.

[111] L. S. Nair and C. T. Laurencin, *Biodegradable polymers as biomaterials*, Progress in Polymer Science, 32 (2007), pp. 762–798.

[112] R. Nap, P. Gong, and I. Szleifer, *Weak polyelectrolytes tethered to surfaces: effect of geometry, acid–base equilibrium and electrical permittivity*, Journal of Polymer Science Part B: Polymer Physics, 44 (2006), pp. 2638–2662.

[113] R. W. Nash, H. B. Carver, M. O. Bernabeu, J. Hetherington, D. Groen, T. Krüger, and P. V. Coveney, *Choice of boundary condition for lattice-boltzmann simulation of moderate-reynolds-number flow in complex domains*, Phys. Rev. E, 89 (2014), p. 023303.

[114] S. K. Nath, F. A. Escobedo, and J. J. de Pablo, *On the simulation of vapor–liquid equilibria for alkanes*, The Journal of Chemical Physics, 108 (1998), pp. 9905–9911.

[115] S. T. T. Ollila, T. Ala-Nissila, and C. Denniston, *Hydrodynamic forces on steady and oscillating porous particles*, Journal of Fluid Mechanics, 709 (2012), p. 123–148.

[116] S. T. T. Ollila, C. Denniston, and T. Ala-Nissila, *One- and two-particle dynamics in microfluidic t-junctions*, Phys. Rev. E, 87 (2013), p. 050302.

[117] S. T. T. Ollila, C. Denniston, M. Karttunen, and T. Ala-Nissila, *Fluctuating lattice-Boltzmann model for complex fluids*, Journal of Chemical Physics, 134 (2011), p. 064902.

[118] S. T. T. Ollila, C. Denniston, M. Karttunen, and T. Ala-Nissila, *Hydrodynamic effects on confined polymers*, Soft Matter, 9 (2013), p. 3478.

[119] S. T. T. Ollila, C. Denniston, M. Karttunen, and T. Ala Nissila, *Biopolymer Filtration in Corrugated Nanochannels*, Phys. Rev. Lett., 112 (2014), p. 118301.

[120] S. T. T. Ollila, C. J. Smith, T. Ala-Nissila, and C. Denniston, *The Hydrodynamic Radius of Particles in the Hybrid Lattice Boltzmann Molecular Dynamics Method*, Multiscale Modeling & Simulation, 11 (2013), pp. 213–243.

[121] L. Onsager, *The Effects of Shape on the Interaction of Colloidal Particles*, Annals of the New York Academy of Sciences, 51 (1949), pp. 627–659.

[122] F. Paiva, A. Boromand, J. Maia, A. Secchi, V. Calado, and S. Khani, *Interfacial aggregation of Janus rods in binary polymer blends and their effect on phase separation*, Journal of Chemical Physics, 151 (2019), p. 114905.

[123] G. Pal and S. Kumar, *Modeling of carbon nanotubes and carbon nanotube-polymer composites*, Progress in Aerospace Sciences, 80 (2016), pp. 33–58.

[124] J. H. Park and Y. L. Joo, *Tailoring nanorod alignment in a polymer matrix by elongational flow under confinement: Simulation, experiments, and surface enhanced Raman scattering application*, Soft Matter, 10 (2014), pp. 3494–3505.

[125] J. H. Park, V. Kalra, and Y. L. Joo, *Controlling the dispersion and orientation of nanorods in polymer melt under shear: Coarse-grained molecular dynamics simulation study*, Journal of Chemical Physics, 140 (2014).

[126] R. Paul and L. Dai, *Interfacial aspects of carbon composites*, vol. 25, Taylor and Francis Ltd., jul 2018.

[127] C. S. Peskin, *Flow patterns around heart valves: A numerical method*, Journal of Computational Physics, 10 (1972), pp. 252–271.

[128] M. Phillips, *A force balance model for particle entrainment into a fluid stream*, Journal of Physics D: Applied Physics, 13 (1980), p. 221.

[129] E. Piskin, *Biodegradable polymers as biomaterials*, Journal of Biomaterials Science, Polymer Edition, 6 (1995), pp. 775–795.

[130] S. Plimpton, *Fast parallel algorithms for short-range molecular dynamics*, Journal of Computational Physics, 117 (1995), pp. 1 – 19.

[131] J. M. Polson and J. P. Gallant, *Equilibrium conformational dynamics of a polymer in a solvent*, Journal of Chemical Physics, 124 (2006).

[132] K. Rack, V. Huck, M. Hoore, D. A. Fedosov, S. W. Schneider, and G. Gompper, *Margination and stretching of von Willebrand factor in the blood stream enable adhesion*, Scientific Reports, 7 (2017), pp. 1–12.

[133] M. Radtke and R. R. Netz, *Shear-enhanced adsorption of a homopolymeric globule mediated by surface catch bonds*, The European Physical Journal E, 38 (2015), p. 69.

[134] M. Radtke, M. Radtke, and R. Netz, *Shear-induced dynamics of polymeric globules at adsorbing homogeneous and inhomogeneous surfaces*, European Physical Journal E, 37 (2014).

[135] R. Ramasubramaniam, J. Chen, and H. Liu, *Homogeneous carbon nanotube/polymer composites for electrical applications*, Applied Physics Letters, 83 (2003), pp. 2928–2930.

[136] M. Rubinstein and R. H. Colby., *Polymer physics*, Oxford University Press, Oxford ;, 2007.

[137] Z. M. Ruggeri, *von willebrand factor.*, The Journal of Clinical Investigation, 99 (1997), pp. 559–564.

[138] J. E. Sadler, *Biochemistry and genetics of von Willebrand factor*, Annual review of biochemistry, 67 (1998), pp. 395–424.

[139] N. G. Sahoo, S. Rana, J. W. Cho, L. Li, and S. H. Chan, *Polymer nanocomposites based on functionalized carbon nanotubes*, Progress in Polymer Science (Oxford), 35 (2010), pp. 837–867.

[140] U. K. Sankar and M. Tripathy, *Dispersion, depletion, and bridging of athermal and attractive nanorods in polymer melt*, Macromolecules, 48 (2015), pp. 432–442.

[141] G. Sansone, *Orthogonal Functions*, Dover Books on Mathematics, Dover, 1959.

[142] J. Sapkota, A. Gooneie, A. Shirole, and J. C. Martinez Garcia, *A refined model for the mechanical properties of polymer composites with nanorods having different length distributions*, Journal of Applied Polymer Science, 134 (2017), p. 45279.

[143] S. V. Savenko and M. Dijkstra, *Phase behavior of a suspension of colloidal hard rods and nonadsorbing polymer*, Journal of Chemical Physics, 124 (2006), p. 244909.

[144] H. A. Scheraga, M. Khalili, and A. Liwo, *Protein-Folding Dynamics: Overview of Molecular Simulation Techniques*, Annual Review of Physical Chemistry, 58 (2007), pp. 57–83.

[145] R. Schneider, A. R. Sharma, and A. Rai, *Introduction to Molecular Dynamics*, Springer Berlin Heidelberg, 2008, pp. 3–40.

[146] S. W. Schneider, S. Nuschele, A. Wixforth, C. Gorzelanny, A. Alexander-Katz, R. R. Netz, and M. F. Schneider, *Shear-induced unfolding triggers adhesion of von Willebrand factor fibers.*, Proceedings of the National Academy of Sciences of the United States of America, 104 (2007), pp. 7899–903.

[147] C. M. Schroeder, R. E. Teixeira, E. S. G. Shaqfeh, and S. Chu, *Characteristic periodic motion of polymers in shear flow*, Phys. Rev. Lett., 95 (2005), p. 18301.

[148] G. SEGRÉ and A. SILBERBERG, *Radial particle displacements in poiseuille flow of suspensions*, Nature, 189 (1961), pp. 209–210.

[149] F. Severini, L. Formaro, M. Pegoraro, and L. Posca, *Chemical modification of carbon fiber surfaces*, Carbon, 40 (2002), pp. 735–741.

[150] X. SHAN, X.-F. YUAN, and H. CHEN, *Kinetic theory representation of hydrodynamics: a way beyond the Navier–Stokes equation*, Journal of Fluid Mechanics, 550 (2006), p. 413–441.

[151] J. Shen, X. Li, L. Zhang, X. Lin, H. Li, X. Shen, V. Ganesan, and J. Liu, *Mechanical and Viscoelastic Properties of Polymer-Grafted Nanorod Composites from Molecular Dynamics Simulation*, Macromolecules, 51 (2018), pp. 2641–2652.

[152] T. Shimoboji, E. Larenas, T. Fowler, S. Kulkarni, A. S. Hoffman, and P. S. Stayton, *Photoresponsive polymer, enzyme switches*, Proceedings of the National Academy of Sciences, 99 (2002), pp. 16592–16596.

[153] D. S. Sholl, M. K. Fenwick, E. Atman, and D. C. Prieve, *Brownian dynamics simulation of the motion of a rigid sphere in a viscous fluid very near a wall*, Journal of Chemical Physics, 113 (2000), pp. 9268–9278.

[154] G. Silva and V. Semiao, *Truncation errors and the rotational invariance of three-dimensional lattice models in the lattice Boltzmann method*, Journal of Computational Physics, 269 (2014), pp. 259–279.

[155] C. E. Sing and A. Alexander-Katz, *Elongational flow induces the unfolding of von willebrand factor at physiological flow rates*, Biophysical Journal, 98 (2010), pp. L35–L37.

[156] C. E. Sing, J. G. Selvidge, and A. Alexander-Katz, *Von willlebrand adhesion to surfaces at high shear rates is controlled by long-lived bonds*, Biophysical Journal, 105 (2013), pp. 1475–1481.

[157] I. Singh, H. Shankaran, M. E. Beauharnois, Z. Xiao, P. Alexandridis, and S. Neelamegham, *Solution structure of human von willebrand factor studied using small angle neutron scattering*, Journal of Biological Chemistry, 281 (2006), pp. 38266–38275.

[158] D. E. Smith, H. P. Babcock, and S. Chu, *Single-Polymer Dynamics in Steady Shear Flow*, Science, 283 (1999), pp. 1724–1727.

[159] F. W. Starr, T. B. Schrøder, and S. C. Glotzer, *Molecular dynamics simulation of a polymer melt with a nanoscopic particle*, Macromolecules, 35 (2002), pp. 4481–4492.

[160] M. A. C. Stuart, W. T. Huck, J. Genzer, M. Müller, C. Ober, M. Stamm, G. B. Sukhorukov, I. Szleifer, V. V. Tsukruk, M. Urban, et al., *Emerging applications of stimuli-responsive polymer materials*, Nature Materials, 9 (2010), pp. 101–113.

[161] S. Succi, *The Lattice Boltzmann Equation for Fluid Dynamics and Beyond*, Clarendon Press, Oxford, 2001.

[162] K. Suga, Y. Kuwata, K. Takashima, and R. Chikasue, *A D3Q27 multiple-relaxation-time lattice Boltzmann method for turbulent flows*, Computers and Mathematics with Applications, 69 (2015), pp. 518–529.

[163] Y. V. Suleimanov, F. J. Aoiz, and H. Guo, *Chemical reaction rate coefficients from ring polymer molecular dynamics: Theory and practical applications*, The Journal of Physical Chemistry A, 120 (2016), pp. 8488–8502.

[164] H. Sun, *Compass: An ab initio force-field optimized for condensed-phase applicationsoverview with details on alkane and benzene compounds*, The Journal of Physical Chemistry B, 102 (1998), pp. 7338–7364.

[165] M. Surve, V. Pryamitsyn, and V. Ganesan, *Dispersion and percolation transitions of nanorods in polymer solutions*, Macromolecules, 40 (2007), pp. 344–354.

[166] W. C. Swope, H. C. Andersen, P. H. Berens, and K. R. Wilson, *A computer simulation method for the calculation of equilibrium constants for the formation of physical clusters of molecules: Application to small water clusters*, The Journal of Chemical Physics, 76 (1982), pp. 637–649.

[167] K. tak Lau, C. Gu, and D. Hui, *A critical review on nanotube and nanotube/nanoclay related polymer composite materials*, Composites Part B: Engineering, 37 (2006), pp. 425–436.

[168] T. T. Takaluoma, K. Laasonen, and R. S. Laitinen, *Molecular dynamics simulation of the solid-state topochemical polymerization of s2n2*, Inorganic Chemistry, 52 (2013), pp. 4648–4657.

[169] L. G. Tang and J. L. Karoos, *A review of methods for improving the interfacial adhesion between carbon fiber and polymer matrix*, Polymer Composites, 18 (1997), pp. 100–113.

[170] J. Tersoff, *New empirical model for the structural properties of silicon*, Phys. Rev. Lett., 56 (1986), pp. 632–635.

[171] J. Tersoff, *Empirical Interatomic Potential for Carbon, with Applications to Amorphous Carbon*, Phys. Rev. Lett., 61 (1988), pp. 2879–2882.

[172] J. Tersoff, *New empirical approach for the structure and energy of covalent systems*, Phys. Rev. B, 37 (1988), pp. 6991–7000.

[173] J. Tersoff, *Modeling solid-state chemistry: Interatomic potentials for multicomponent systems*, Phys. Rev. B, 39 (1989), pp. 5566–5568.

[174] W. Thomas, *Catch Bonds in Adhesion*, Annual Review of Biomedical Engineering, 10 (2008), pp. 39–57.

[175] W. E. Thomas, V. Vogel, and E. Sokurenko, *Biophysics of catch bonds*, Annu. Rev. Biophys., 37 (2008), pp. 399–416.

[176] A. P. Thompson, H. M. Aktulga, R. Berger, D. S. Bolintineanu, W. M. Brown, P. S. Crozier, P. J. in 't Veld, A. Kohlmeyer, S. G. Moore, T. D. Nguyen, R. Shan, M. J. Stevens, J. Tranchida, C. Trott, and S. J. Plimpton, *LAMMPS - a flexible simulation tool for particle-based materials modeling at the atomic, meso, and continuum scales*, Comp. Phys. Comm., 271 (2022), p. 108171.

[177] A. P. Thompson, H. M. Aktulga, R. Berger, D. S. Bolintineanu, W. M. Brown, P. S. Crozier, P. J. in 't Veld, A. Kohlmeyer, S. G. Moore, T. D. Nguyen, R. Shan, M. J. Stevens, J. Tranchida, C. Trott, and S. J. Plimpton, *LAMMPS - a flexible simulation tool for particle-based materials modeling at the atomic, meso, and continuum scales*, Computer Physics Communications, 271 (2022), p. 108171.

[178] G. N. Toepperwein, N. C. Karayiannis, R. A. Riggleman, M. Kröger, and J. J. De Pablo, *Influence of nanorod inclusions on structure and primitive path network of polymer nanocomposites at equilibrium and under deformation*, Macromolecules, 44 (2011), pp. 1034–1045.

[179] G. N. Toepperwein, R. A. Riggleman, and J. J. De Pablo, *Dynamics and deformation response of rod-containing nanocomposites*, Macromolecules, 45 (2012), pp. 543–554.

[180] R. Tuinier, T. Taniguchi, and H. H. Wensink, *Phase behavior of a suspension of hard spherocylinders plus ideal polymer chains*, European Physical Journal E, 23 (2007), pp. 355–365.

[181] D. Urbanik, S. Mani Dwivedi, and C. Denniston, *Simulations of microscopic propulsion of soft elastic bodies*, The European Physical Journal E, 41 (2018), p. 24.

[182] F. B. Usabiaga and R. Delgado-Buscalioni, *Characteristic times of polymer tumbling under shear flow*, Macromolecular Theory and Simulations, 20 (2011), pp. 466–471.

[183] L. Vaisman, H. D. Wagner, and G. Marom, *The role of surfactants in dispersion of carbon nanotubes*, 2006.

[184] L. Verlet, *Computer "Experiments" on Classical Fluids. I. Thermodynamical Properties of Lennard-Jones Molecules*, Phys. Rev., 159 (1967), pp. 98–103.

[185] J. C. Verschaeve and B. Müller, *A curved no-slip boundary condition for the lattice Boltzmann method*, Journal of Computational Physics, 229 (2010), pp. 6781–6803.

[186] J. C. G. Verschaeve, *Analysis of the lattice Boltzmann Bhatnagar-Gross-Krook no-slip boundary condition: Ways to improve accuracy and stability*, Phys. Rev. E, 80 (2009), p. 036703.

[187] G. Volpe, L. Helden, T. Brettschneider, J. Wehr, and C. Bechinger, *Influence of noise on force measurements*, Physical Review Letters, 104 (2010), pp. 1–4.

[188] G. J. Vroege and H. N. Lekkerkerker, *Phase transitions in lyotropic colloidal and polymer liquid crystals*, vol. 55, 1992.

[189] J. Wang, T. C. O'Connor, G. S. Grest, Y. Zheng, M. Rubinstein, and T. Ge, *Diffusion of Thin Nanorods in Polymer Melts*, Macromolecules, 54 (2021), pp. 7051–7059.

[190] M. Wang and Q. Kang, *Modeling electrokinetic flows in microchannels using coupled lattice Boltzmann methods*, Journal of Computational Physics, 229 (2010), pp. 728–744.

[191] Q. Wang, *Buckling of carbon nanotubes wrapped by polyethylene molecules*, Physics Letters A, 375 (2011), pp. 624 – 627.

[192] R. Werner, *Phy*, Rev, A, 58 (1998), p. 1827.

[193] A. T. White and C. K. Chong, *Rotational invariance in the three-dimensional lattice Boltzmann method is dependent on the choice of lattice*, J. Comput. Phys., 230 (2011), pp. 6367–6378.

[194] D. F. Williams and D. F. Williams, *The Williams dictionary of biomaterials*, Liverpool University Press, 1999.

[195] D. A. Wolf-Gladrow, *5. Lattice Boltzmann Models*, Springer Berlin Heidelberg, 2000, pp. 159–246.

[196] D. A. Wolf-Gladrow, *Lattice-gas cellular automata and lattice Boltzmann models: An introduction*, Springer, 2004.

[197] M. Wong, M. Paramsothy, X. J. Xu, Y. Ren, S. Li, and K. Liao, *Physical interactions at carbon nanotube-polymer interface*, Polymer, 44 (2003), pp. 7757–7764.

[198] X. L. Xie, Y. W. Mai, and X. P. Zhou, *Dispersion and alignment of carbon nanotubes in polymer matrix: A review*, 2005.

[199] X. Xu, M. M. Thwe, C. Shearwood, and K. Liao, *Mechanical properties and interfacial characteristics of carbon-nanotube-reinforced epoxy thin films*, Applied Physics Letters, 81 (2002), pp. 2833–2835.

[200] R. Young, D. Bloor, D. Batchelder, and C. Hubble, *Deformation mechanisms in polymer crystals*, Journal of Materials Science, 13 (1978), pp. 62–71.

[201] R. L. Zhang, Y. Liu, Y. D. Huang, and L. Liu, *Effect of particle size and distribution of the sizing agent on the carbon fibers surface and interfacial shear strength (IFSS) of its composites*, Applied Surface Science, 287 (2013), pp. 423–427.

[202] S. Zhang, W. B. Liu, L. F. Hao, W. C. Jiao, F. Yang, and R. G. Wang, *Preparation of carbon nanotube/carbon fiber hybrid fiber by combining electrophoretic deposition and sizing process for enhancing interfacial strength in carbon fiber composites*, Composites Science and Technology, 88 (2013), pp. 120–125.

[203] Y. Zhao, M. Byshkin, Y. Cong, T. Kawakatsu, L. Guadagno, A. De Nicola, N. Yu, G. Milano, and B. Dong, *Self-assembly of carbon nanotubes in polymer melts: Simulation of structural and electrical behaviour by hybrid particle-field molecular dynamics*, Nanoscale, 8 (2016), pp. 15538–15552.

[204] J. Zhu, J. D. Kim, H. Peng, J. L. Margrave, V. N. Khabashesku, and E. V. Barrera, *Improving the dispersion and integration of single-walled carbon nanotubes in epoxy composites through functionalization*, Nano Letters, 3 (2003), pp. 1107–1113.

[205] R. Zhu, E. Pan, and A. K. Roy, *Molecular dynamics study of the stress-strain behavior of carbon-nanotube reinforced Epon 862 composites*, Materials Science and Engineering A, 447 (2007), pp. 51–57.

[206] J. Zhuang, M. R. Gordon, J. Ventura, L. Li, and S. Thayumanavan, *Multi-stimuli responsive macromolecules and their assemblies*, Chemical Society Reviews, 42 (2013), pp. 7421–7435.

Appendix A

Moltemplate

Moltemplate [64] is a general cross platform text-based molecule builder tool for LAMMPS. It can be used to prepare custom coarse-grained molecular models as well as all-atom simulations as well. It supports the entire ATB molecular database along with a wide variety of existing force fields and models including OPLS, AMBER (GAFF, GAFF2), DREIDING, COMPASS, LOPLS, EFF, TraPPE, MOLC, mW, ELBA (water), oxDNA2. It is fully open source and can be used to build molecules using any of the force fields and atom styles in LAMMPS.

It is modular in structure, and the molecules built can be copied, combined and linked together as basic blocks to define new and complex molecules. Once the base molecules have been built, they and their subnits can be customized such as the atoms and subunits can be either moved, rotated or deleted. The tool is also iteroperable with other suite of scientific visualization software such as VMD, PACKMOL, OVITO, EMC and so on. For further details, visit Moltemplate. As an example we give a short moltemplate code snippet, obtained from the official moltemplate website for creating a simple water molecule

Figure A.1: Simple water molecule (white) Hydrogen atoms (red) oxygen

```
SPCE {
# AtomID MoleculeID AtomType charge    X       Y       Z
write("Data Atoms") {
$atom:o   $mol:w  @atom:O  -0.8476  0.0000000 0.00000 0.000000
$atom:h1  $mol:w  @atom:H   0.4238  0.8164904 0.00000  0.5773590
$atom:h2  $mol:w  @atom:H   0.4238  -0.8164904 0.00000 0.5773590
}
write_once("Data Masses") {
```

```
@atom:O 15.9994
@atom:H 1.008
}
write("Data Bonds") {
$bond:oh1 @bond:OH $atom:o $atom:h1
$bond:oh2 @bond:OH $atom:o $atom:h2
}


write("Data Angles") {
$angle:hoh @angle:HOH $atom:h1 $atom:o $atom:h2
}

write_once("In Settings") {
bond_coeff   @bond:OH         600.0   1.0
angle_coeff  @angle:HOH       75.0    109.47
pair_coeff   @atom:O @atom:O  0.1553  3.166
pair_coeff   @atom:H @atom:H  0.0     0.0
group spce type  @atom:O  @atom:H
fix fShakeSPCE spce shake 0.0001 10 100 b @bond:OH a @angle:HOH
# (Remember to "unfix" fShakeSPCE during minimization.)
# Note: Since we are using SHAKE constraints, the bond and angle strength
# parameters ("600.0", "75.0") do not matter. But the equilibrium bond
# length ("1.0") and equilibrium angle ("109.47") does matter. LAMMPS
# obtains these numbers from the bond_coeff and angle_coeff commands above.
}
write_once("In Init") {
# -- Default styles (for solo "SPCE" water) --
units        real
atom_style   full
pair_style   lj/charmm/coul/long 9.0 10.0
bond_style   harmonic
angle_style  harmonic
kspace_style pppm 0.0001
#pair_modify  mix arithmetic  # LEAVE THIS UNSPECIFIED!
}
} # end of definition of "SPCE" water molecule type
```

Appendix B

Hermite Polynomials

Hermite polynomials are a special set of orthogonal polynomials that naturally arise when solving for the simple quantum harmonic oscillator. They form a complete set of orthogonal polynomials and are especially useful in discretizing integrals over continuous domains. The *Hermite* polynomials, $H_n(x)$ may be defined by a *generating function* [11, 141]

$$\omega(x) = \frac{1}{\sqrt{2\pi}} \exp\left(-\frac{x^2}{2}\right) \tag{B.1}$$

They arise naturally as solutions to the *Hermite's* equation

$$\frac{d^2 f}{dx^2} - 2x\frac{df}{dx} + 2nf = 0 \tag{B.2}$$

and alternatively they can be generated recursively through *Rodrigues formula*

$$H_n(x) = (-1)^n \frac{1}{\omega(x)} \frac{d^n}{dx^n}\omega(x) \tag{B.3}$$

The first few Hermite polynomials are

$$\begin{aligned} H_0(x) &= 1 \\ H_1(x) &= x \\ H_2(x) &= x^2 - 1 \\ H_3(x) &= x^3 - 3x \\ H_4(x) &= x^4 - 6x^2 + 3 \\ H_5(x) &= x^5 - 10x^3 + 15x \end{aligned} \tag{B.4}$$

The Hermite polynomials also satisfy the following recurrence relation

$$H_{n+1}(x) = 2xH_n(x) - 2nH_{n-1}(x) \tag{B.5}$$

$$H_n^{'}(x) = 2nH_{n-1}(x) \tag{B.6}$$

One of the most useful features of these polynomials is the fact that they are orthogonal to each other with respect to the *weight function* $\omega(x)$ i.e

$$\int_{-\infty}^{\infty} \omega(x) H_n(x) H_m(x) dx = n!\delta_{nm} \tag{B.7}$$

Moreover, the 1-D Hermite polynomials also form a complete basis in $\mathbb{R}$, so in principle any well behaved function $f(x) \in \mathbb{R}$ can be represented as a series over Hermite polynomials

$$f(x) = \sum_{n=0}^{\infty} \frac{1}{n!} a_n H_n(x) \tag{B.8}$$

$$a_n = \int_{-\infty}^{\infty} f(x) H_n(x) \omega(x) dx \tag{B.9}$$

B.1 Gauss-Hermite Quadrature

On of the most important features of Hermite polynomials is its applications in numerical integration of functions. This is commonly referred to as *Gauss-Hermite* quadrature rules and simply states that the integral over $(-\infty, \infty)$ for any 1-D function $f(x)$ multiplied by the Hermite weight function, $\omega(x)$ can be approximated by a finite sum of the function values evaluated at certain points x_i called *abscissae*

$$\int_{-\infty}^{\infty} \omega(x) f(x) dx \approx \sum_{i=1}^{q} \omega_i f(x_i) \tag{B.10}$$

The accuracy of the approximation depends on the values and the number of *abscissae* points at which the function is evaluated at. Another important aspect of the relation B.10 is that if one chooses the *abscissae* as the n roots of the n^{th} order Hermite polynomial, then it is guaranteed that for any polynomial P of order $N = 2n - 1$ relation B.10 holds exactly i.e

$$\int_{-\infty}^{\infty} \omega(x) P^{(N)}(x) dx = \sum_{i=1}^{n} \omega_i P^{(N)}(x_i) \tag{B.11}$$

The weights, ω_i can then conveniently be obtained as

$$\omega_i = \frac{n!}{\left(n H^{(n-1)}(x_i)\right)^2} \tag{B.12}$$

B.2 Copyright Permissions

Molecular Modeling and Simulation of Polymer Nanocomposites with Nanorod Fillers

Author: Shizhao Lu, Zijie Wu, Arthi Jayaraman
Publication: The Journal of Physical Chemistry B
Publisher: American Chemical Society
Date: Mar 1, 2021

PERMISSION/LICENSE IS GRANTED FOR YOUR ORDER AT NO CHARGE

This type of permission/license, instead of the standard Terms and Conditions, is sent to you because no fee is being charged for your order. Please note the following:

- Permission is granted for your request in both print and electronic formats, and translations.
- If figures and/or tables were requested, they may be adapted or used in part.
- Please print this page for your records and send a copy of it to your publisher/graduate school.
- Appropriate credit for the requested material should be given as follows: "Reprinted (adapted) with permission from {COMPLETE REFERENCE CITATION}. Copyright {YEAR} American Chemical Society." Insert appropriate information in place of the capitalized words.
- One-time permission is granted only for the use specified in your RightsLink request. No additional uses are granted (such as derivative works or other editions). For any uses, please submit a new request.

If credit is given to another source for the material you requested from RightsLink, permission must be obtained from that source.

BACK CLOSE WINDOW

ELSEVIER LICENSE
TERMS AND CONDITIONS

Mar 09, 2022

This Agreement between University of Western Ontario -- Venkat Bala ("You") and Elsevier ("Elsevier") consists of your license details and the terms and conditions provided by Elsevier and Copyright Clearance Center.

License Number	5264870037512
License date	Mar 09, 2022
Licensed Content Publisher	Elsevier
Licensed Content Publication	Polymer
Licensed Content Title	Molecular dynamics simulation of dispersion and aggregation kinetics of nanorods in polymer nanocomposites
Licensed Content Author	Yangyang Gao,Jun Liu,Jianxiang Shen,Liqun Zhang,Dapeng Cao
Licensed Content Date	Mar 10, 2014
Licensed Content Volume	55
Licensed Content Issue	5
Licensed Content Pages	9
Start Page	1273
End Page	1281